Stanford University
Basin and Petroleum System Modeling
10th Annual Industrial Affiliates Meeting

November 13-15, 2017
Lompoc, California

Meeting Guide compiled by
Allegra Hosford Scheirer and Jane Moss

Field Trip Guide by
Allegra Hosford Scheirer & Les Magoon (Stanford University)
Professor Rick Behl (California State Univ. Long Beach)
http://bpsm.stanford.edu

2017 BPSM Industrial Affiliates

Aker BP (new for 2017)
Anadarko Petroleum Corporation (new for 2017)
Bureau of Energy Ocean Management (new for 2017)
ConocoPhillips
Hess
Saudi Aramco/Aramco Services Company
Southwestern Energy Company
Statoil (new for 2017)
Total Energy

With special thanks to
Biomarker Technologies, Inc.
Schlumberger
US DOE National Energy Technical Laboratory

Schedule of Events

Monday, 11/13/17, 5:30-7:30 p.m.	Icebreaker & Poster Session at Embassy Suites by Hilton, Lompoc
Tuesday, 11/14/17, 8:30 a.m.-5:00 p.m.	Oral Session at Embassy Suites by Hilton, Lompoc
Tuesday, 11/14/17, 6:00-9:00 p.m.	Group dinner, La Botte
Wednesday, 11/15/17, 8:00 a.m.-5:00 p.m.	Field trip to the Santa Maria Basin

November 14, 2017, Oral Session Agenda

Morning

9:00 a.m.	**Steve Graham or Allegra Hosford Scheirer**, Introduction
9:20 a.m.	**Will Thompson-Butler**, Improved understanding of petroleum charge and migration in the Middle Magdalena Valley, Colombia
9:45 a.m.	**Zack Burton**, Unraveling petroleum degradation, maturity, and mixing in the frontier Pegasus Basin, New Zealand
10:10-10:30 a.m.	**Coffee break**
10:30 a.m.	**Inessa Yurchenko**, Source rock heterogeneity and migrated hydrocarbons in the Triassic Shublik Formation and implications for unconventional resource evaluation in Arctic Alaska
11:05 a.m.	**Krongrath Suwannasri**, The effect of changes in permeability on pore pressure and petroleum migration predictions in BPSM
11:30 a.m.	**Tanvi Chheda,** Bayesian networks to quantify risk in basin and petroleum system modeling
11:55 a.m.	**Anatoly Aseev**, Introduction
12:05-1:15 p.m.	**Lunch**

Afternoon

1:15 p.m.	**Allegra Hosford Scheirer**, New initiatives in BPSM
1:30 p.m.	**Tapan Mukerji**, Basin modeling links to rock physics, seismic imaging and uncertainty quantification
1:45 p.m.	**Anshuman Pradhan**, Integrated constraints for basin modeling and seismic imaging: Application to the northern Gulf of Mexico
2:10 p.m.	**Wisam AlKawai**, Combining statistical rock physics and pressure and thermal history modeling to map reservoir lithofacies in the deepwater Gulf of Mexico
2:35 p.m.	**Laura Dafov**, Basin and petroleum system modeling of Terrebonne Basin gas hydrates, Northern Gulf of Mexico
3:00-3:20 p.m.	**Coffee break**
3:20 p.m.	**Wisam AlKawai**, Integrating structural restoration into basin and petroleum system modeling: A case study from the Mississippi Canyon area in the Gulf of Mexico
3:45 p.m.	**Laainam (Best) Chaipornkaew**, Incorporating the frictional stress limit into basin and petroleum system models improves stress and pore pressure predictions of critically-stressed sedimentary basins
4:10 p.m.	**Mustafa Al Ibrahim**, The effect of thermal maturity on the elastic properties of organic-rich mudrocks—A case study of the Shublik Formation, Alaska
4:35 p.m.	**Les Magoon & Ken Peters**, The Monterey(!) petroleum system of the onshore Santa Maria Basin

Evening

6:00-9:00 p.m.	Group Dinner at La Botte Restaurant, 812 N H St, Lompoc, CA

2017 Meeting Attendees

Attendee	Affiliate Organization
Mark Adamski	Statoil
Vladimir Blanco-Velandia	Ecopetrol
Kim Butler	Southwestern Energy
Stephen Anthony ("Stoney") Clark	Statoil
Tristan Cornu	Total
Giuseppe De Prisco	Statoil
Sergey Doronichev	Schlumberger
Gretchen Gillis	Aramco Services Company
John Guthrie	Hess
Mario Alberto Guzman-Vega	Ecopetrol
Ebbe Hartz	Aker BP
Xiaoli Liu	Anadarko Petroleum
Thomas Lorenson	USGS
Veit J. Matt	ConocoPhillips
Daniel Nientiedt	Statoil
Bryan Norman	Division of Oil, Gas, and Geothermal Resources
Tori Parisi	Anadarko Petroleum
Ken Peters	Schlumberger and Adjunct Professor, Stanford
Andres Reyes-Harker	Ecopetrol
Constantin Sandu	Aramco Services Company
Noelle Schoellkopf	Schlumberger and Adjunct Professor, Stanford
Vaughn Thompson	California Resources Corporation
Kevin Weberling	California Resources Corporation
Johannes Wendebourg	Total

Stanford Students	Stanford Scientists	Cal. State Univ. Long Beach
Wisam AlKawai	Nader Dutta	Prof. Richard Behl
Mustafa Al Ibrahim	Allegra Hosford Scheirer	Maia Davis
Anatoly Aseev	Les Magoon	Leo Giannetta
Zack Burton	Inessa Yurchenko	Vanya Keyes
Laainam Chaipornkaew		Megan Mortimer-Lamb
Tanvi Chheda		Ashley Newman
Laura Dafov		Jon Schwalbach
Stephen Dobbs		Ryan Weller
Anshuman Pradhan		
Krongrath Suwannasri		
Will Thompson-Butler		
Colin White		

2017 Meeting Abstracts Follow

IMPROVED UNDERSTANDING OF PETROLEUM CHARGE AND MIGRATION IN THE MIDDLE MAGDALENA VALLEY, COLOMBIA

William Thompson-Butler[1,*], Kenneth E. Peters[1,2], J. Michael Moldowan[3], Leslie B. Magoon[1], Allegra Hosford Scheirer[1], Vladimir Orlando Blanco[4], and Román Eugenio González[5]

[1]*Department of Geological Sciences, Stanford University, Stanford, CA*
[2]*Schlumberger, Mill Valley, CA*
[3]*Biomarker Technologies, Inc., Rohnert Park, CA*
[4]*Instituto Colombiano del Petróleo, Ecopetrol Bucaramanga, Colombia*
[5]*Exploration Onshore Division, Ecopetrol Bogotá, Colombia*
[*]rthomps@stanford.edu

Abstract

The Middle Magdalena Valley (MMV) is an intermontane basin and petroleum province in northwestern Colombia that, along with the Eastern Cordillera and Llanos, has acted as a regional sedimentary basin from the Triassic well into the Late Neogene (**Figure 1**). During the Cretaceous, restricted marine conditions within a broad foreland basin resulted mainly in the deposition of organic-rich carbonate and siliciclastic sediments in the area of the modern MMV (Cooper et al., 1995). While the Upper Cretaceous La Luna Formation is the primary regional source rock, the Cretaceous Tablazo and Umir Formations may also contribute (Zumberge, 1984; Ramon and Dzou, 1999). Despite over a century of petroleum exploration, the complex burial and variable exhumation history associated with the Andean orogeny add uncertainty to the evaluation of petroleum systems in the MMV by impacting the distribution, quality, and thermal maturity of the Cretaceous succession of organic-rich source rocks. This study utilizes the multivariate statistical analysis of source-related biomarker and isotopic ratios from oil samples to establish distinct oil 'tribes' and then infer the differences in source rock depositional environment, lithology, and thermal maturity between them.

Chemometric analysis of 73 oil samples, employing hierarchical cluster analysis (**Figure 2**) and principal component analysis, defines six geochemically distinct oil tribes that may originate from different source rocks or organofacies of the same source rock within the MMV (Peters et al., 2007). The tribes in this study show systematic distribution by both map location (**Figure 3**) and reservoir age. Tribes 1 through 4 are likely related to the primary regional source rock, the La Luna Formation. However, biomarker ratios (Peters et al., 2005) and alternating least squares analysis are used to observe regional differences in character and thermal maturity of the La Luna oil as well as mixing. The northernmost Tribe in the MMV, Tribe 5, likely originates from the middle Cretaceous Tablazo or Rosablanca Formations. Tribe 6, in the southern MMV, is the sole terrigenous oil identified in the study, suggesting a non-marine source in the western flank of the Eastern Cordillera or an extension of the Cretaceous Umir Formation. Finally, diamondoid analysis shows the presence of secondary cracking in the Tribe 6 oil, while also suggesting input from a deeply buried and cracked source in the central MMV that may be the middle Cretaceous Tablazo Formation (Dahl et al., 1999).

While 6 tribes have been identified, more than half of the oil recovered in the Middle Magdalena Valley has come from a series of Tribe 1 fields in the central portion of the study area. In the area of these fields the total vertical depth subsea to the top of the Cretaceous interval ranges dramatically from less than 2,500 feet to greater than 10,000 feet (**Figure 4**). This disparity illustrates the lateral heterogeneity in both exhumation and modern day source rock burial depth. 1-D modeling can effectively illustrate the differences in burial history laterally in the central MMV. However, to accurately characterize both charge timing and the presence of an early Cretaceous source suggested by diamondoid analysis, a full 2-D model and structural restoration will be utilized.

Figures

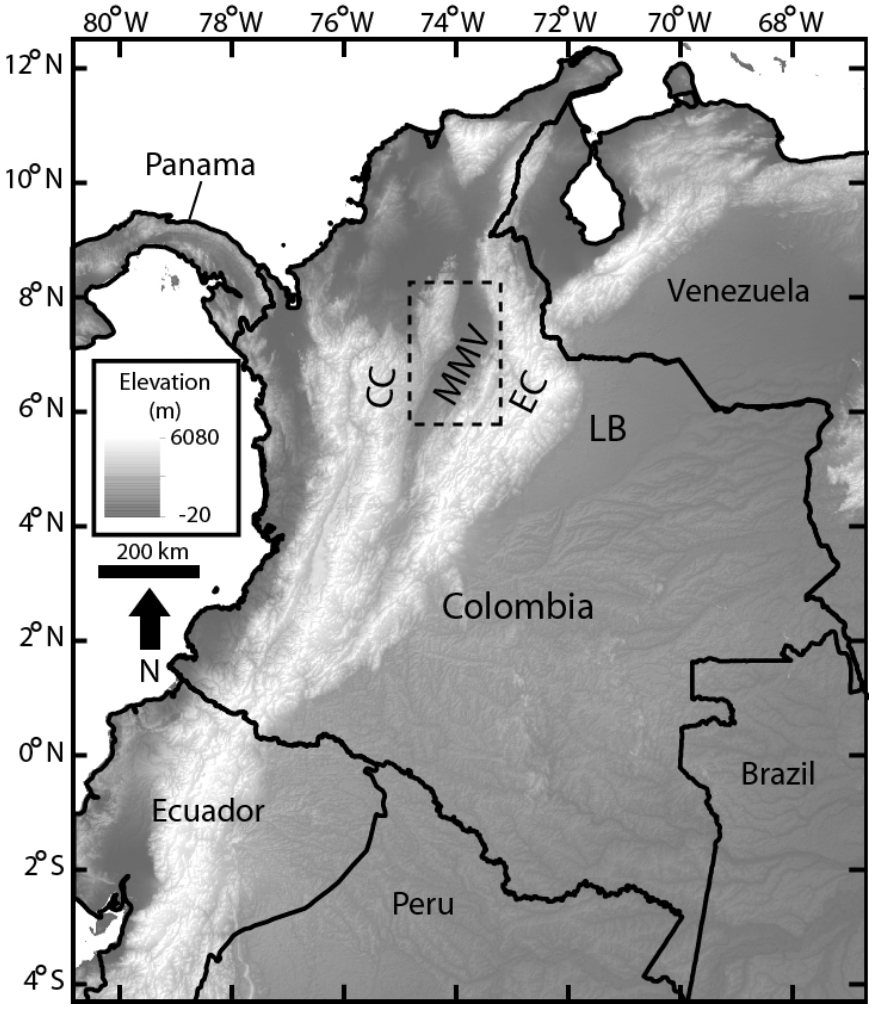

Figure 1. Map of Colombia showing elevation as well as the location of the Middle Magdalena Valley (MMV), Central Cordillera (CC), Eastern Cordillera (EC), and Llanos Basin (LB). Dashed box indicates location of Middle Magdalena Valley map used in Figures 3 and 4.

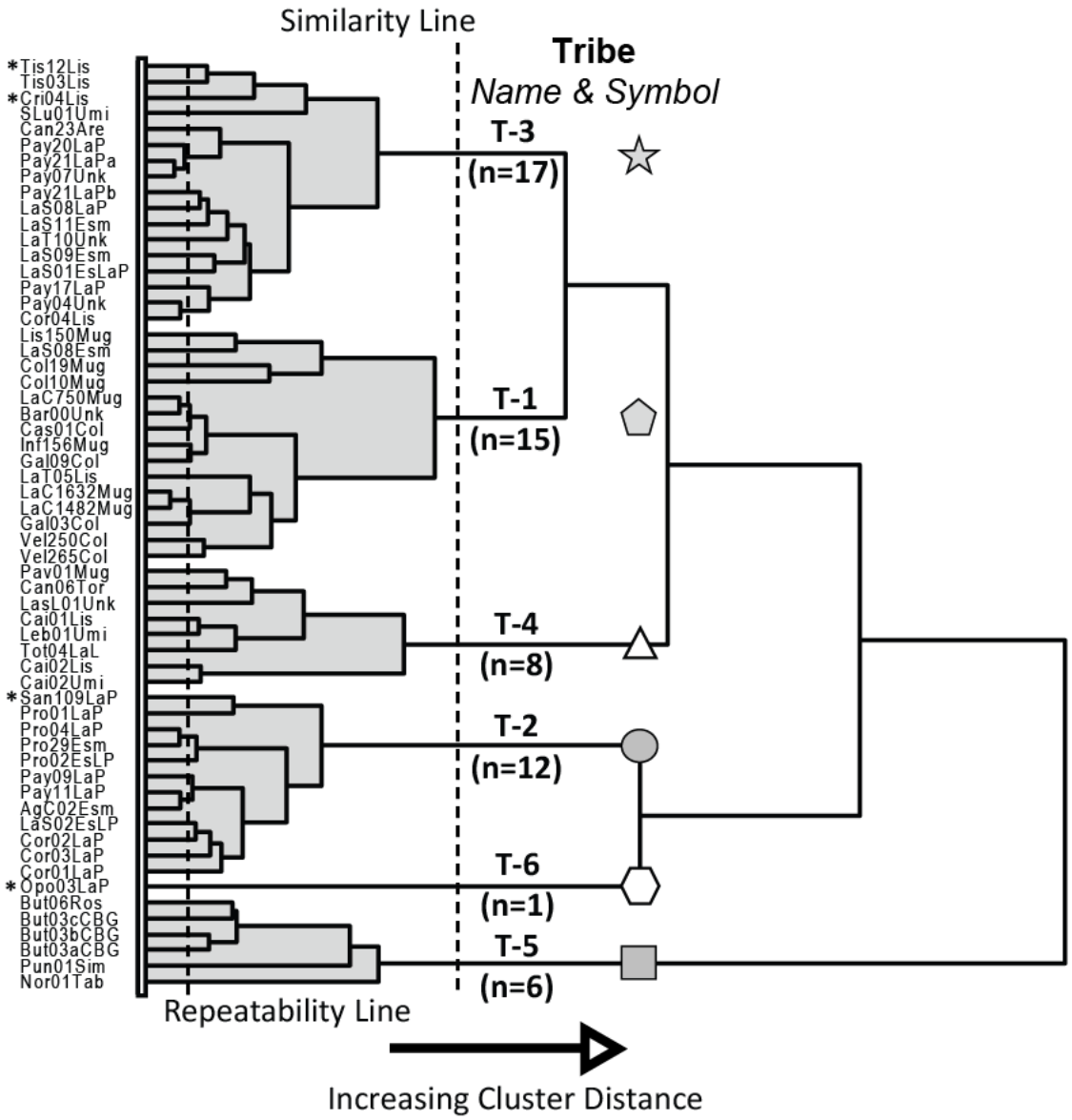

Figure 2. Hierarchical cluster analysis (HCA) dendrogram for the oil database provided by GeoMark Research. The HCA was built using 20 biomarker and isotopic ratios and identifies six total tribes in the Middle Magdalena Valley with the name, number of samples and map symbology for each tribe given. Samples marked by an asterisk were processed by both BTI and GeoMark Research. The Repeatability Line is based on the Pay20LaP and Pay21LaPa samples in Tribe 3 and the Pay09LaP and Pay11LaP samples in Tribe 2.

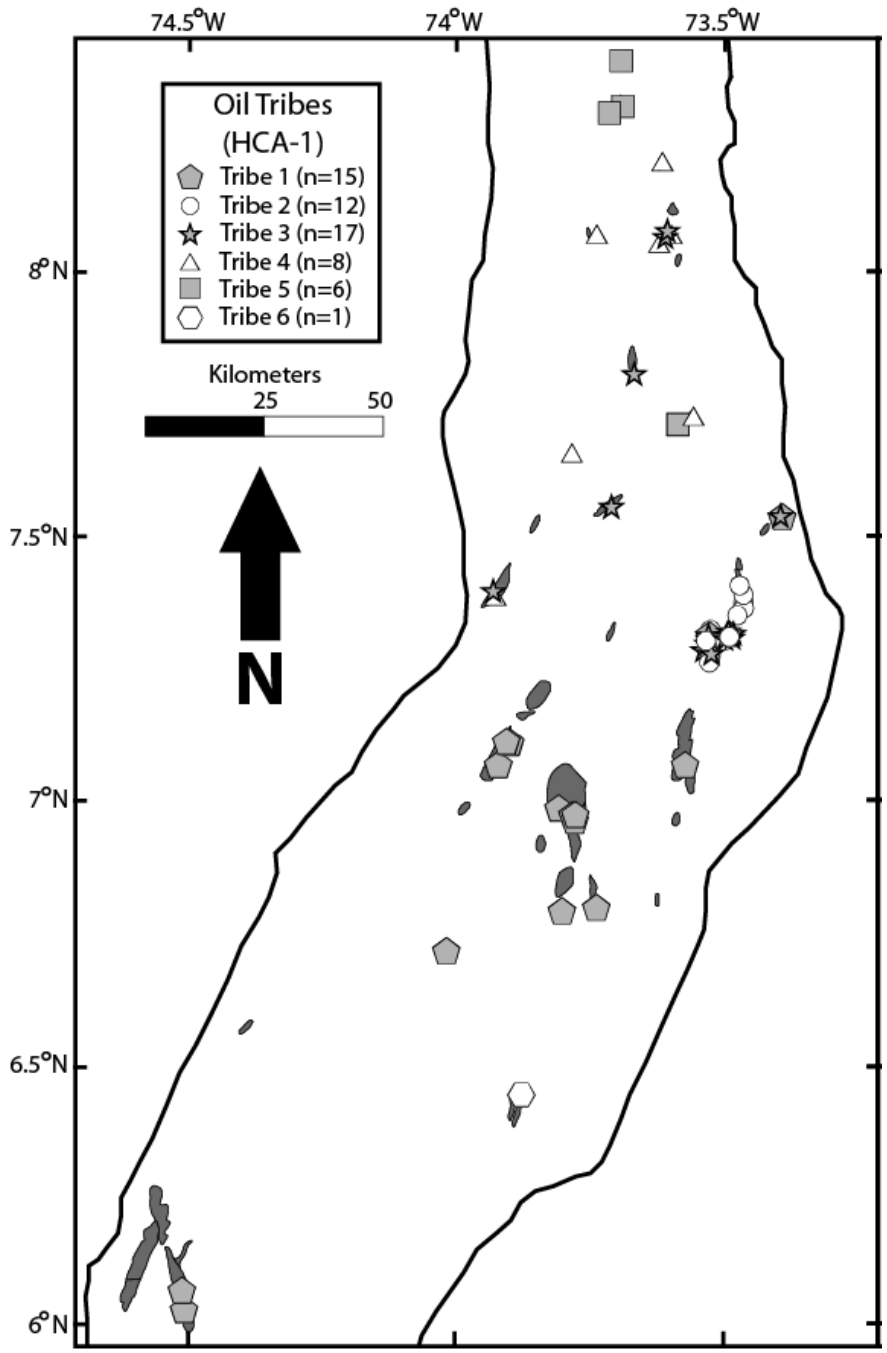

Figure 3. Map of the Middle Magdalena Valley showing the locations of oil samples used in HCA-1 with symbols indicating the petroleum tribe of each sample. Grey polygons are the locations of the primary oil fields in the MMV. Location of study area is indicated in Figure 1 by the dashed box.

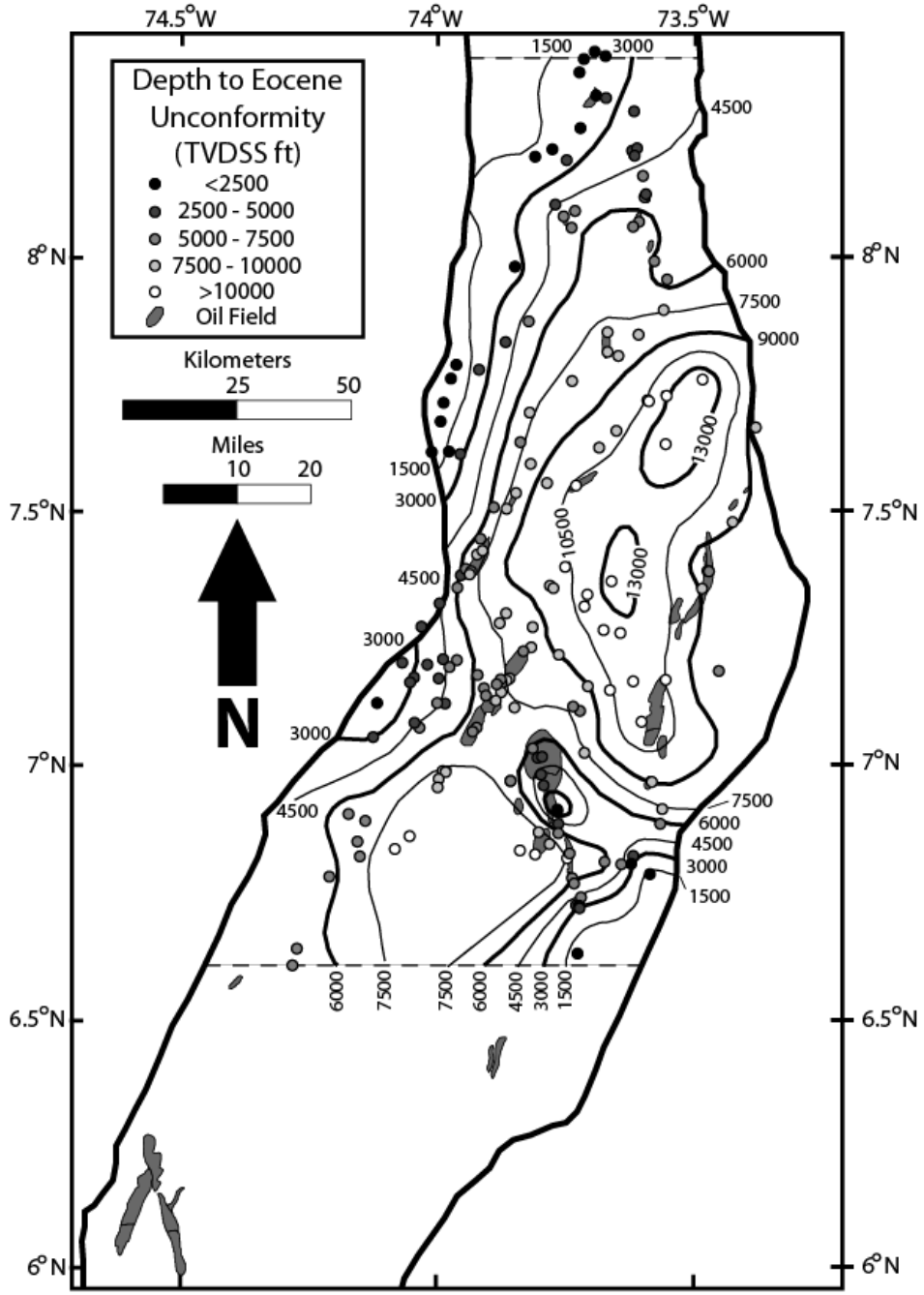

Figure 4. Map of the Middle Magdalena Valley contouring the depth to the top of the Cretaceous source rock package, marked by the Eocene unconformity, in total vertical depth subsea from 140+ wells. General deepening trends from both North to South and West to East exist in the MMV. Location of study area is indicated in Figure 1 by the dashed box.

Acknowledgments
The authors thank Ecopetrol, GeoMark Research, and Petroleum Systems International (PSI) for providing oil samples and analyses for this study and for permission to publish this work. Special thanks go out to Dave Wavrek, Biomarker Technologies, Inc., Infometrix, and the members of the Basin and Petroleum System Modeling Group at Stanford for many rounds of constructive review over the course of this project.

References
Cooper, M. A., F. T. Addison, R. Alvarez, M. Coral, R. H. Graham, A. B. Hayward, S. Howe, J. Martinez, J. Naar, R. Penas, A. J. Pulham, and A. Taborda, 1995, Basin development and tectonic history of the Llanos Basin, Eastern Cordillera and Middle Magdalena Valley, Colombia: AAPG Bulletin, v. 79, p. 1421-1443.

Dahl, J. E., J. M. Moldowan, K. E. Peters, G. E. Claypool, M. A. Rooney, G. E. Michael, M. R. Mello, and L. Kohnen, 1999, Diamondoid hydrocarbons as indicators of natural oil cracking: Nature, v. 399, p. 54-57.

Peters, K. E., L. S. Ramos, J. E. Zumberge, Z. C. Valin, C. R. Scotese, and D. L. Gautier, 2007, Circum-Arctic petroleum systems identified using decision-tree chemometrics: AAPG Bulletin, v. 91, no. 6, p. 877-913.

Peters, K. E., C. C. Walters, and J. M. Moldowan, 2005, The biomarker guide: Cambridge, UK, Cambridge University Press, 1155 p.

Ramon, J. C., and L. I. Dzou, 1999, Petroleum geochemistry of the Middle Magdalena Valley: Colombia: Organic Geochemistry, v. 30, p. 249-266.

Zumberge, J. E., 1984, Source rocks of the La Luna Formation (Upper Cretaceous) in the middle Magdalena Valley, Colombia: Petroleum Geochemistry and Source Rock Potential of Carbonate Rocks (Palacas J. C., ed.), AAPG Studies in Geology #18, p. 127-133.

UNRAVELING PETROLEUM DEGRADATION, MATURITY, AND MIXING IN THE FRONTIER PEGASUS BASIN, NEW ZEALAND

Zachary F. M. Burton[1,*], J. Michael Moldowan[1,2], Richard Sykes[3], Stephan A. Graham[1]
[1]Department of Geological Sciences, Stanford University, Stanford, CA
[2]Biomarker Technologies Incorporated, Rohnert Park, CA
[3]GNS Science, Institute for Geological and Nuclear Sciences, Lower Hutt 5040, New Zealand
*zburton@stanford.edu

Abstract
Determining hydrocarbon quality is essential to identifying valuable resource accumulations. However, in new areas of exploration, little information is available on the processes affecting resource quantity and quality. Geochemical analyses of oil seeps from frontier regions of New Zealand's east coast illustrate an application of underutilized resource quality assessment techniques. Distributions of n-alkanes and isoprenoids reveal biodegradation, and thus potentially lower oil quality in the southern versus the northern oil seeps. However, sterane and terpane compounds are unaltered, indicating overall biodegradation of these oils is low to moderate. Additionally, lack of 25-norhopane indicates degradation of southern oils may be solely aerobic. Therefore, any subsurface accumulations are potentially unaffected. Investigation of sterane and hopane isomerization ratios and additional sterane and terpane maturity parameters is paired with diamondoid analyses of oil-to-gas conversion and petroleum mixing. Three distinct hydrocarbon mixtures are identified among the sampled seeps: 1) a seep composed of an early/peak oil window component and an intensely cracked condensate/wet gas component, 2) seeps solely containing a peak/late oil window component, and 3) seeps composed of a peak/late oil window component and an intensely cracked condensate/wet gas component. Identified components indicate at least three distinct charges or stages of petroleum generation. Black oil components might indicate actively producing source rock in all regions represented by the seeps. Intensely cracked components indicate hydrocarbon mixing via thermogenic gas infiltration, and suggest an effect on oil quality. Important questions concerning migration pathways and timing, ties to New Zealand's offshore basins, and potential for reservoir entrapment of these hydrocarbon components

Background
The key goal of the oil and gas industry's upstream sector is to find and extract significant amounts of energy resources. Because there are high risks associated with this process, methods for identifying economically-attractive accumulations are critical. Geochemical analysis of oils is one technique available for assessing both the presence and producibility of petroleum accumulations (Hunt, 1979; Tissot and Welte, 1984).

Analytical geochemistry provides inexpensive methods to leverage the limited data available in frontier exploration areas. Geochemical technology can be successfully applied to determine impact of biodegradation on oil quality and to identify petroleum mixtures (Seifert & Moldowan, 1979; Connan, 1984; Volkman et al., 1984; Peters et al., 2005). It can be used to assess contribution of shallow versus deep sources and to fingerprint conversion of oil to gas (Jones and Drozd, 1983; Behar et al., 1992; Dahl et al., 1999).

Analysis of geochemical data in conjunction with geological and geophysical data is critical for success in frontier exploration and production (Demaison, 1984).

Oil seeps in areas of New Zealand's east coast are an ideal target for demonstrating the power and utility of advanced geochemical techniques. This region contains hundreds of seeps, shows, and other petroleum indicators, and has seen exploration interest for over a century (Uruski, 2010). Despite this, understanding of petroleum systems is limited, and significant accumulations of oil and gas remain undiscovered (Uruski, 2010).

We present results from our studies of onshore oil seep samples from New Zealand's North Island and South Island (Figure 1). We studied biomarker and diamondoid compounds to determine the degree of petroleum biodegradation (Figures 2-5), to assess thermal maturity (Figures 6-7), and to calculate the extent of cracking of these oils (Figure 7). We bring the results of these studies together to characterize source mixing and to identify different charges revealed by these oils.

Figures

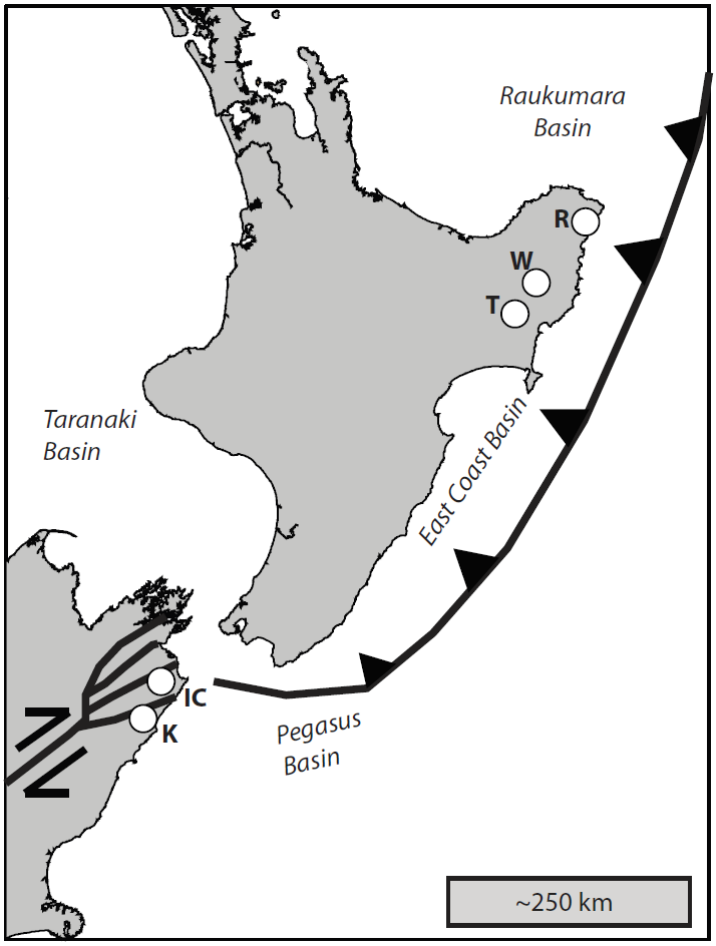

Figure 1. Area of interest and general setting; white circles indicate oil seep locations labeled as follows: R for Rotokautuku, W for Waitangi, T for Totangi, IC for Isolation Creek, and K for Kaikoura; black lines indicate active plate boundary; frontier basins most relevant to this study, as well as the established Taranaki Basin, are labeled.

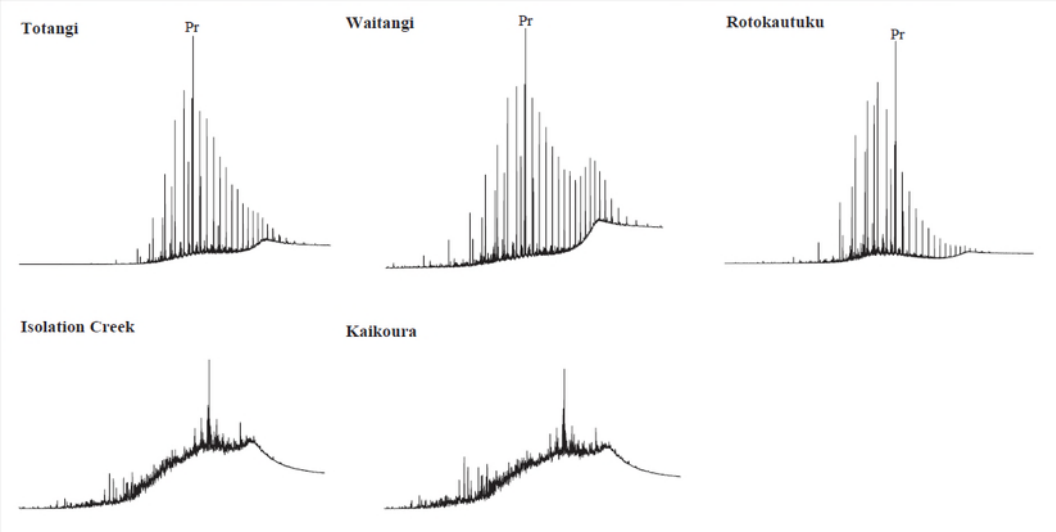

Figure 2. Whole-oil gas chromatograms show n-alkane and isoprenoid distributions and illustrate the contrast between 1) the very high preservation of n-alkane and isoprenoid compounds in the Totangi, Waitangi, and Rotokautuku oil seep samples and 2) the poor preservation, i.e., nearly complete destruction of n-alkanes and isoprenoids in the Isolation Creek and Kaikoura oil samples; GC-FID chromatograms from GNS Science public report (Sykes et al., 2012).

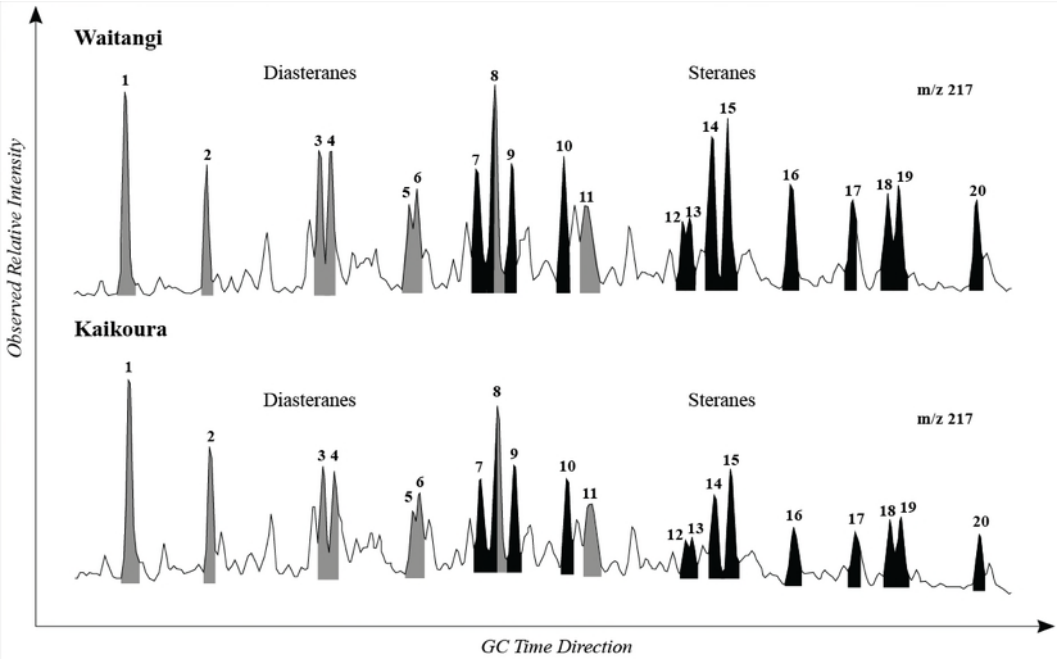

Figure 3. Representative m/z 217 fragmentograms of selected sterane distributions for the Waitangi and Kaikoura samples illustrate the preservation of sterane biomarkers and the similarity of sterane:diasterane ratios for all samples; Obtained via GC-MS of saturate hydrocarbon fractions.

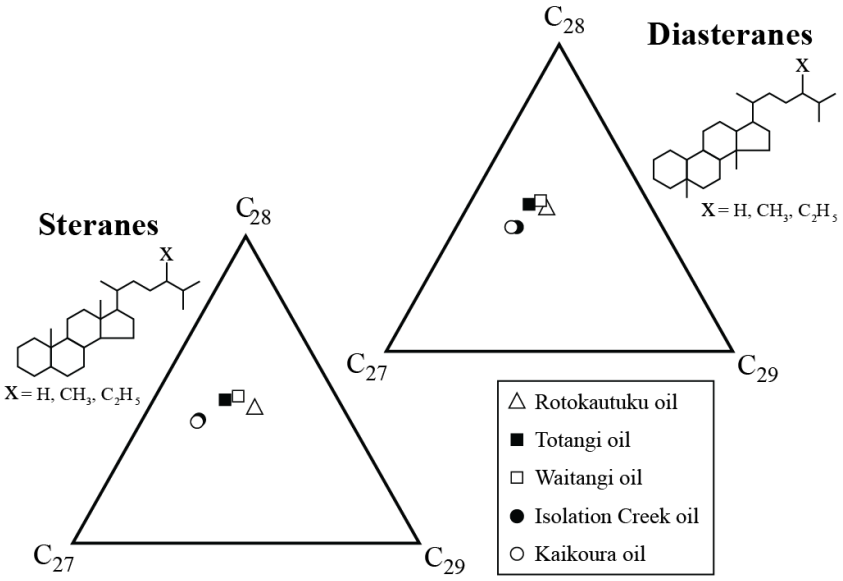

Figure 4. Ternary diagrams show high degree of similarity in the relative abundances of C_{27}, C_{28}, and C_{29} regular steranes versus βα-diasteranes (rearranged steranes); For steranes, C_{27} = Total C_{27} / Total (C_{27} + C_{28} + C_{29}) and so on for C_{28} and C_{29}, for βα-diasteranes, C_{27} = C_{27}/(C_{27} + C_{28} + C_{29}) βα-diasteranes; Determined by GC-MS-MS of oil sample saturate hydrocarbon fractions.

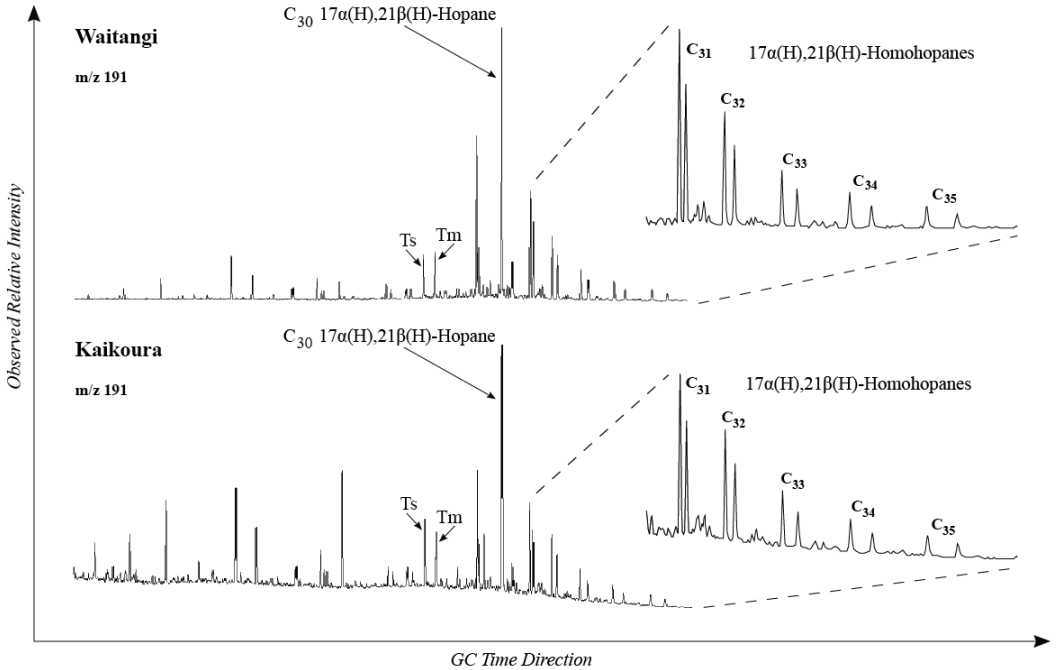

Figure 5. Representative m/z 191 fragmentograms of selected hopane distributions from the Waitangi oil and the Kaikoura oils show good preservation of biomarkers in all five samples. Enlarged region highlights the preservation of the C_{31}-C_{35} 17α(H),21β(H)-homohopanes.

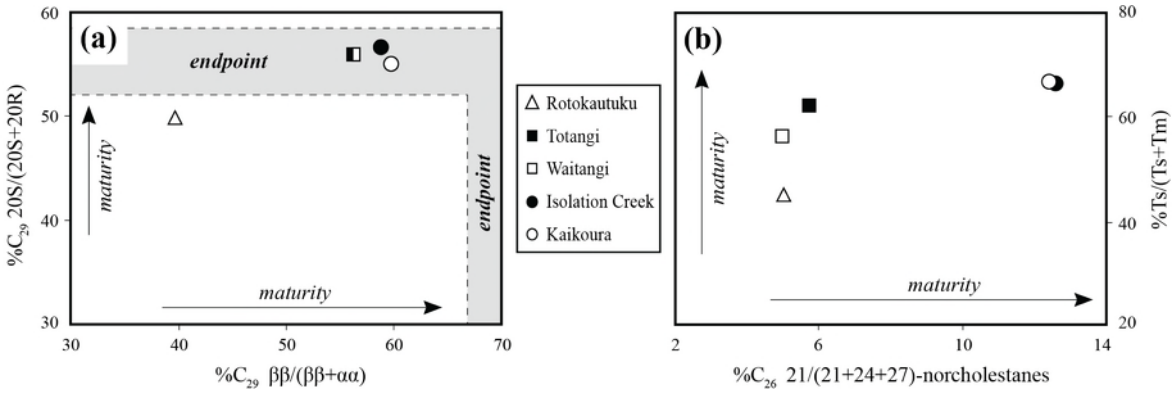

Figure 6. (a) C_{29} sterane isomerization and (b) C_{26} norcholestane versus C_{27} hopane maturity parameters. "Endpoint" areas indicate equilibration of isomerization ratios. All ratios calculated from GC-MS-MS measurements (C_{29} steranes monitored with m/z 400→217, C_{26} norcholestanes with m/z 358→217, and C_{27} hopanes with 370→191).

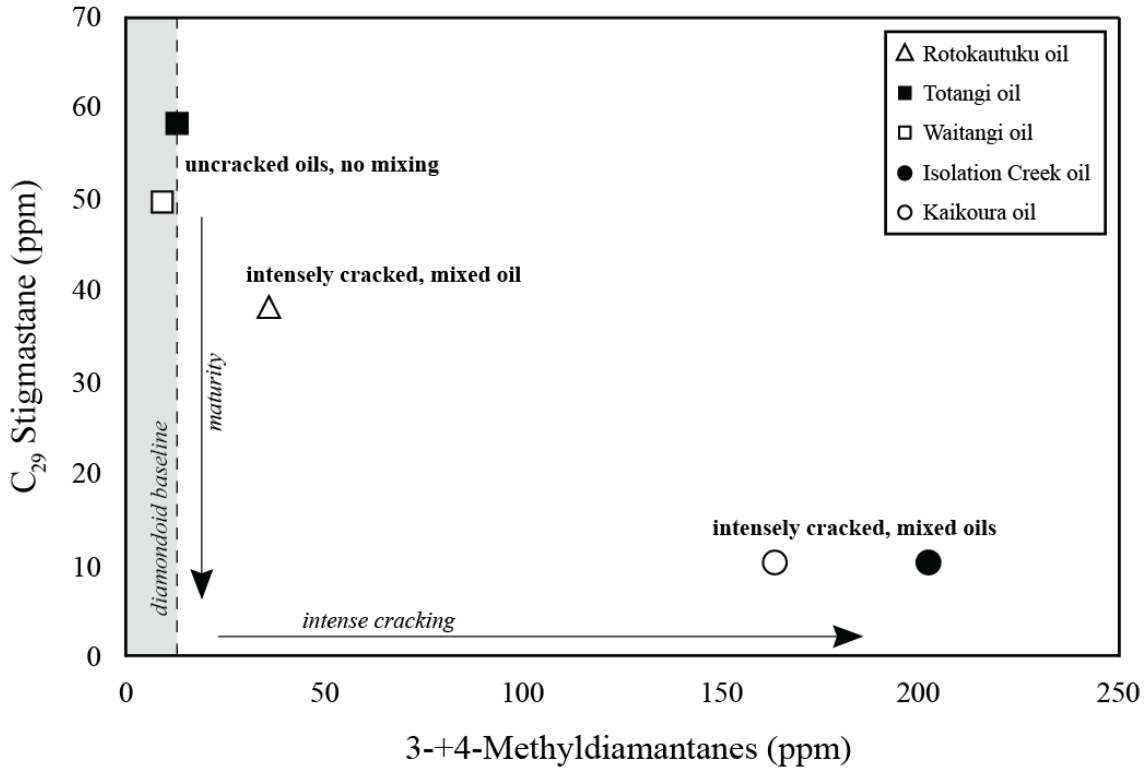

Figure 7. Concentrations of thermally stable diamondoids (methyldiamantanes) versus much less stable biomarkers (stigmastane) indicate thermal maturity and degree of cracking of oils, and reveal petroleum mixtures (e.g., Dahl et al., 1999).

Acknowledgments
This research was funded by the Basin and Petroleum System Modeling (BPSM) Industrial Affiliates Program and by the Department of Energy National Energy Technology Laboratory (DOE NETL). Additional funding provided by the McGee/Levorsen Research Grant of Stanford University. The primary author would like to thank the BPSM group, SPODDS group, BTI Inc., and advisors for support on this project.

References

Behar, F.; Kressmann, S.; Rudkiewicz, J. L.; Vandenbroucke, M., 1992, Experimental simulation in a confined system and kinetic modelling of kerogen and oil cracking: *Organic Geochemistry***,** 19 (1-3*)*, p. 173-189.

Connan, J., 1984, Biodegradation of crude oils in reservoirs, in *Advances in Petroleum Geochemistry*, Vol. 1; Academic Press, London, p. 299-335.

Dahl, J. E.; Moldowan, J. M.; Peters, K. E.; Claypool, G. E.; Rooney, M. A.; Michael, G. E.; Mello, M.R.; Kohnen, M. L., 1999, Diamondoid hydrocarbons as indicators of natural oil cracking: *Nature***,** 399 (6731*)*, p. 54-57.

Demaison, G., The generative basin concept, in *Petroleum Geochemistry and Basin Evaluation*: American Association of Petroleum Geologists, Tulsa, OK, p. 1-14.

Hunt, M. J., 1979, *Petroleum Geochemistry and Geology*: W.H. Freeman, New York

Jones, V. T.; Drozd, R. J., 1983, Predictions of oil or gas potential by near-surface geochemistry: *AAPG Bulletin,* 67 (6), p. 932-952.

Peters, K. E., C. C. Walters, and J. M. Moldowan, 2005, The biomarker guide: Cambridge, U.K., Cambridge University Press, 1155 p.

Seifert, W. K.; Moldowan, J. M., 1979, The effect of biodegradation on steranes and terpanes in crude oils: *Geochimica et Cosmochimica Acta***,** 43 (1*)*, p. 111-126.

Sykes, R., Zink, K. G., Rogers, K. M., Phillips, A., Ventura, G. T., New and updated geochemical databases for New Zealand petroleum samples, with assessments of genetic oil families, source age, facies and maturity: *GNS Science Consultancy Report* 37, xx p. 1-29.

Tissot, B. P., D. H. Welte. *Petroleum Formation and Occurrence*: Springer-Verlag, New York, 617 p.

Uruski, C. I., 2010 New Zealand's deepwater frontier: *Marine and Petroleum Geology***,** 27 (9), p. 2005-2026.

Volkman, J. K.; Alexander, R.; Kagi, R. I.; Rowland, S. J.; Sheppard, P. N., 1984, Biodegradation of aromatic hydrocarbons in crude oils from the Barrow Sub-basin of Western Australia. *Organic Geochemistry***,** 6, p. 619-632.

SOURCE ROCK HETEROGENEITY AND MIGRATED HYDROCARBONS IN THE TRIASSIC SHUBLIK FORMATION AND THEIR IMPLICATION FOR UNCONVENTIONAL RESOURCE EVALUATION IN ARCTIC ALASKA

Inessa A. Yurchenko[1,*], J. Michael Moldowan[2], Kenneth E. Peters [1,3], Leslie B. Magoon[1], Stephan A. Graham[1]
[1]Department of Geological Sciences, Stanford University, Stanford, CA
[2]Biomarker Technologies, Inc., 638 Martin Avenue Rohnert Park, CA
[3]Schlumberger, Mill Valley, CA
*inessa@stanford.edu

Abstract
This organic geochemical study of the Triassic Shublik Formation investigates source rock heterogeneity and vertical variability in organic-richness distribution in the Tenneco Phoenix-1 well (OCS-Y-0338), drilled in offshore Arctic Alaska in 1986. Recovered continuous core is nearly 90 m thick core through the entire Shublik Formation. Guided by previously published analyses of the Phoenix-1 core by Robison et al. (1996), this study provides the most detailed core-based geochemical analysis of the Shublik Formation to date. Analysis of biomarkers and diamondoids combined with Rock-Eval pyrolysis results yields evidence of mature migrated hydrocarbons that may have affected previous interpretations of organic matter type and maturity of this core. Despite the variable lithology, four identified source rock intervals contain oil-prone type I kerogens and are immature to marginally mature. Biomarker analysis indicates the presence of two organic facies deposited under anoxic clay-poor and suboxic clay-rich environments that likely generated genetically distinct oils.

Geological background
Arctic Alaska is one of the world's most petroliferous regions, containing a great share of U.S. energy resources (Bird and Houseknecht, 2011). Nearly all petroleum-producing fields are located in the central North Slope between the National Petroleum Reserve in Alaska (NPRA) to the west and the Arctic National Wildlife Refuge (ANWR) to the east (**Fig. 1A**). The Middle to Upper Triassic Shublik Formation (**Fig. 1B**) is a key source rock in the North Slope of Alaska and the greater Prudhoe Bay Field area. This accounts for nearly all of the oil in the Kuparuk River Oil Field and about a third of the oil in the Prudhoe Bay Oil Field (Peters et al., 2008) (**Fig. 1A**). Although it has been recognized that organic-rich Shublik rocks show variable lithology, the majority of the research historically focused on organic geochemical assessments of Shublik oil types, rather than the source rock itself.

Methodology
Eleven samples from six different lithologies (originally detailed and described by Hulm, 1999) were collected for total organic carbon (TOC), Rock-Eval pyrolysis, carbonate content, elemental analysis (ICP-MS), and analysis of biomarkers and diamondoids (**Fig. 2**). In addition, two selected source-rock samples were analyzed for petroleum generation kinetics using kinetic modeling based on a discrete activation energy distribution using three different pyrolysis heating rates as discussed in Peters et al. (2015).

Moreover, the entire core was scanned using a hand-held XRF Bruker Tracer IV-SD at 0.3-m intervals.

Results and Conclusions

The Triassic Shublik Formation in the Phoenix-1 core was subdivided into four source-rock and two non-source intervals (**Fig. 3**). The presence of mature migrated petroleum from a deeper Shublik source is confirmed by Rock-Eval pyrolysis, as well as analyses of biomarkers and diamondoids. This study documents the excellent potential of the Shublik Formation as an unconventional resource system and provides the first look at expulsion and retention of source units and storage capacity of non-source/reservoir units in this context. Our results show that the presence of previously unrecognized migrated fluids resulted in misleading interpretations of organic matter type and maturity by previous studies (**Fig. 4**).

Despite the geochemical overprint of non-indigenous hydrocarbons, detailed geochemical characterization of immature Shublik core samples from the Phoenix-1 well reveals similar organic matter input and a clear difference in depositional environments between the analyzed samples. The organic matter of the Shublik Formation is dominated by Type I kerogen based on Rock-Eval pyrolysis. The algal contribution of organic matter is supported by biomarker analysis, particularly high tricyclic terpanes concentrations linked to reported widespread occurrence of unicellular algae *Tasmanites* in northern Alaska. Within this Shublik succession, the depositional environment changes from anoxic clay-poor to suboxic clay-rich conditions (**Fig. 5**). This apparently leads to the generation of genetically distinct oils. Kinetic analyses of organofacies end-members suggest different timing of onset and peak of hydrocarbon generation that may have significantly affected generation and expulsion history of mature Shublik source rock, and resultant petroleum migration and filling history of the North Slope oil fields.

Acknowledgments

Support for this study was provided by the Stanford Basin and Petroleum System Modeling (BPSM) Industrial Affiliates Program and Great Bear Petroleum. Special thanks are due to USGS Core Research Center in Denver, Colorado for access to the Phoenix-1 Shublik core for sampling. We thank Bruce Kaiser, Harry Rowe, and Bruker Corporation for discussions and assistance with XRF instrumentation; Agilent Technologies for MassHunter software; and Erik Sperling for ICP-MS analysis. This work benefitted from discussions with Ken Bird and Allegra Hosford Scheirer. We also thank the staff of the Biomarker Technologies, Inc. and Will Thompson-Butler for lab and XRF measurements assistance respectively.

References

Bird, K.J., and Houseknecht, D.W., 2011, Chapter 32 Geology and petroleum potential of the Arctic Alaska petroleum province: Geological Society, London, Memoirs, v. 35, p. 485–499, doi: 10.1144/M35.32.

Hulm, E.J., 1999, Subsurface facies architecture and sequence stratigraphy of the Eileen Sandstone, Shublik Formation, and Sag River Sandstone, Arctic Alaska: Fairbanks, Alaska, Master's Thesis, University of Fairbanks Alaska, 98 p.

Houseknecht, D.W., Bird, K.J., and Garrity, C.P., 2012, Assessment of Undiscovered Petroleum Resources of the Arctic Alaska Petroleum Province Scientific Investigations Report 2012 – 5147, 33 p.

Peters, K.E., Scott Ramos, L., Zumberge, J.E., Valin, Z.C., and Bird, K.J., 2008, De-convoluting mixed crude oil in Prudhoe Bay Field, North Slope, Alaska: Organic Geochemistry, v. 39, p. 623–645, doi: 10.1016/j.orggeochem.2008.03.001.

Peters, K.E., Burnham, A.K., and Walters, C.C., 2015, Petroleum generation kinetics: Single versus multiple heating ramp open-system pyrolysis: AAPG Bulletin, v. 99, p. 591–616, doi: 10.1306/11141414080.

Robison, V.D., Liro, L.M., Robison, C.R., Dawson, W.C., and Russo, J.W., 1996, Integrated geochemistry, organic petrology, and sequence stratigraphy of the Triassic Shublik Formation, Tenneco Phoenix 1 well, North Slope, Alaska, U.S.A.: Organic Geochemistry, v. 24, p. 257–272, doi: 10.1016/0146-6380(96)00023-X.

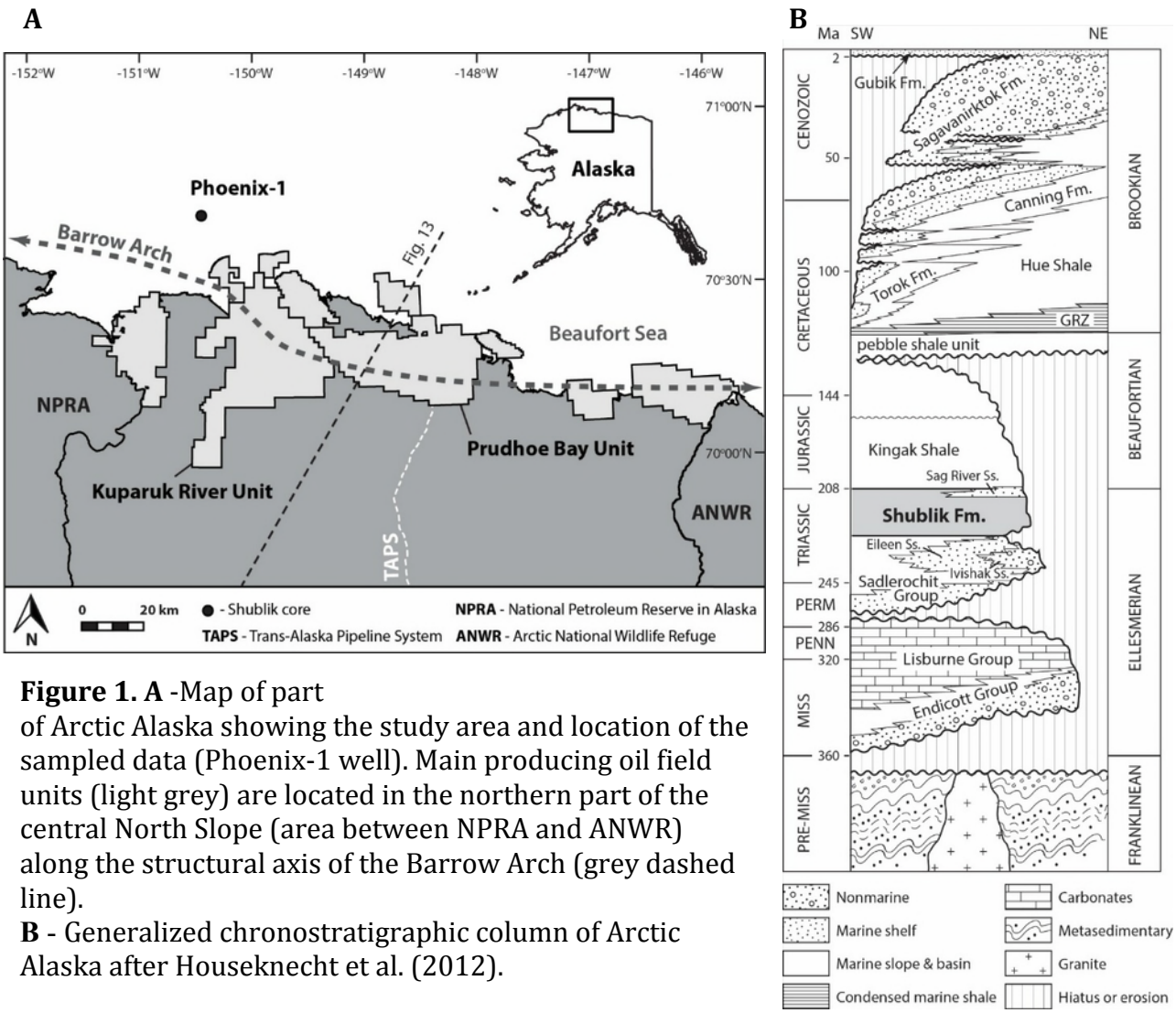

Figure 1. A -Map of part of Arctic Alaska showing the study area and location of the sampled data (Phoenix-1 well). Main producing oil field units (light grey) are located in the northern part of the central North Slope (area between NPRA and ANWR) along the structural axis of the Barrow Arch (grey dashed line).
B - Generalized chronostratigraphic column of Arctic Alaska after Houseknecht et al. (2012).

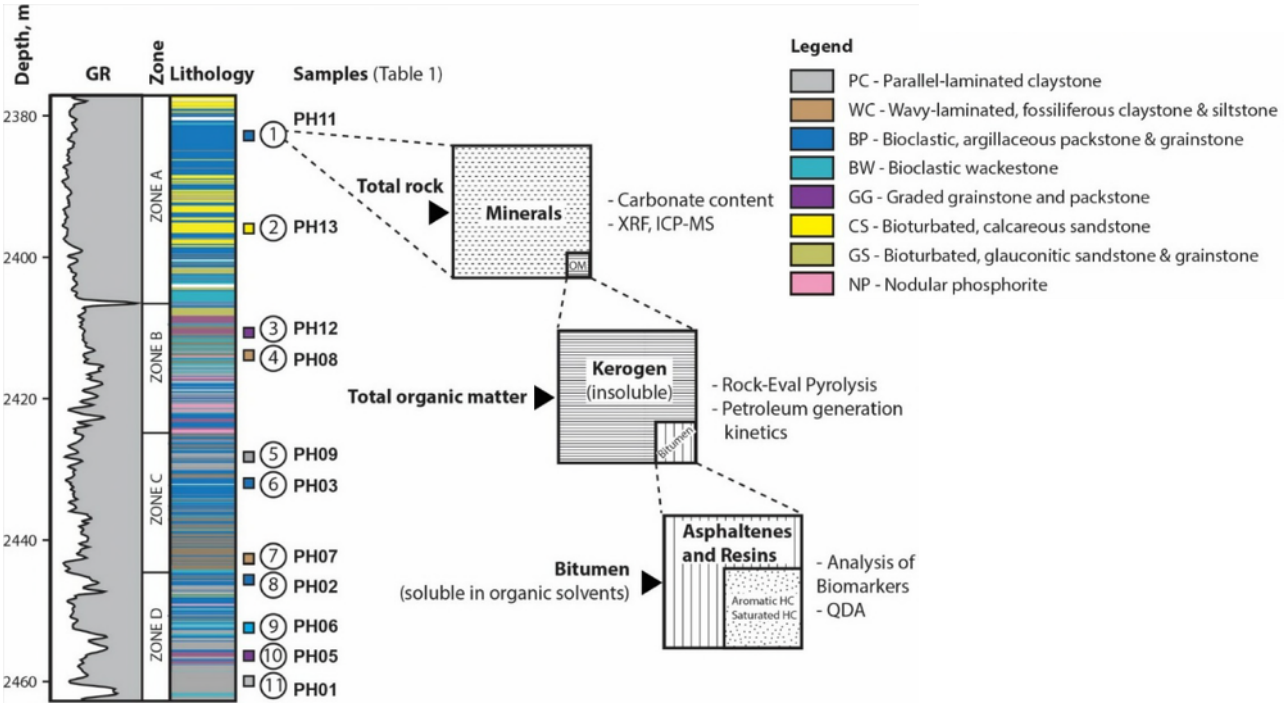

Figure 2. Stratigraphic column of Phoenix-1 Shublik core based on conventional core description by Hulm (1999), lithology and location of collected samples in depth, and analytical methodology.

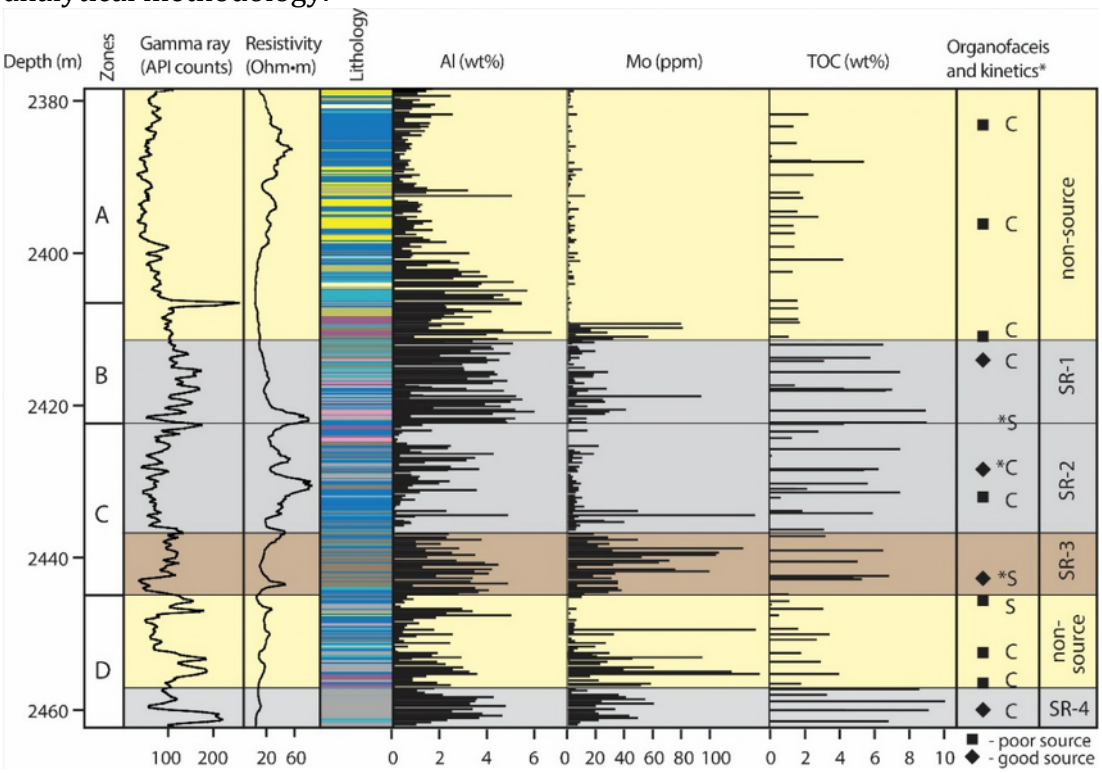

Figure 3. Subdivision of the Shublik Formation into two non-source and four source intervals based on distinctive geochemical and lithologic features and their well-log signatures.

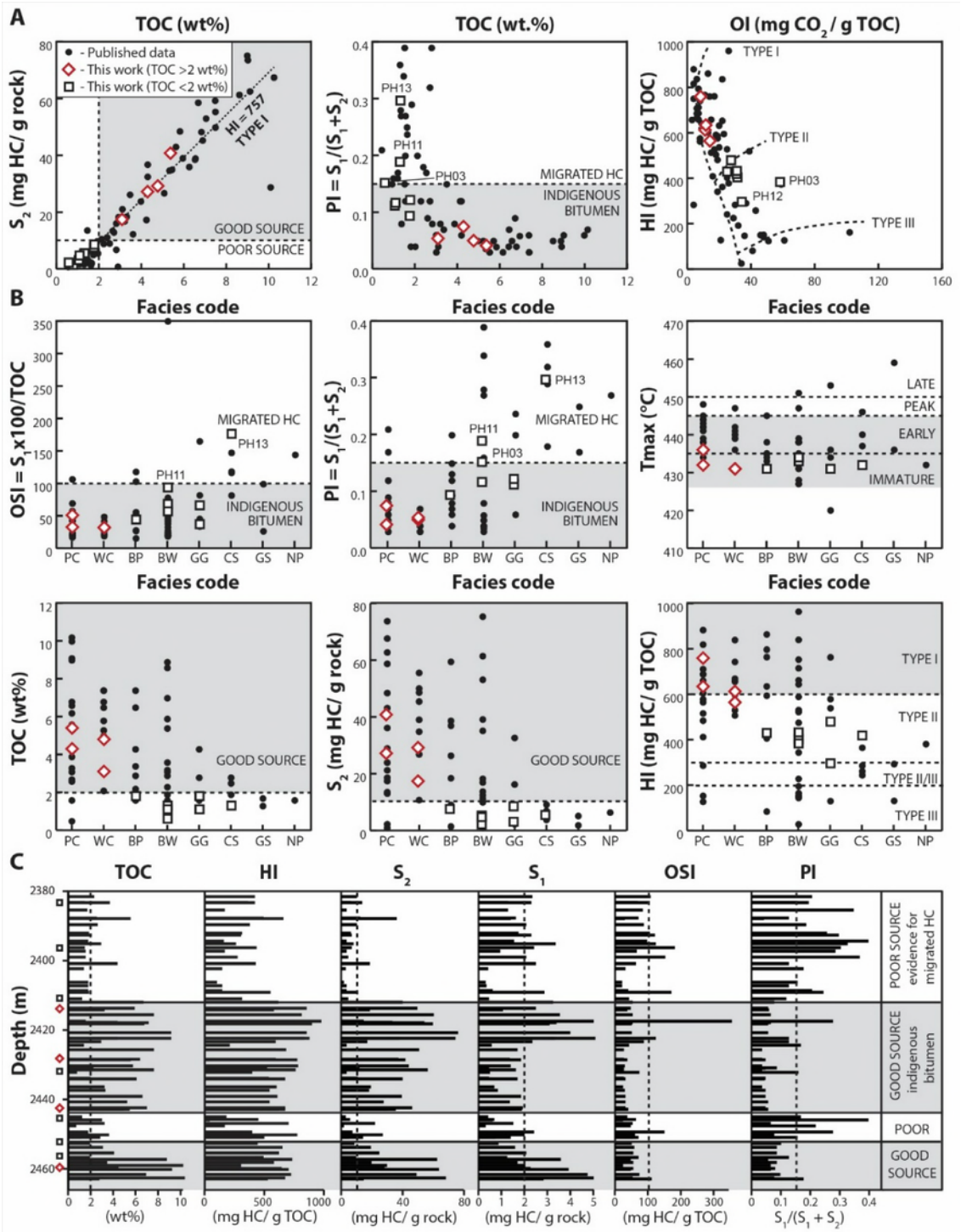

Figure 4. Total organic carbon and Rock-Eval pyrolysis results. **A** – Bulk analysis of organic matter quantity (S_2 vs. TOC plot), quality (HI vs. OI plot) and thermal maturity (PI vs. TOC plot). **B** – Variability of source rock properties by lithology. Lithofacies key is on **Fig. 2**. **C** - Geochemical logs in depth. The selected sample set includes 11 samples collected for this study, as well as 61 core samples previously published data (e.g. Robison et al., 1996).

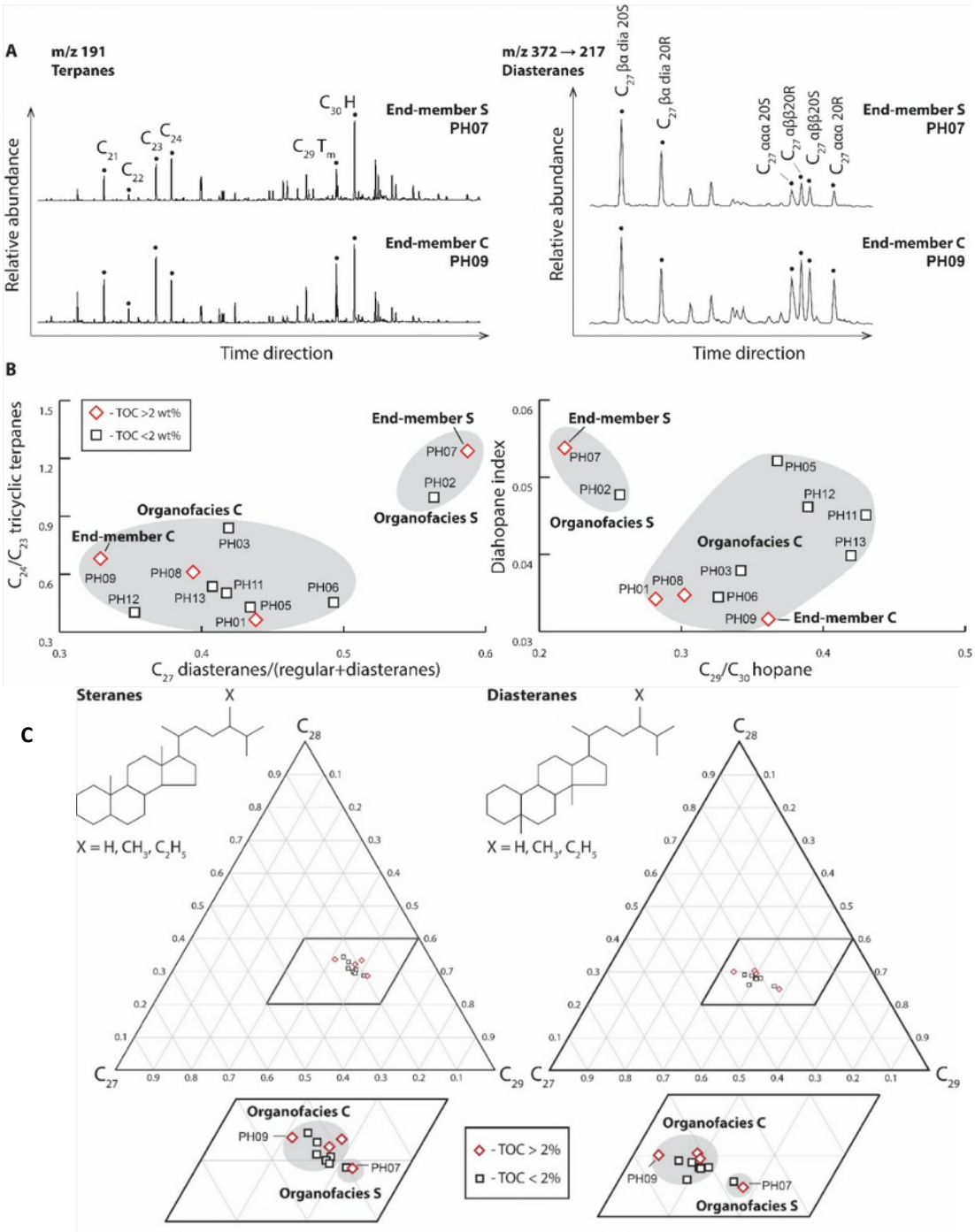

Figure 5. A - Comparison of terpane and diasterane mass chromatograms (m/z 191 and m/z 372 → 217) for organofacies C and S rock extract end-members. **B** - Representative lithology-related biomarkers. Most samples plot in the same group, showing low C_{27} diasteranes/(regular + diasteranes), C_{24}/C_{23} tricyclic terpanes, diahopane index, and high C_{29}/C_{30} hopane values indicative of a carbonate/clay-poor organofacies C. Conversely, samples PH07 and PH02 are interpreted as a shaly/clay-rich organofacies S. **C -** Ternary diagrams of steranes and diasteranes support subdivision of the Shublik core samples into two genetically distinct organofacies.

THE EFFECT OF CHANGES IN PERMEABILITY ON PORE PRESSURE AND PETROLEUM MIGRATION PREDICTIONS IN BPSM

Krongrath Suwannasri[1,*], Noelle Schoellkopf[2] and Allegra Hosford Scheirer[3]
[1]*Department of Geophysics, Stanford University, Stanford, CA*
[2]*Software Integrated Solutions (SIS), Schlumberger, CA*
[3]*Department of Geological Sciences, Stanford University, Stanford, CA*
[*]krath@stanford.edu

Introduction

The current basin and petroleum system modeling (BPSM) workflow benignly accommodates the changes in permeability during thermal maturation by assuming a constant relationship between porosity and permeability. However, recent pyrolysis experiments show that the relationship between porosity and permeability changes throughout the maturation process (Allan 2015; Burnham 2017). Permeability is a primary factor affecting pore pressure and petroleum migration predictions in BPSM; therefore, the simple assumption that the relationship between porosity and permeability remains constant could lead to suboptimal predictions.

Methodology

The goals of this study are to (1) implement a new BPSM workflow using the changing porosity and permeability relationships during the maturation process and (2) compare its predictions of pore pressure and petroleum migration with predictions from the traditional workflow. The data set of the changing porosity and permeability relationships came from pyrolysis experiments on Eagle Ford samples from the immature window to the early oil and all the way through the peak oil, late oil, and gas window as shown in **Figure 1** (Suwannasri et al., 2017). Using this data set, we set up three basin modeling cases for the comparison as listed below.

- Case 1: This case represents the scenario of using measurements from immature outcrop samples to calibrate the porosity-permeability relationship and used that relationship throughout the simulated maturation process.
- Case 2: This case represents the scenario of using the measurements from the well samples to calibrate the porosity-permeability relationship and used that relationship throughout the simulated maturation process.
- Case 3: The porosity-permeability relationship was based on our own custom rock physics measurements from all maturity windows. This case represented the new workflow that uses the changing relationships throughout maturation. Before thermal maturation occurred, the relationship of case 3 is the same as case 1 (**Figure 1**). Upon reaching the gas window, the porosity-permeability relationship changes and approaches case 2 (**Figure 1**).

We ran the three cases on a synthetic 2D model that had the source rock spanning from the immature to the gas window (**Figure 2**). After simulation, we compared the pore pressure and petroleum migration of the three cases.

Results

The results of three cases show different pore pressure and petroleum migration predictions. The overpressure is highest in case 1 and lowest in case 2 (**Figure 3**). The difference is about 500 psi at the deepest point of the section. The overpressure of case 3 is between the first two cases. Conversely, petroleum migration is slowest in case 1 and fastest in case 2. This leads to highest remaining petroleum saturation in case 1 and lowest in case 2. The petroleum saturation in case 3 is between the first two cases.

Summary

We successfully implemented the new BPSM workflow that uses changing relationship between porosity and permeability during maturation. The results show that pore pressure and petroleum migration are predicted differently depending on whether the porosity and permeability relationship is constant or varied.

Acknowledgments

We thank Tiziana Vanorio and Stanford Rock Physics Lab (SPRL) for the experimental results. We also would like to express our gratitude to Tapan Mukerji and Alan Burnham at Stanford University and Adrian Kleine (Schlumberger) for constant support.

References

Allan, Adam M. 2015. "Thermal Maturation-Induced Evolution of the Elastic and Transport Properties of Organic-Rich Shales." Stanford University.

Burnham, Alan K. 2017. "Porosity and Permeability of Green River Oil Shale and Their Changes during Retorting." *Fuel* 203: 208–13. doi:10.1016/j.fuel.2017.04.119.

Suwannasri, K., T. Vanorio, and A. C. Clark. 2017. "Monitoring the Changes in the Microstructure, Elastic, and Transport Properties of Eagle Ford Marl during Maturation." Manuscript in preparation.

Figures

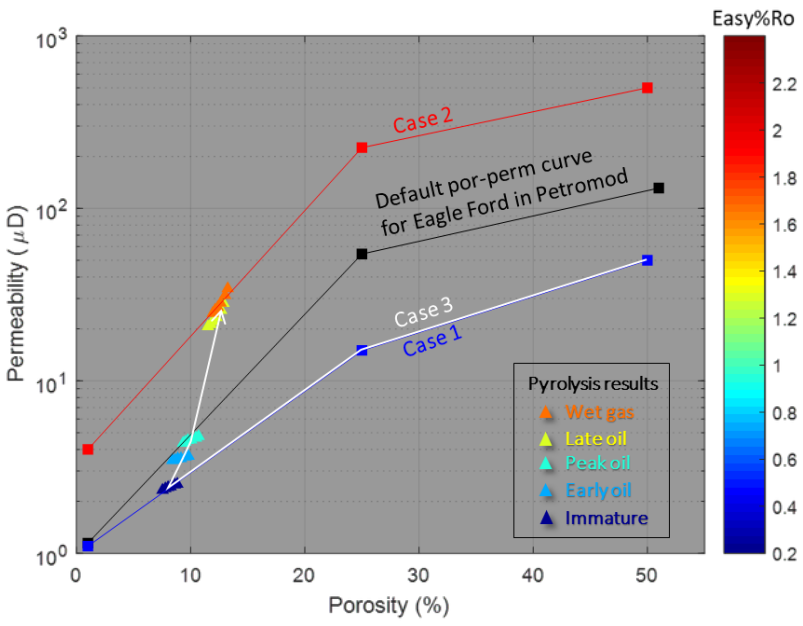

Figure 1. The relationships between porosity and permeability of the 3 cases and the default relationship of the Eagle Ford Shale in PetroMod. Also shown are measured porosity and permeability relationships of the pyrolyzed Eagle Ford sample at different thermal maturity levels, as colored by Easy%Ro values.

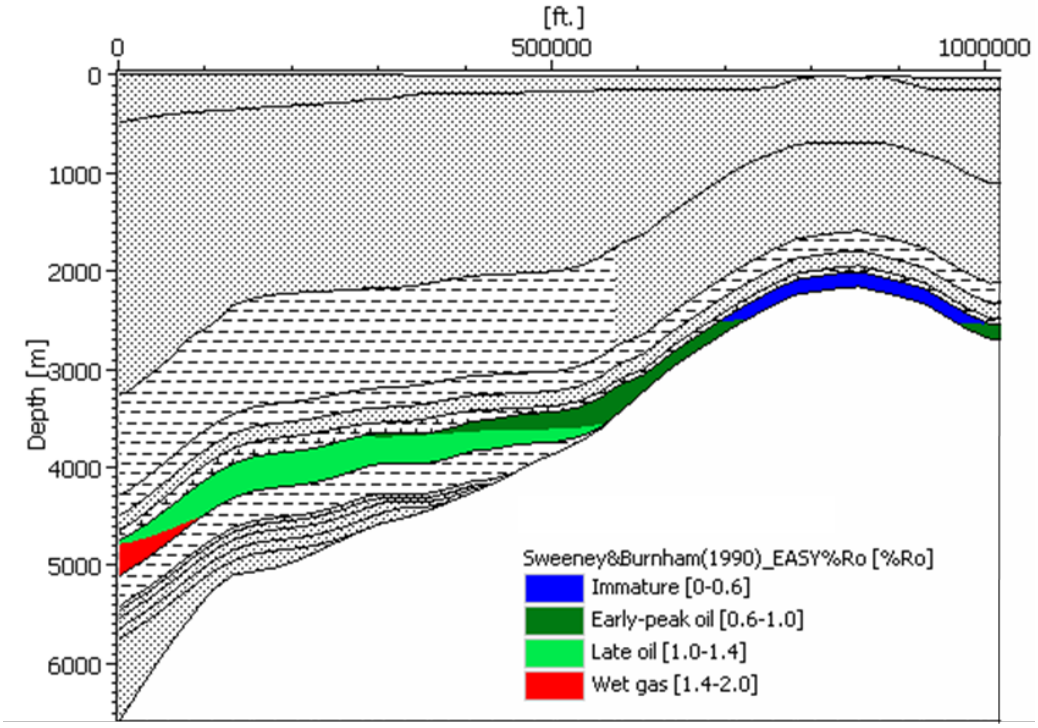

Figure 2. The synthetic 2D model used in this study. The source rock layer spans from immature to wet gas windows.

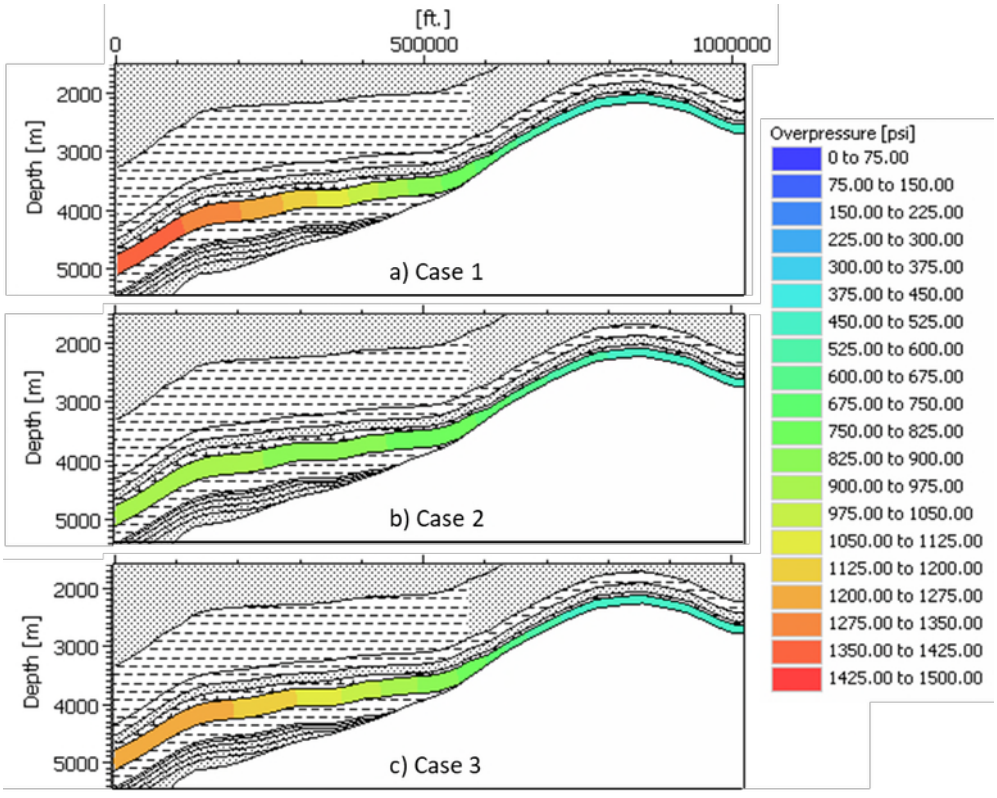

Figure 3. The comparison of overpressure predictions of the three cases. Case 1 has the highest overpressure and case 2 has the lowest. The overpressure in case 3 is in between the first two cases.

BAYESIAN NETWORKS TO QUANTIFY UNCERTAINTY IN BASIN MODELING

Tanvi Chheda[1,*], Jef Caers[1], Tapan Mukerji[2], Allegra Hosford Scheirer[1], and Stephan A. Graham[1]

[1]*Department of Geological Sciences, Stanford University, Stanford, CA*

[2]*Department of Energy Resources Engineering, Stanford University, Stanford, CA*

[*]tanvic@stanford.edu

Abstract

Basin and Petroleum System Modeling (BPSM) couples fluid and heat flow, sediment deposition and compaction, and chemical reactions to quantitatively predict hydrocarbon generation, migration and accumulation, among other things. Given the uncertainty in input parameters of such models, it is important to understand and quantify the uncertainty in predictions such as petroleum volumetric estimates derived from basin model simulations. In addition to this objective that we will refer to as *risking*, we also aim at *understanding* the sensitivity of data and prediction variables to the variation in model parameters, and propose a structured workflow for *calibrating* to the observed data.

In practice, the procedure of variation of model parameters tends not to be systematic and the choice of probable scenarios is often not well quantified (Hantschel and Kauerauf, 2009). The first run is a best guess value of the parameters and the sampling interval is enlarged in subsequent simulations according to calibration data. This practice might find a local optimum but miss a region with parameters that lead to better calibration.

For risking, an experimental design consisting of extremes of the input parameters to predict distribution of output is not sufficient because there might be nonlinear relationships between model parameters and prediction variable, as well as interactions between the parameters. To address this, Wendebourg (2003) presents a Response Surface Modeling workflow, which eliminates least important parameters first with a linear screening design, and then makes a quadratic response surface design with two to three of the most important parameters. This procedure is limited by need for discretization.

Hence, we propose the use of Bayesian networks that can help understand uncertainty as well as complexity by incorporating probability theory and graph theory. The workflow **(Figure 1)** will be as follows:

1. Prior probability distributions are determined by uncertain parameters in the model (eg. TOC - log normally distributed, heat flow - uniform, porosity: Gaussian, fault leakage: scenario based).
2. The parameter space is sampled using Monte Carlo or Latin Hypercube method and multiple basin models are simulated. Data and prediction variables are obtained.
3. These parameters, data, and prediction variables are used to learn conditional probability distributions as inputs for the Bayesian network.
4. Condition on the observed data (eg. vitrinite reflectance, pore pressure) to obtain posterior distribution of parameters.
5. Use the posterior to obtain prediction variables with reduced uncertainty. Query what-if scenarios, value of information, and chance of success correlations between multiple segments of a prospect if present.

In addition to the workflow outlined above, we will experiment with sequential sampling by likelihood weighing, or by Markov Chain Monte Carlo method such as Gibbs sampling. Martinelli et al. (2013) assume a known Bayes net structure with charge, reservoir and trap elements **(Figure 2)**. In this study, we will try the following different cases to create a Bayes net:

1. Known or given structure (from geologic knowledge), similar to Martinelli et al. (2013), but with mixed priors, as opposed to categorical only;
2. Learn the structure from data by finding the graphical structure G that maximizes P(G|D), where D represents the available data. It will not assume a structure a priori, but use maximum likelihood approach to find the graphical structure that maximizes Bayesian network score by searching the model space.

This Bayesian network framework will allow propagation of evidence (data collected) to update our prior beliefs of geologic and geophysical assumptions about the model, determine the value of gathering more data, and quantitatively streamline risk evaluation for decision making.

Figures

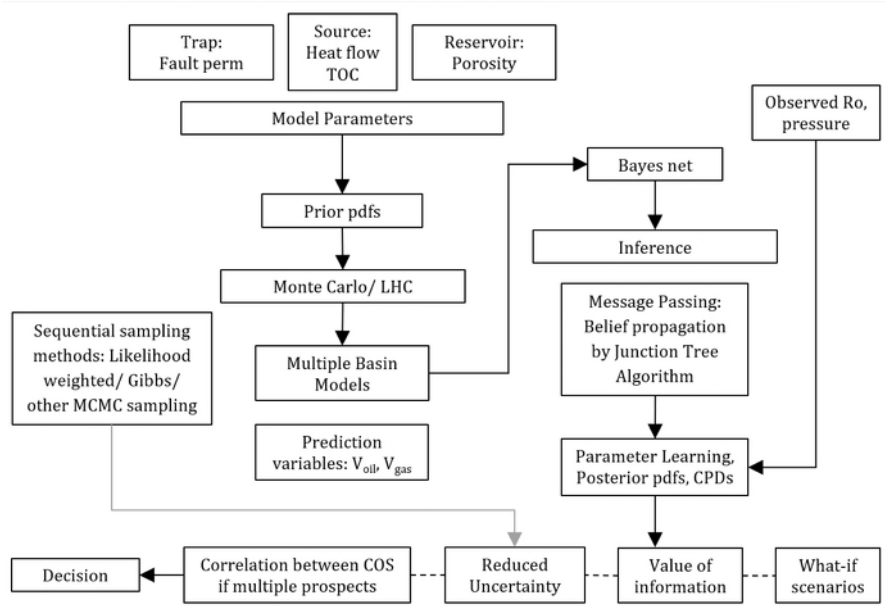

Figure 1. Strategy for risking, understanding, and calibrating basin modeling simulations.

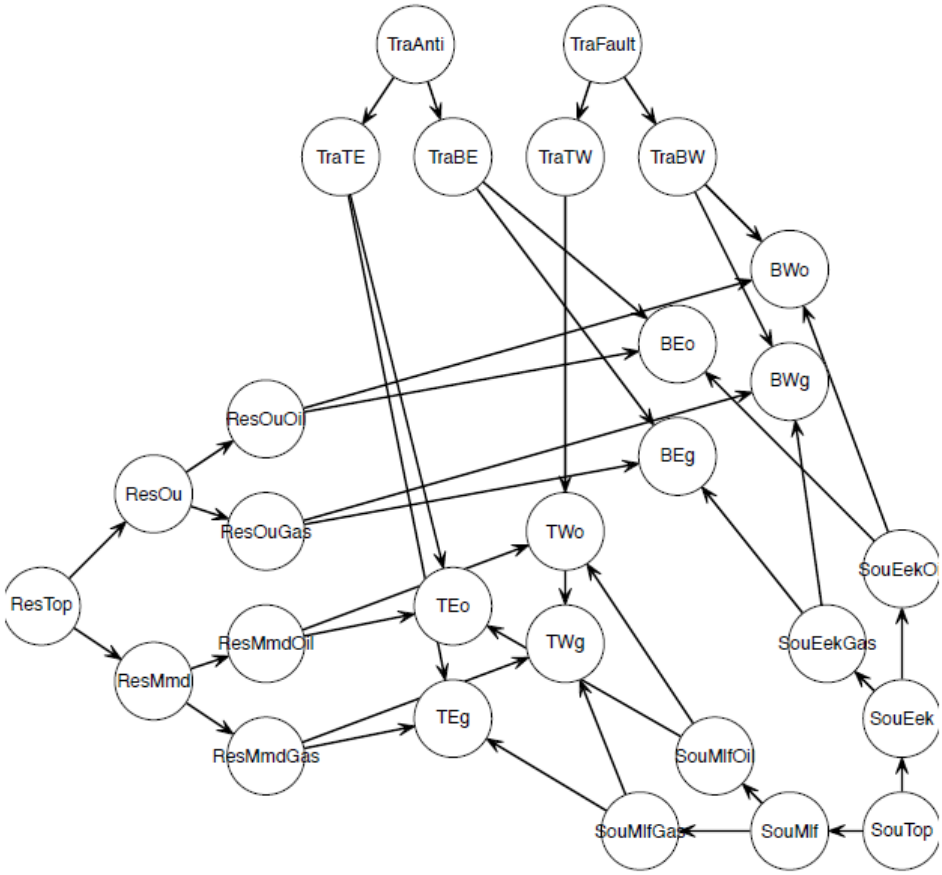

Figure 2. Bayes net with trap (top), reservoir (left) and source (lower right) branches. Top nodes are all discrete, whereas bottom nodes are Gaussian. From Martinelli et al. (2013).

References

Wendebourg, J. (2003). Uncertainty of Petroleum Generation Using Methods of Experimental Design and Response Surface Modeling: Application to the Gippsland Basin, Australia. AAPG/Datapages Discovery Series, 7, 295–307.

Hantschel, T., and A. I. Kauerauf, 2009, Fundamentals of basin and petroleum systems modeling: Berlin, Springer-Verlag, 476 p.

Martinelli, G., Eidsvik, J., Sinding-Larsen, R., Rekstad, S., & Mukerji, T. (2013). Building Bayesian networks from basin-modelling scenarios for improved geological decision making. Petroleum Geoscience, 19(3), 289–304.

Scheidt, C., Li, L., & Caers, J. (In press). Quantifying Uncertainty in Subsurface systems.

INTEGRATED CONSTRAINTS FOR BASIN MODELING AND SEISMIC IMAGING: APPLICATION TO THE NORTHERN GULF OF MEXICO

Anshuman Pradhan[1,*], Allegra Hosford Scheirer[2], Nader C. Dutta[3], Wisam H. AlKawai[2], Huy Q. Le[3] and Tapan Mukerji[1]

[1]*Department of Energy Resources Engineering, Stanford University, Stanford, CA*

[2]*Department of Geological Sciences, Stanford University, Stanford, CA*

[3]*Department of Geophysics, Stanford University, Stanford, CA*

[*]pradhan1@stanford.edu

Abstract

Basin modeling simulates burial history by constructing present day and paleo geometries of stratigraphic horizons (Hantschel and Kauerauf, 2009). Present-day stratigraphic horizons are often identified in 2D or 3D seismic data. Then, paleo geometry of stratigraphic horizons is obtained through applying vertical backstripping or imposing structurally restored sections on the model of areas with structural complexity. Interpreting stratigraphic horizons in a seismic image is highly dependent on the velocity model used for seismic depth migration or the imaging algorithm used. Variations in these interpreted horizons impacts the reconstruction of structural evolution of the basin and consequently modeling thermal or pressure history. Thus, the seismic imaging workflow can significantly change the outputs of a basin model. On the other hand, seismic imaging itself is strongly controlled by the geohistory of the basin because compaction and diagenesis of sediments can affect the values of seismic velocity in the subsurface. Traditional basin modeling and seismic imaging workflows are not integrated to ensure consistency.

In this work, we employ an integrated workflow similar to those of Petmecky et al., (2009), De Prisco et al., (2014), AlKawai and Mukerji (2016) and Pradhan et al. (2017) to address this lack of consistency (Figure 1). The workflow starts with basin modeling to obtain outputs like pore pressure and porosity. These outputs are subsequently linked to rock properties such as seismic velocity and Thomsen's anisotropic parameters through a rock physics model (Dutta 2016). Accounting for uncertainties in basin or rock physics models facilitates the generation of multiple realizations of anisotropic velocity models, all of which embody information about the geohistory of the basin. These realizations of velocity models serve the purpose of improving the constraints on the velocity inversion scheme and ultimately obtaining a robust seismic image. It should be noted that the earlier work did not carry through the entire iteration process as indicated in Figure 1.

The study area includes parts of Ship Shoal (SS) and South Timbalier (ST) protraction areas and is imaged with a 3D seismic survey known as E-Dragon II. Horizons were interpreted in the 3D post-stack seismic volume based on biostratigraphic data in deep industry wells in the blocks SS 188, SS 190 and SS 191 as depth ties (Figure 2). The seismic data images to a depth of 15,000 meters and the key wells penetrated a zone of a total depth of 7,000 meters extending to the Miocene. We interpreted the following horizons: top of Pliocene, top Miocene, mid Miocene (Tortonian) and the top and base of allochthonous salt. In this study, we focused on an arbitrary 2D line extracted from the 3D seismic volume (Figure 2).

The key structure on this line is a listric normal fault that dips basinward and soles into an extruded shallow salt weld. This structure is analogous to what Schuster (1995) referred to as a roho system, which he observed in this area and in other parts of the northern Gulf of Mexico. The presence of salt related structures necessitates the application of palinspastic restoration techniques to rigorously model the effect of salt related structural deformation. The sequential structural restoration workflow accounted for compaction of sediments, Airy isostasy, displacement along the fault plane, and deformation of stratigraphic layers due to salt withdrawal. The deformation due to salt withdrawal was addressed by employing the concept of a regional datum (Marshak and Woodward, 1988; Rowan (1993). Unfolding the layers above salt to a regional datum creates an extra space, which is assumed to correspond to salt withdrawal. For restoring each layer, we used the water depth in an area of the section that seemed to be least affected by salt movement as a consistent estimate for the regional datum.

Figure 3 depicts the restored sections at present day, 2.6 Ma, 5.3 Ma and 7.2 Ma. The restored section at 7.2 Ma shows the presence of a shallow salt canopy that is characterized by some topographic relief and approaches the sediment surface in some areas. The later sections suggest salt withdrawal from the northern portion of the canopy in response to high flux of sediments. The extruded salt from the welded northern portion of the canopy potentially supplied salt into the rising diapir to the south. Evacuation of salt from the welded part of the canopy results in gravitational gliding of sediments, which is accommodated with the development of the roho system.

The restored sections were imposed on the basin model to define paleo-geometry of stratigraphic layers in the basin model. We imported the restored geologic sections from Midland Valley Move software to PetroMod as a TecLink model. We defined the stratigraphic layers in the basin model to be identical to those in the present-day section in Figure 3. The restored sections used to construct the 2D basin model captures key episodes of salt withdrawal and development of the roho system. Lithologies were defined and assigned based on the gross shale content for each layer obtained from gamma-ray logs. The paleo-water depth was assigned to ensure consistency with each of the restored sections. We calibrated the model with bottom hole pressure data from an intersecting well. Figure 4 shows the simulated present day pore-pressure section.

The outputs of the basin modeling such as pore pressure and porosity section will be transformed into an anisotropic velocity section using rock physics models (Pradhan et. al., 2017; Dutta, 2016). This section will constrain anisotropic full-waveform velocity inversion and generate a new seismic image, which we will show at the meeting. Re-interpretation of this image can facilitate updating the basin model in an iterative manner.

Figures

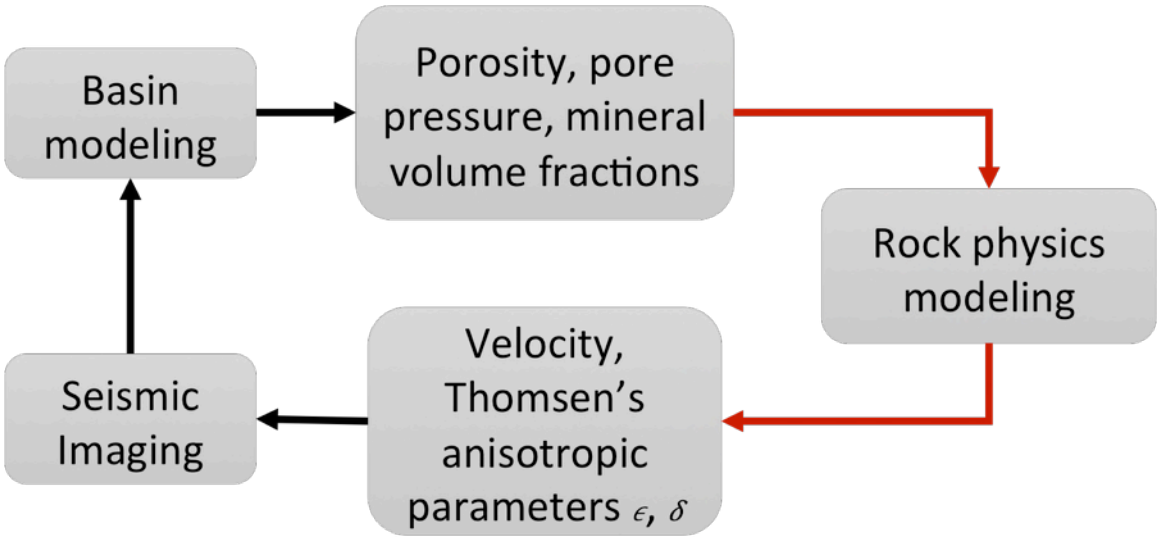

Figure 1. Components of the new integrated workflow

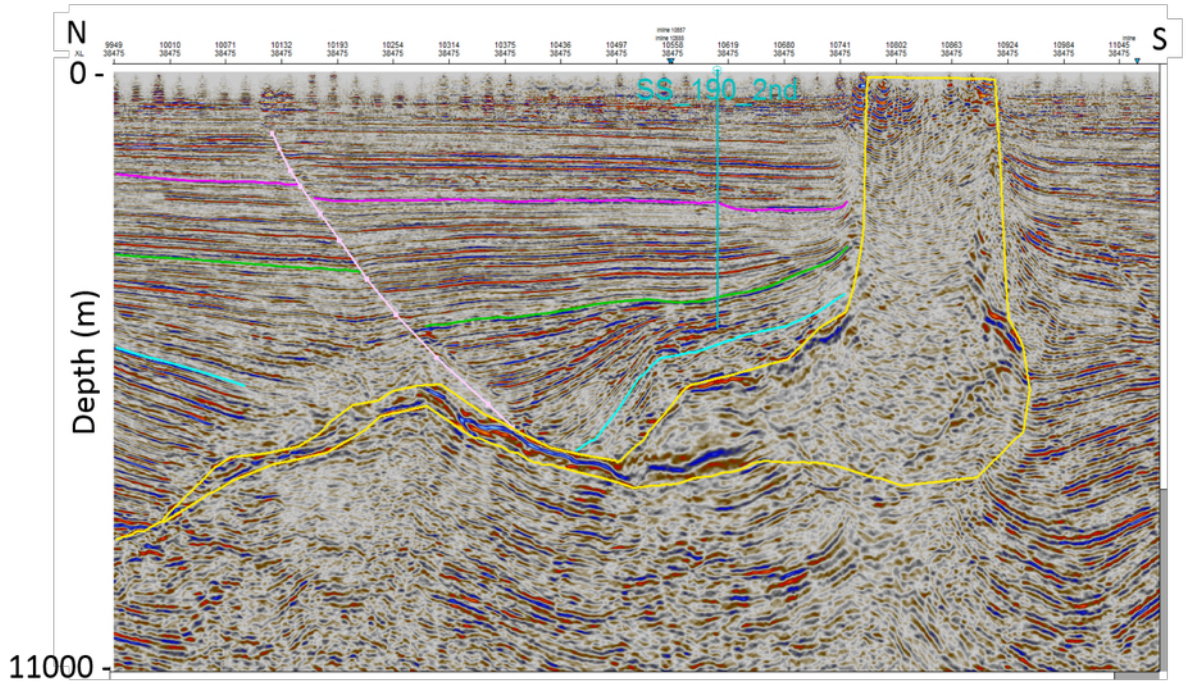

Figure 2. Horizon interpretations on a 2D section. The interpreted lines are for tops Pliocene (magenta), Miocene (green), mid-Miocene (blue), salt (yellow) and a listric fault (pink). The well in block SS_190 is overlain.

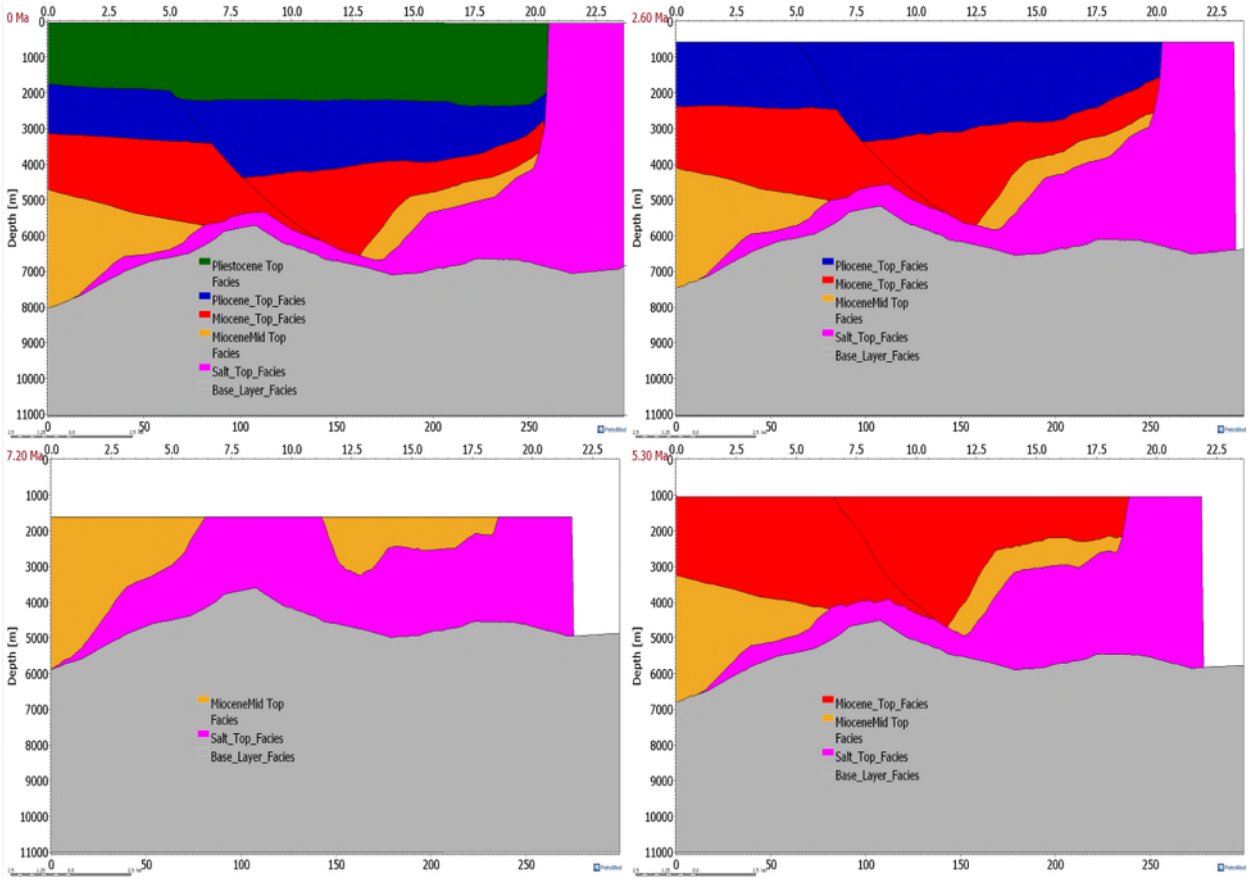

Figure 3. Palinspastic restoration of the section. The ages of the sections are present day, 2.6, 5.3 and 7.2 Ma clockwise from top left.

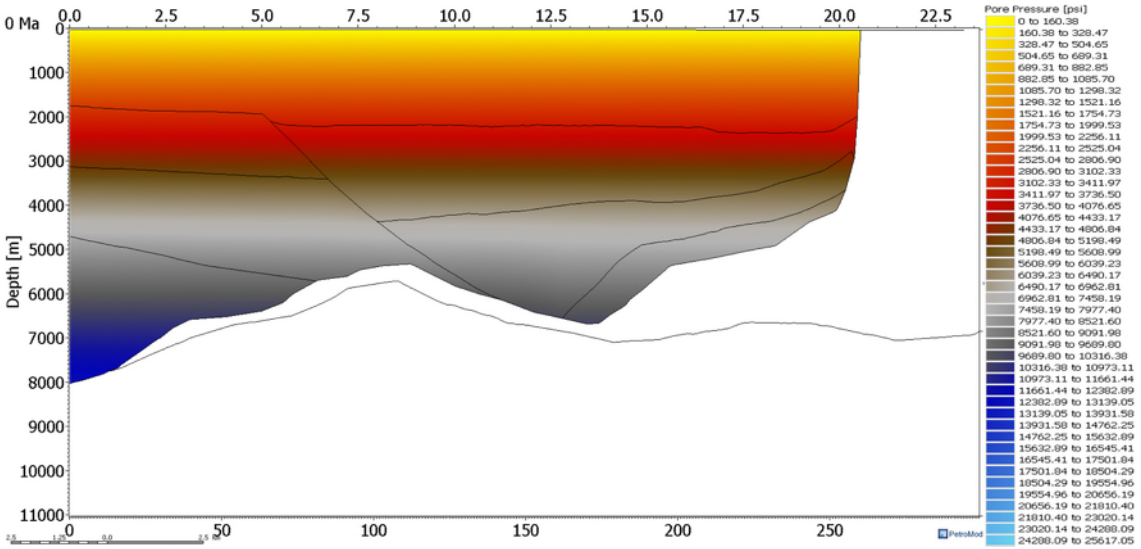

Figure 4. Present day pore-pressure cross-section

Acknowledgments
We gratefully acknowledge Schlumberger for donating PetroMod software, Midland Valley for Move software, and Lexco for access to the OWL database.

References
AlKawai, W., and T. Mukerji, 2016, Integrating basin modeling with seismic technology and rock physics: Geophysical Prospecting, v. 64, 1556-1574.

De Prisco, G., Thanoon, D., Bachrach, R., Brevik, I., Clark, S. A., Corver, M. P., Pepper, R. E., Hantschel, T., Helgesen, H. K., Osypov, K., and Leirfall, O. K., 2015, Geophysical basin modeling: Effective stress, temperature, and pore pressure uncertainty. Interpretation, 3(3), SZ27-SZ39.

Dutta, Nader C., 2016, Effect of chemical diagenesis on pore pressure in argillaceous sediment, The Leading Edge, p. 523 – 527, doi.org/10.1190/tle35060523.1.

Hantschel, T., A. Kauerauf, 2009, Fundamentals of basin modeling: Berlin, Springer-Verlag, 425 p.

Marshak, S. and N.B. Woodward, 1988, Introduction to cross-section balancing, in S. Marshak, and G. Mitra, eds., Basic methods of structural geology: Englewood Cliffs, Prentice Hall, p. 303-332.

Petmecky, R. S., M. L. Albertin, and N. Burke, 2009, Improving subsalt imaging using 3D-basin modeling derived velocities: Journal of Marine Petroleum Geology, 26, 457–463, doi: 10.1016/j.marpetgeo.2009 .01.011.

Pradhan, A., Mukerji, T., and Dutta, N., (2017), Effect of compaction and smectite-illite transition on velocity anisotropy. SEG Technical Program Expanded Abstracts 2017: pp. 452-457. https://doi.org/10.1190/segam2017-17789338.1

Rowan, M. G., 1993, A systematic technique for the sequential restoration of salt structures: Tectonophysics, v. 228, p. 331–348, doi:10.1016/0040-1951(93)90347-M.

Schuster, D. C., 1995, Deformation of allochthonous salt and evolution of related salt–structural systems, eastern Louisiana Gulf Coast, *in* M. P. A. Jackson, D. G. Roberts, and S. Snelson, eds., Salt tectonics: a global perspective: AAPG Memoir 65, p. 177-198

COMBINING STATISTICAL ROCK PHYSICS AND PRESSURE AND THERMAL HISTORY MODELING TO MAP RESERVOIR LITHFACIES IN THE DEEPWATER GULF OF MEXICO

Wisam H. AlKawai[1,*], Tapan Mukerji[2], Allegra Hosford Scheirer[1] and Stephan A. Graham[1]
[1]Department of Geological Sciences, Stanford University, Stanford, CA
[2]Department of Energy Resources Engineering, Stanford University, Stanford, CA
[*]walkawai@stanford.edu

Summary

This study integrates statistical rock physics with pressure and thermal history modeling for quantitative seismic interpretation workflows. We model pressure and thermal history with a 2D basin model intersecting two wells across the turtle structure of Thunder Horse mini-basin. In the subsequent parts, we combine the basin modeling simulations of effective stress and smectite to illite transformation with statistical rock physics to test how lithofacies elastic properties may be extrapolated away from the wells. This extrapolation extends the training data within the geologic context, and serves the purpose of constraining the background model for seismic inversion. To assess the value added by the basin-modeling guided extrapolation to the quantitative seismic interpretation workflow, we establish a base case that is based on actual data from both wells. We also ran two other quantitative seismic interpretation scenarios that are based only on one well, with and without the guided extrapolations. The scenario with guided extrapolations shows improvement in capturing the spatial trends of elastic properties in the extended training data and derived distributions. The inverted impedances volumes are also improved when compared to the other scenario limited to one well without geological extrapolation. Furthermore, the scenario with the extrapolation result in a lithofacies map nearly identical to that obtained from the base case.

Introduction

Quantitative seismic interpretation (QSI) combines rock physics, statistics and information theory to address uncertainties in predicting lithofacies of heterogeneous reservoirs (Mukerji et al., 2001; Avseth et al., 2005). A key aspect of QSI is extrapolating beyond well control to honor spatial trends of elastic properties and fluid saturations in the subsurface. Extrapolating beyond well control requires knowledge about geologic processes affecting the elastic properties in the subsurface.

Basin and petroleum system modeling (BPSM) can simulate pressure and thermal history after accounting for the geologic factors of deposition, erosion, subsidence, salt tectonism and uplift through the geologic history of the basin (Al-Hajeri et al., 2009; Hantschel and Kauerauf, 2009; Peters, 2009). In this study, we integrate BPSM results with statistical rock physics models to derive pseudo logs of seismic velocities and density away from the vicinity of wells. These pseudo logs serve the purpose of extending training data and constraining the impedance inversion background model. We emphasize on the value added to mapping reservoir lithofacies maps by QSI, using the basin-model guided extrapolations.

Methods

We first modeled pressure and thermal history by building a 2D basin model across the turtle structure of Thunder Horse mini-basin that intersects two wells, one from Thunder Horse Field (i.e., Well A) and the other from Thunder Horse North Field (i.e., Well B). We restricted calibrating the model pressure and thermal history to Well B only to show applicability in the case of limited well control. The seismic attributes used in QSI workflows presented in this study are acoustic impedance and far angle (36º) elastic impedance (Connolly, 1999).

For the purpose of testing the extrapolation scenario, we built a set of rock physics models linking porosity, effective stress and impedance. We defined and calibrated these models based solely on Well B. In the subsequent parts, we applied the rock physics models along with the BPSM pressure and thermal history results to derive pseudo logs of *Vp*, *Vs* and density in Well A based on the porosity and effective stress conditions there. We combined these pseudo logs with actual logs in Well B to extend the training data and condition the background models for seismic inversion. Then, we mapped reservoir lithofacies for the base case (i.e., QSI is based on actual data from both wells), the extrapolation case (i.e., actual data in Well B and extrapolation in Well A), and the other scenario that is based solely on Well B without BPSM guided extrapolation.

Results

We defined rock physics models that describe porosity compaction with effective stress and porosity-velocity relationship for both sandstone and shale. We also distinguished between smectitic and illitic shale based on the basin modeling simulation of illitic molar fractions. The goal is to derive porosity based on effective stress and calculate velocity and density from the derived porosity values. We applied the bootstrap technique to account for uncertainty in the rock physics models. Examples of the models used in the template are shown in Figure 1. In these models for shale, we assigned bulk moduli and shear moduli for smectite and illite respectively based on the data of Wang et al. (2001). We also assumed mineral matrix densities of 2.69 g/cm^3, 2.35 g/cm^3 and 2.62 g/cm^3 for sandstone, smectitic shale, and illitic shale to calculate density based on porosity.

The probability density functions (pdfs) of lithofacies impedances in Figure 2 show increase in impedance in Well A compared to the impedances in Well B. The BPSM-guided extrapolation of the rock properties based on the rock physics models gave us the derived distribution of lithofacies impedance in Well A. These derived distributions are close in their impedance values to those obtained at the same well location from actual data in the base case (Figure 2). These PDFs were estimated by kernel smoothing of impedances distributions. The impedances distributions were obtained from correlated Monte Carlo Simulation of *Vp*, *Vs* and density in which 10,000 samples of each variable were drawn.

In the seismic inversion, we ran model-based inversion. We started the inversion by optimizing the wavelet and the inversion input parameters. We checked the frequency spectrum of the original seismic data to ensure proper high cut filtering of the background models at 10 Hz. Incorporating the BPSM extrapolation in Well A into the impedance background model improves the correlation between the inverted impedances at the well

location and the acoustic impedances derived from the well-log data as can be seen in the acoustic impedance inversion example in Figure 3.

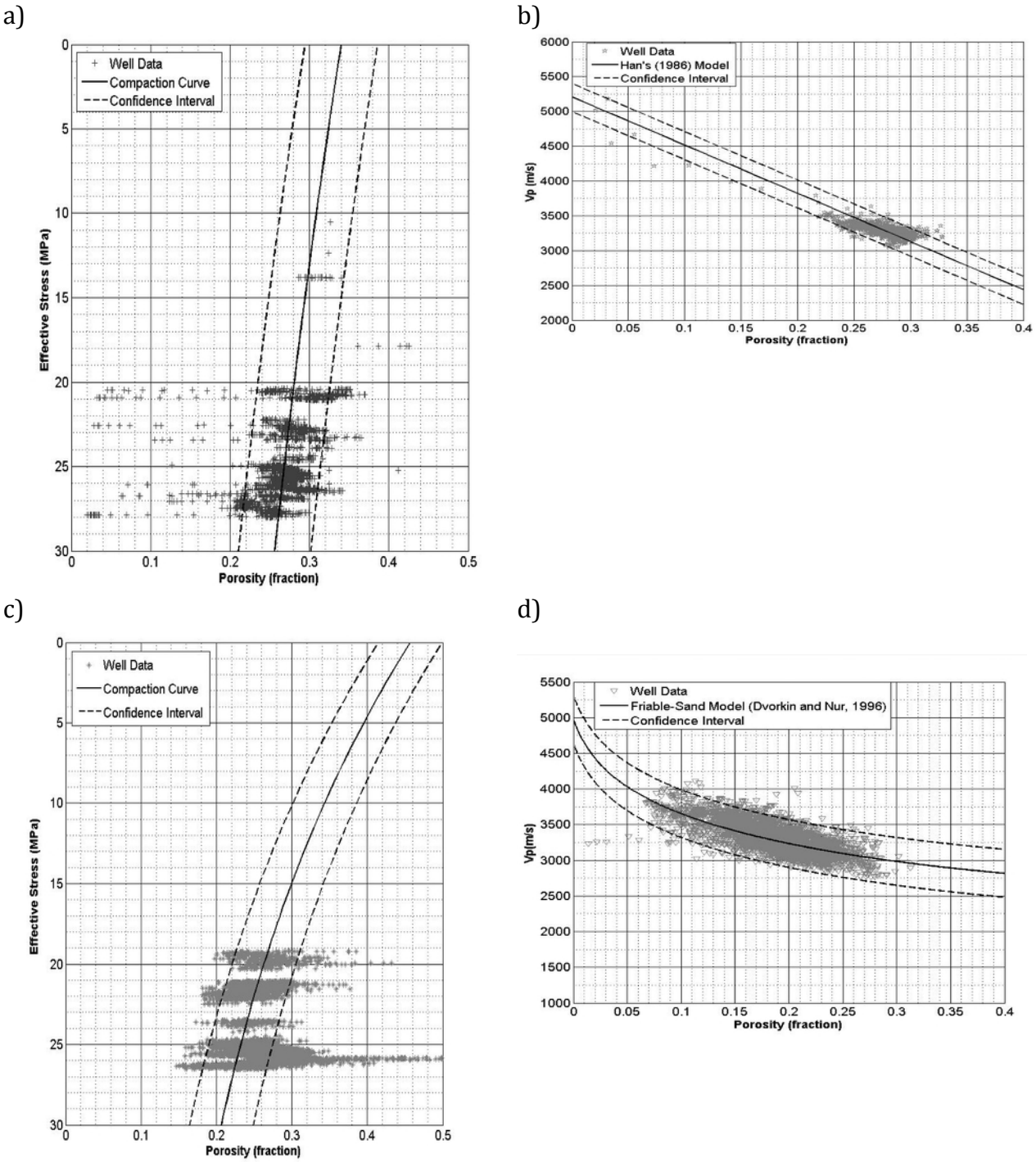

Figure 1. Rock physics models for sandstone (a and b), smectitic shale (c and d) and illitic shale (e and f).

e)

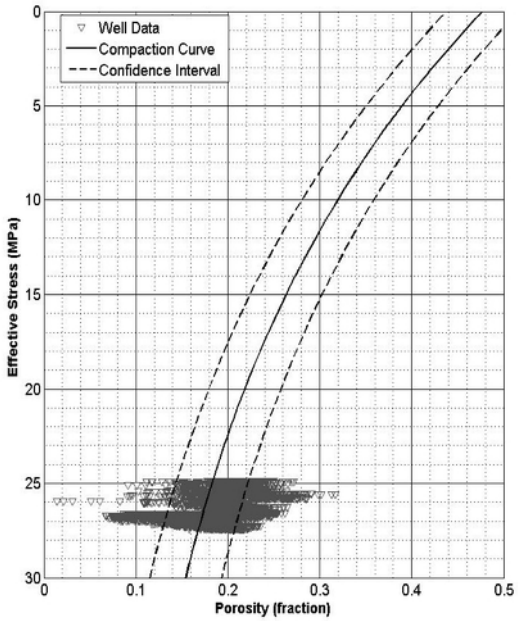

f)

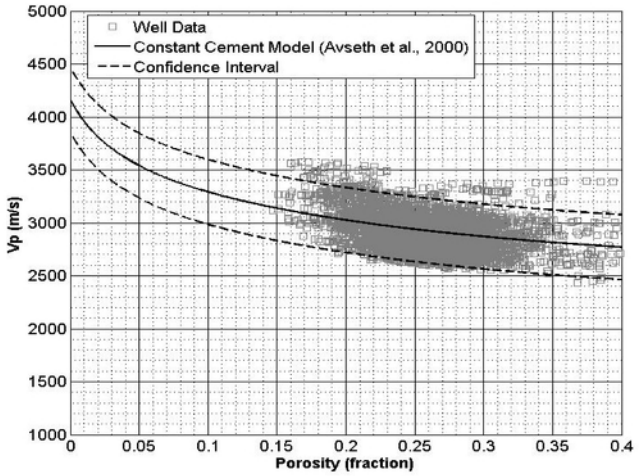

a) Actual PDFs in Well B

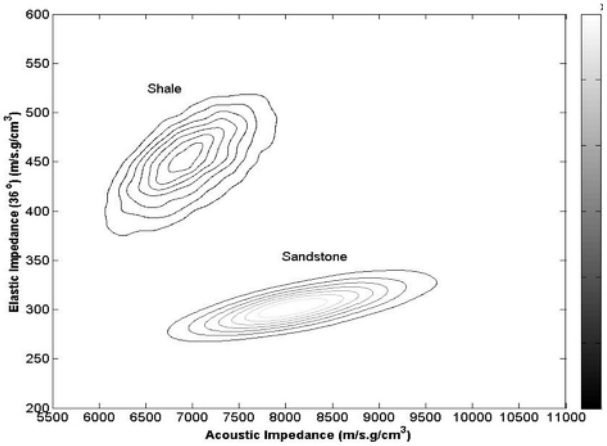

b) Actual PDFs in Well A

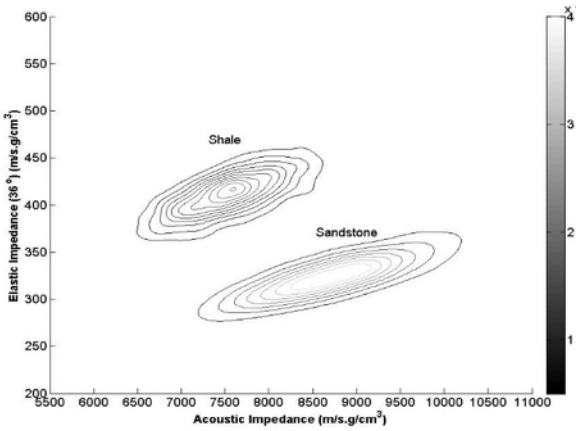

c) BPSM- extrapolations of PDFs in Well B

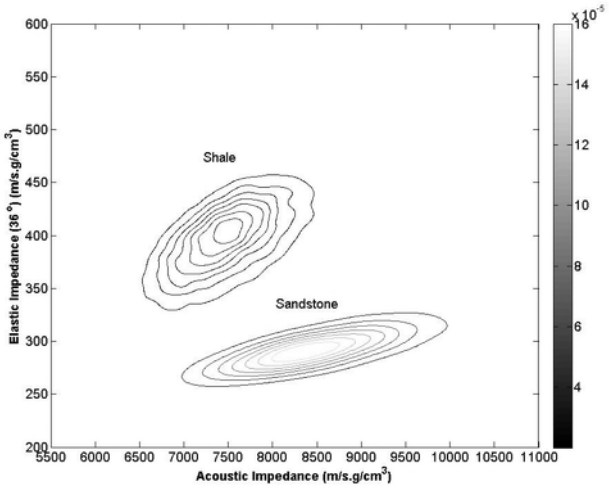

Figure 2. Comparison between actual impedance PDFs in Well B (a), actual PDFs in Well A (b) and BPSM estimated PDFs in Well A (c).

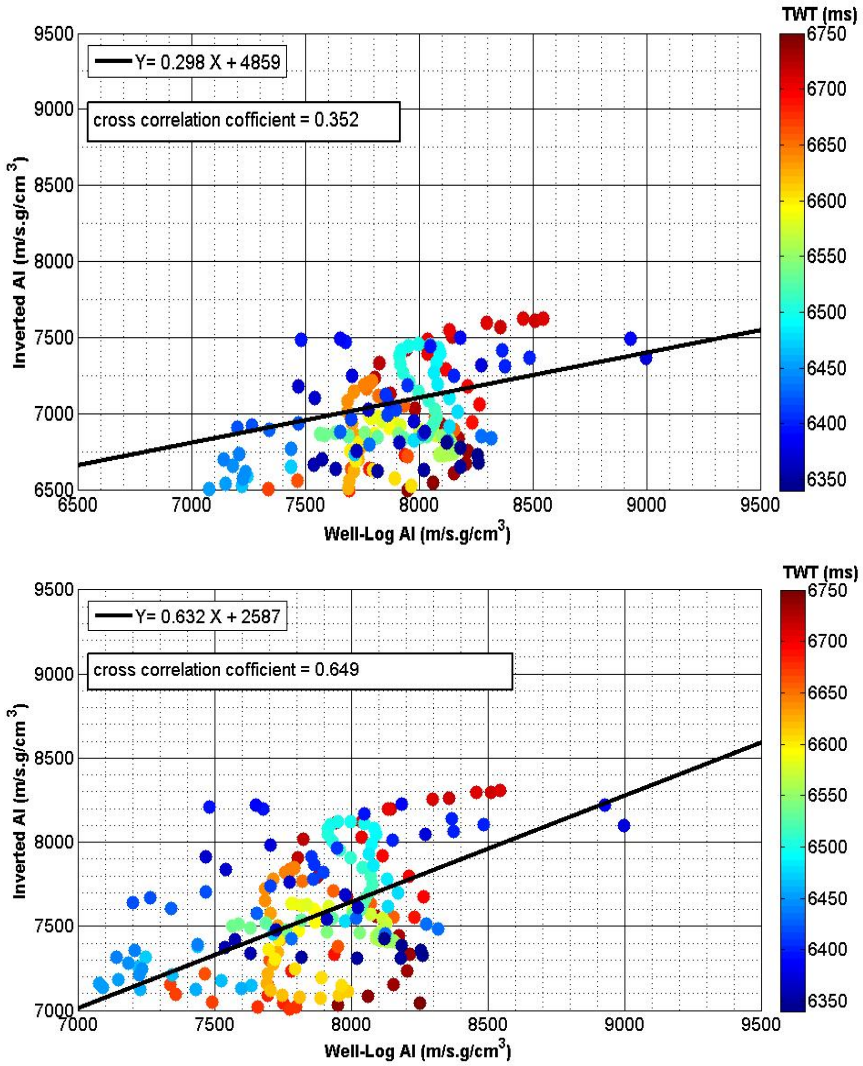

Figure 3. Inverted acoustic impedance result based on: 1) background model constrained to Well B only (top) and 2) background model constrained to Well B and BPSM extrapolation in Well A (bottom). The inverted impedances in both plots are compared with the impedances calculated from actual well-log data.

Conclusions

The results of mapping reservoir lithofacies using only one well along with extrapolating the impedances based on BPSM-guided rock physics modeling show minor differences with the reference case where both wells are used. On the other hand, the resulting lithofacies map resulting from the scenario based on Well B only shows significant differences with the base case. The superiority of the extrapolation scenario demonstrate the value added by combining BPSM with statistical rock physics to the QSI workflows in the case of limited well control.

Acknowledgments

The authors thank BP and ExxonMobil for providing the data set used in this study. Funding and participation in this research is made possible through the support of the Stanford Basin and Petroleum System Modeling, Stanford Center for Reservoir Forecasting, and Stanford Rock Physics industrial affiliate programs and through Saudi Aramco Scholarship. Special thanks to Stew Levin (Stanford Exploration Project) for guidance in setting up the project. Schlumberger graciously provided PetroMod® software. CGG Geosoftware provided the license for Hampson Russell®. Halliburton provided the license to Decision Space Desktop®.

References

Al-Hajeri, M. M., Al Saeed, M., Derks, J., Fuchs, T., Hantschel, T., Kauerauf, A., and Welte, D., 2009, Basin and petroleum system modeling: Oilfield Review, 21(2), p. 14-29.

Avseth, P., Mukerji, T., & Mavko, G., 2005, Quantitative Seismic Interpretation: Cambridge University Press, Cambridge, UK, 376 p.

Connolly, P., 1999, Elastic impedance: The Leading Edge, 18, p. 438–452.

Hantschel, T., A. Kauerauf, 2009, Fundamentals of basin modeling: Berlin, Springer-Verlag, 425 p.

Mukerji, T., Jorstd, A., Avseth, P., 2001, Mapping lithofacies and pore-fluid probabilities in a North Sea Reservoir: Seismic inversions and statistical rock physics: Geophysics, 66(4), p. 988-1001.

Peters, K. E., 2009, Getting Started in Basin and Petroleum System Modeling: American Association of Petroleum Geologists (AAPG) CD-ROM #16, AAPG Datapages.

Wang, Z., Wang, H., and Cates, M. E., 2001, Effective elastic properties of solid clays: Geophysics, 66(2), p. 428-440.

BASIN AND PETROLEUM SYSTEM MODELING OF TERREBONNE BASIN GAS HYDRATES, NORTHERN GULF OF MEXICO

Laura Dafov*, Allegra Hosford Scheirer, Stephan A. Graham, and Tim McHargue
Department of Geological Sciences, Stanford University, Stanford, CA
*ldafov@stanford.edu

Abstract

Gas hydrates affect a wide range of scientific interests including potential future energy resource, drilling hazards, global carbon cycling, sequestration and storage, geohazards, and climate change. Although total global estimates of gas hydrate volumes vary, even the most conservative estimates consider methane hydrates to be the world's largest reservoir of fossil fuel with it potentially being at least 3 times larger than all of the world's conventional and unconventional oil, gas, and coal combined[i].

This study focuses on basin-scale modeling of gas hydrates. Though widely used in academy and industry, basin and petroleum system modeling (BPSM) has only recently been used to study gas hydrate systems[ii]. BPSM is ideally suited for gas hydrate modeling due to its sophisticated treatment of subsurface pressure and temperature through time, and its ability to handle short time steps and fine spatial resolutions. Therefore, BPSM can capture the temporal and spatial variability in gas hydrate deposits as well as changing conditions in the water column that can affect the gas hydrate stability zone (GHSZ).

The Bureau of Ocean Energy Management estimates 607 trillion cubic meters (21,444 trillion cubic feet) of gas hydrates in place in the Gulf of Mexico (GoM) alone[iv]. This research project focuses on the Terrebonne Basin in the northern GoM continental slope, a ponded salt-withdrawal mini-basin in northwest Walker Ridge Area (**Figure 1**). Well data and 2D seismic surveys (**Figures 1 & 2**) underpin the geologic conditions for our 1D, 2D, and a forthcoming 3D Earth model of the basin. The 2009 GoM Gas Hydrates Joint-Industry-Project Leg II logging-while-drilling program confirmed predictions of gas hydrate in the Terrebonne Basin and provides much necessary background information[vi,vii,viii,ix].

We interpreted seven of forty-two high-resolution USGS 2D seismic lines (**Figure 3**), yielding three models for the depositional environment of hydrate-bearing sand intervals. Deeper hydrate-bearing sand reservoirs were deposited as sheet-like turbidite lobes. Two shallower hydrate-bearing intervals display two possible depositional systems: 1) sandy to muddy channel sealed laterally by muddy levees with associated sandy crevasse splays, and 2) ponded sandy lobes cut by channels filled with sand lags and mud (**Figure 4**). Additional observations in the 2D seismic include mass transport deposits and possible contourites.

The mini-basin is bound laterally and floored by Louann Salt, deposited in the Late Triassic-Early Jurassic during rifting of the GoM basin. Our seismic interpretations also indicate periodic salt uplift. Salt movement facilitated mini-basin formation, which was then ponded by sediment and followed by episodes of fill-and-spill and erosion. Overturn of salt along the northwestern edge of the basin resulted in thrust faults. The faults and erosional surfaces act as seals to reservoirs. The greatest volume of sandy reservoir rock

potential occurs in sheet-like turbidite lobes with high lateral continuity, which facilitates updip migration of deep-sourced thermogenic gas along bedding surfaces. Channel levees serve as lateral seals to gas hydrate reservoirs, whereas faults, erosional surfaces, and shales provide vertical seals. Deposition of reservoir-quality sand beds, sealed by shale, occurred most rapidly during the Miocene and continued periodically to the present.

We constructed 1D and pseudo-2D models of the Terrebonne Basin centered on the deepest well, WR313#001. Significant detail was included in the shallow region of most importance for gas hydrate studies (**Figure 5**). We also included model layers for the Oligocene, the Jurassic Louann salt, and the Tithonian source rock. The model was calibrated to observed pore pressure from mud weight (**Figure 6**). Predicted and observed[vi] thickness of the GHSZ are in agreement (**Figure 7**). The GHSZ thickness and existence diminished during the Jurassic most likely due to high basal heat flow during rifting (**Figure 8**).

Development of a 3D model of gas hydrates in the Terrebonne Basin of the northern GoM will provide a vehicle within which to integrate other research being conducted on gas hydrates. In conclusion, BPSM has been called the 'great integrator' in petroleum exploration[v]. The 3D BPSM Earth model will ultimately serve as a platform within which past, present, and future lab and production test findings can be incorporated.

Figures

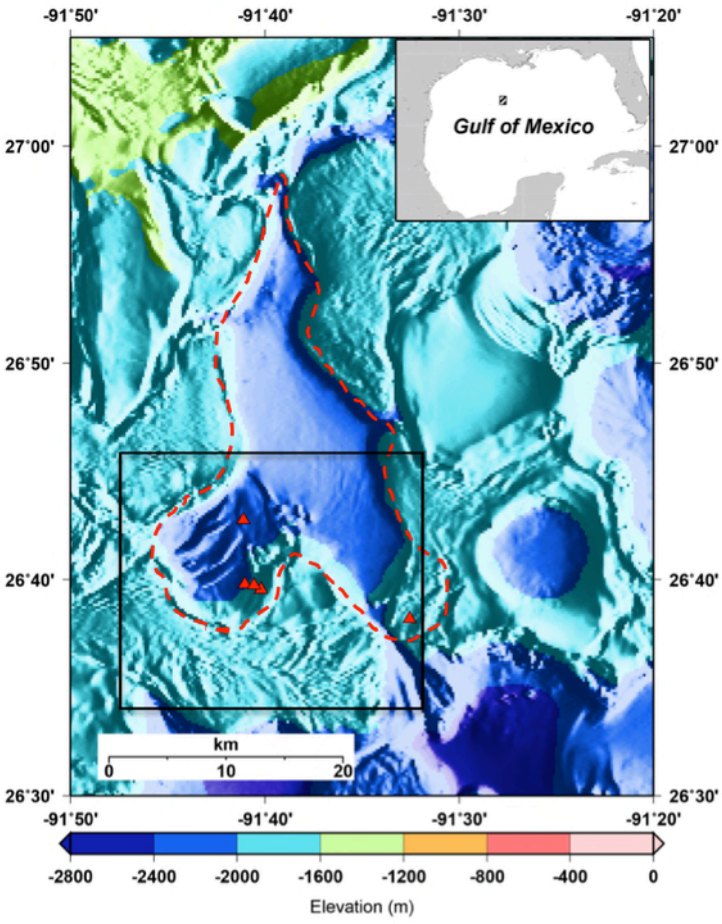

Figure 1. Bathymetric map of study area. Dashed red line indicates the outline of the Terrebonne Basin. Five red triangles indicate well locations. Seafloor bathymetry is from BOEM (https://www.boem.gov/Gulf-of-Mexico-Deepwater-Bathymetry/).

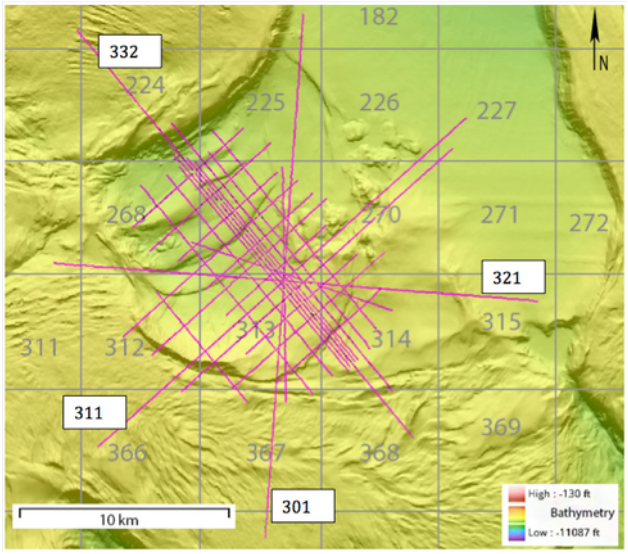

Figure 2. Map showing location of USGS 2D seismic lines (pink). Block numbers are shown in gray. Four white boxes indicate the lines used for interpretation of stratigraphic architecture. See **Figure 1** for bounding box of this area with respect to entire Terrebonne Basin area.

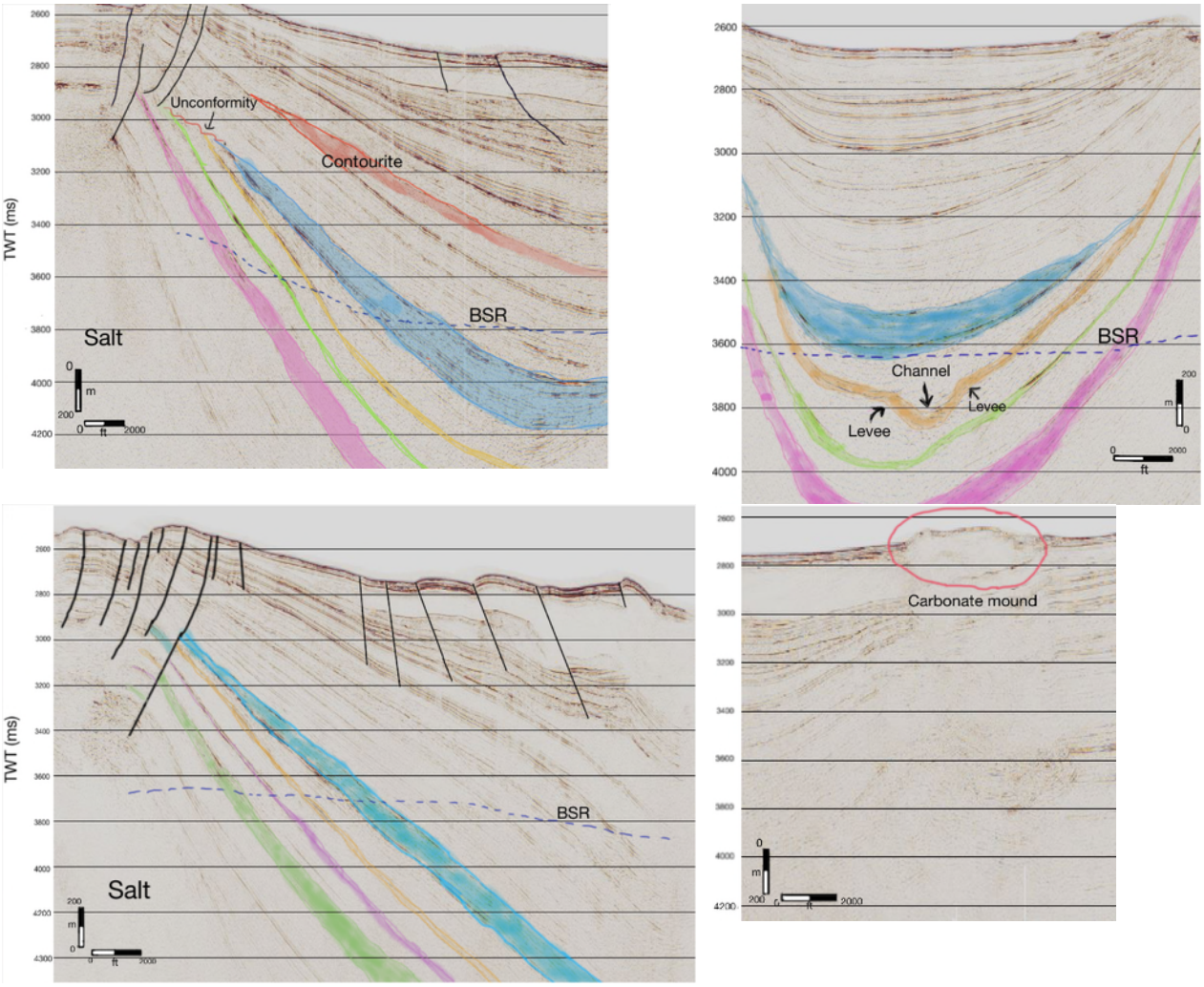

Figure 3. Four interpreted seismic lines (see **Figure 2** for location of lines). Blue, orange, green, and pink horizons are hydrate bearing, based on literature[vi] and well data.

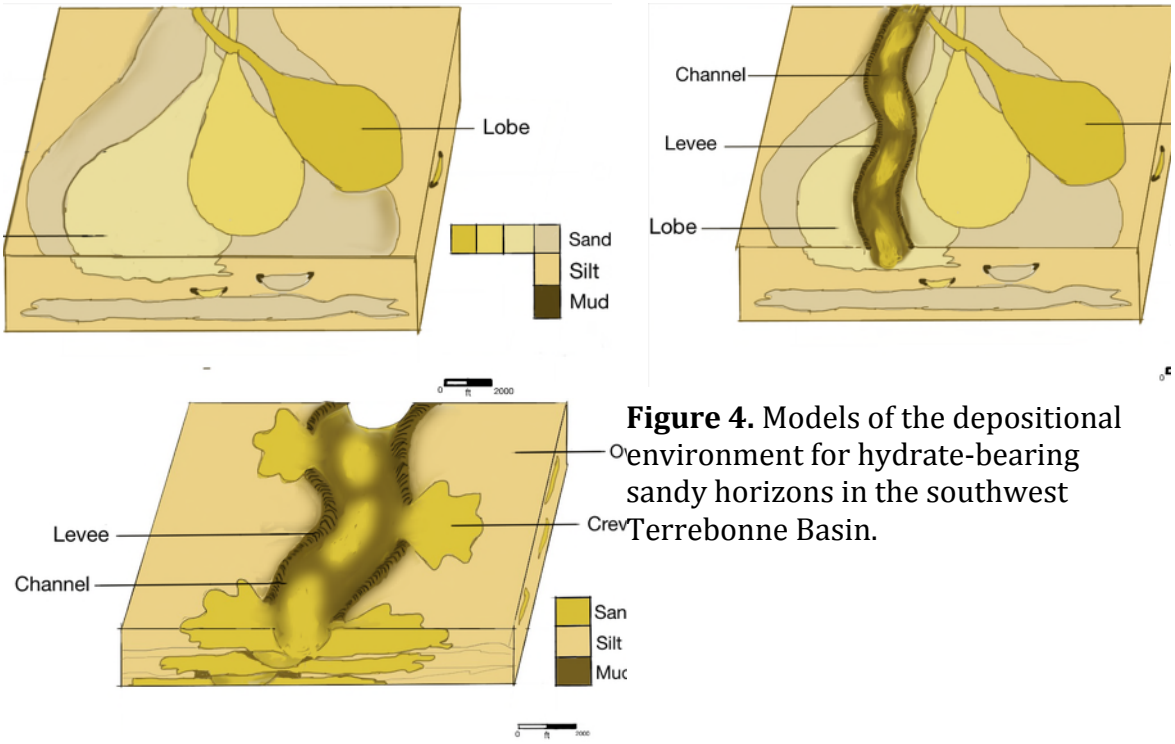

Figure 4. Models of the depositional environment for hydrate-bearing sandy horizons in the southwest Terrebonne Basin.

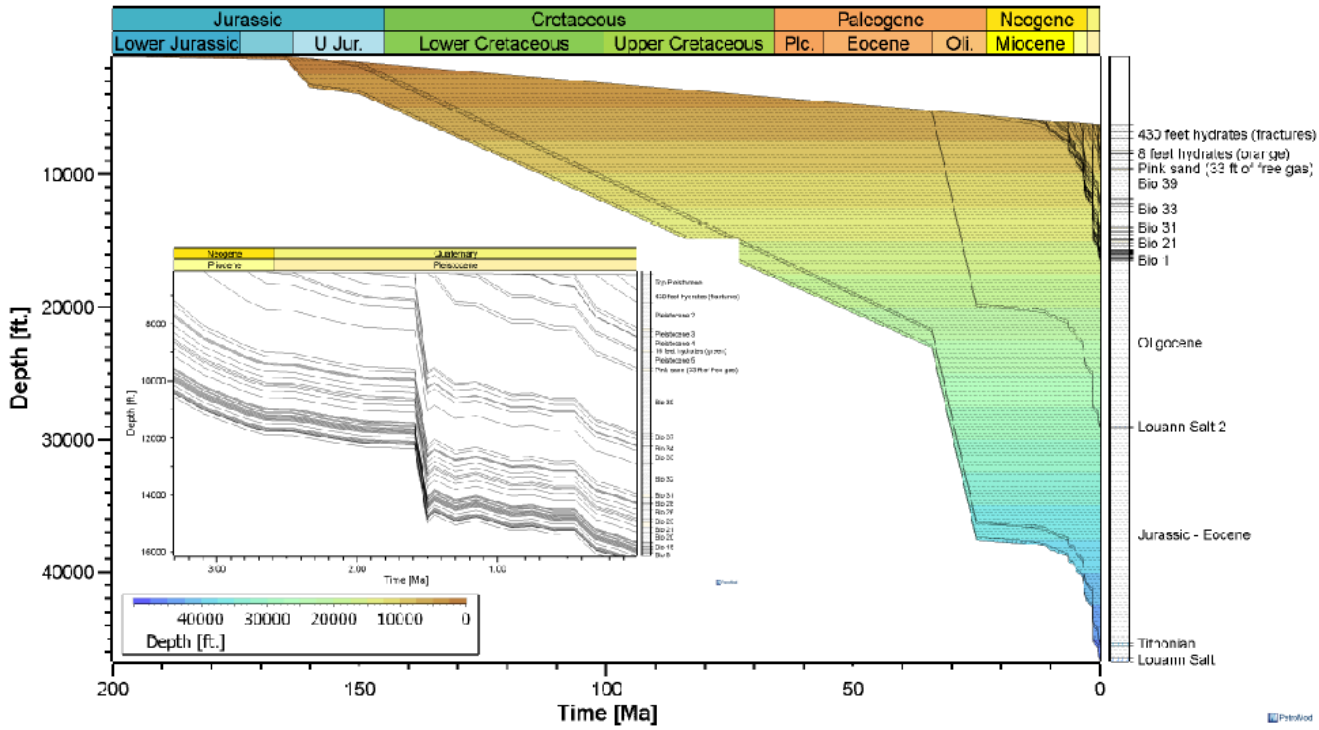

Figure 5. Burial history of sediments in the Walker Ridge area, Gulf of Mexico based on model input for Terrebonne Basin at well WR313#001.

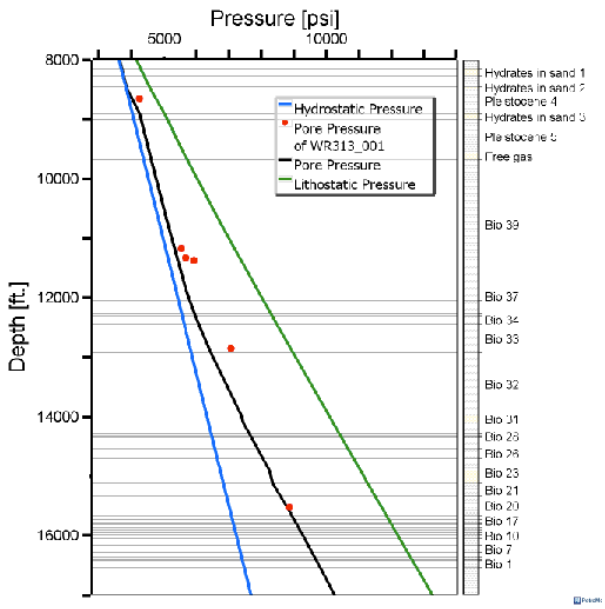

Figure 6. Calibration of predicted pore pressure (black line) to proxy for observed pore pressure, mud weight (filled red circles).

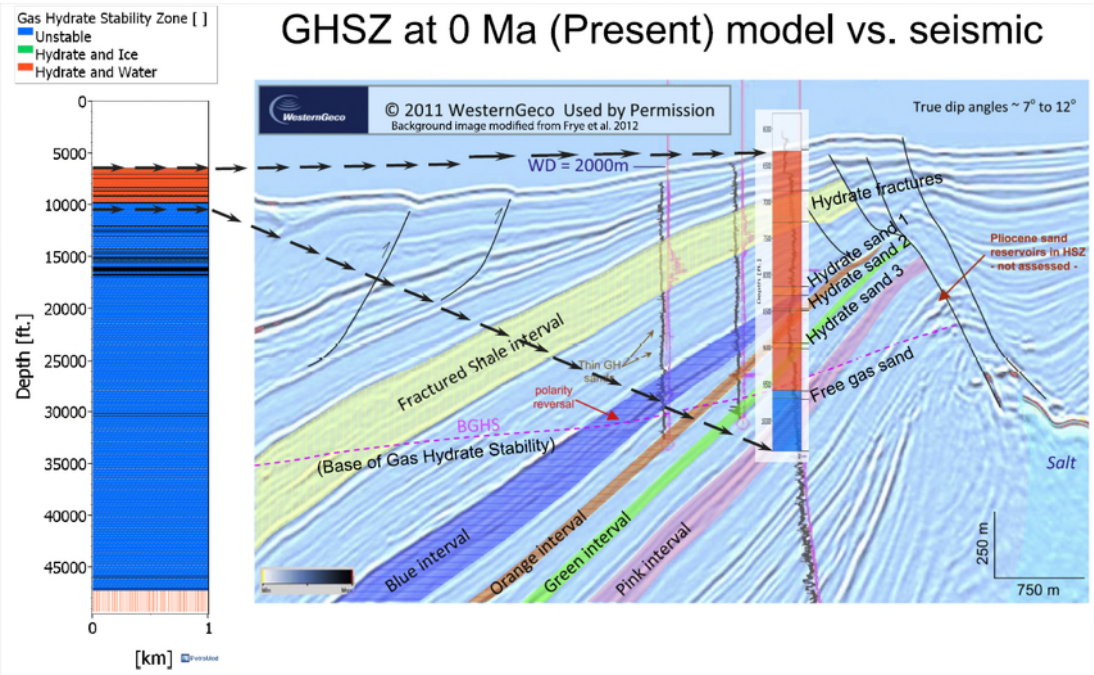

Figure 7. Predicted (this model) and observed[vi] thickness of the GHSZ align well.

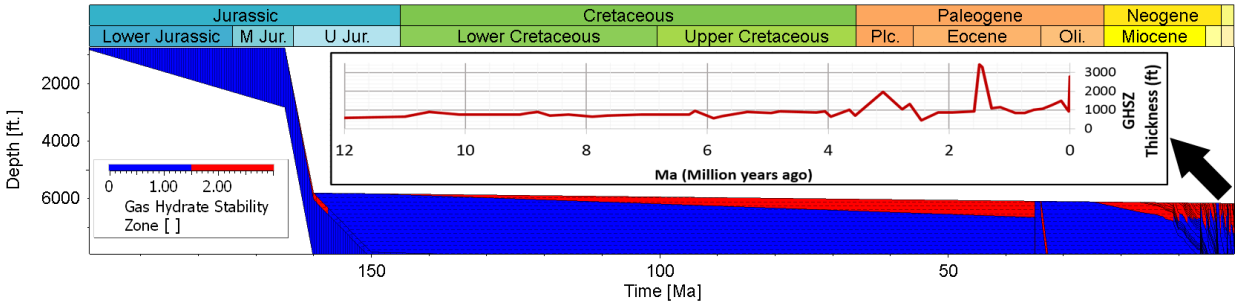

Figure 8. Thickness of the GHSZ through time.

Acknowledgments
We gratefully acknowledge the Department of Energy National Energy Technology Laboratory (NETL) for supporting this research, Matt Frye (BOEM), Seth Haines (USGS), Schlumberger for PetroMod software, Midland Valley for Move software, and Lexco for the Offshore Well and Lease Databases.

References

[i]Wygrala, B., R. Wolf, and T. Fuchs, 2016, Modeling Gas Hydrates in Petroleum Systems, Schlumberger, PetroMod White Paper, p. 23

[ii]Burwicz, E., et al., 2017, 3-D basin-scale reconstruction of natural gas hydrate system of the Green Canyon, Gulf of Mexico, AGU Publications- Geochem. Geophys. Geosyst., 18, 1959–1985

[iv]Boswell, R., T.S. Collett, M. Frye, W. Shedd, D.R. McConnell, and D. Shelander, 2012, Subsurface gas hydrates in the northern Gulf of Mexico, Marine and Petroleum Geology, v. 34, p. 4-30.

[v]Hosford Scheirer, A., 2014, The 'great integrator' in petroleum exploration, Hart's Exploration and Production Magazine, 3 p. [http://www.epmag.com/great-integrator-petroleum-exploration-758546#p=full]

[vi]Frye, M., Shedd, W., Boswell, R., 2012, Gas hydrate resource potential in the Terrebonne Basin, Northern Gulf of Mexico, Marine and Petroleum Geology, v. 34, p. 150-168.

[vii]Boswell, R., M. Frye, D. Shelander, W. Shedd, D.R. McConnell, and A. Cook, 2011, Architecture of gas-hydrate-bearing sands from Walker Ridge 313, Green Canyon 955, and Alaminos Canyon 21: Northern deepwater Gulf of Mexico, v. 34, p. 1-16.

[viii]Boswell, R., T.S. Collett, M. Frye, W. Shedd, D.R. McConnell, and D. Shelander, 2012, Subsurface gas hydrates in the northern Gulf of Mexico, Marine and Petroleum Geology, v. 34, p. 4-30.

[ix]Myshakin, E.M., M. Gaddipati, K. Rose, and B.J. Anderson, 2011, Numerical simulations of depressurization-induced gas production from gas hydrate reservoirs at the Walker Ridge 313 site, northern Gulf of Mexico, Marine and Petroleum Geology, v. 34, p. 169-185.

INTEGRATING STRUCTURAL RESTORATION INTO BASIN AND PETROLEUM SYSTEM MODELING: A CASE STUDY FROM THE MISSISSIPPI CANYON AREA IN THE GULF OF MEXICO

Wisam H. AlKawai[1,*], Kristian Meisling[1], Tapan Mukerji[2] and Allegra Hosford Scheirer[1]
[1]Department of Geological Sciences, Stanford University, Stanford, CA
[2]Department of Energy Resources Engineering, Stanford University, Stanford, CA
*walkawai@stanford.edu

Summary

In this study, we investigate the relative importance of incorporating full structural restorations into basin and petroleum system modeling. The emphasis here is on complex structures involving faults, and how incorporating changes in thickness and juxtaposition of stratigraphic units due to slip on faults can impact pressure and thermal history modeling. We use a 2D arbitrary seismic line extracted from a 3D seismic volume that crosses an expulsion rollover in Thunder Horse mini-basin in the Mississippi Canyon area, Gulf of Mexico. We apply 2D sequential structural restorations techniques to understand the evolution of the expulsion rollover. Results of the sequential structural restoration suggest that the slip along the fault took place between 12.5 and 9.0 Ma in response to salt withdrawal triggered by high sedimentation rates during middle Miocene. The layers in the hanging wall of the expulsion rollover displaced laterally by about 2.2 km due to offset along the fault plane. We compare a basin model that calculates layers paleo-thicknesses based on porosity loss (vertical backstripping) with another basin model that conditions layers paleo-thicknesses to the structural restorations. The two models are associated with different paleo-thicknesses of the layers before 12.5 Ma as well as different spatial contacts with salt. The paleo pore pressure values simulated by the two models differ before 12.5 Ma, and the differences increase with fault slip. The paleo temperatures predicted by the two models differ significantly before 12.5 Ma, and these differences decrease until the two models reach the same temperature values at present day. We infer from the results that changes in predicted paleo-thicknesses can change the simulated pore pressure due to changing the overburden pressure and the permeability pathways associated with stratigraphic contacts. Also, the changes in paleo-thicknesses can have implications for thermal history that depends on the changes in stratigraphic contacts, changes in pore pressure history and heat generation in the basin.

Introduction

A widely used method to reconstruct paleo-thickness of the layers in basin and petroleum system modeling (BPSM) is porosity-controlled backstripping (Al-Hajeri et al., 2009; Hantschel and Kauerauf, 2009). A key assumption in this approach is that layer thickness changes through time are solely governed by porosity loss due to mechanical compaction, chemical compaction and cementation. This underlying assumption is violated in areas of complex structures in which layer thickness is modified by slip on faults. A proposed method to work around this issue in structural complex areas is the paleo-stepping technique (Al-Hajeri et al., 2009; Baur et al., 2009; Hantschel and Kauerauf, 2009; Lampe et al., 2012). Paleo-stepping imposes complete geometric models at certain geologic

times to account for structural deformation. These geometric models are typically obtained through sequential structural restoration. Sequential structural restoration reconstructs changes in layer thicknesses through time by combining kinematic restoration algorithms with porosity-controlled backstripping (Bally et al., 1966; Dahlstrom, 1969,1970; Rowan, 1993). The goal of these algorithms is to progressively undeform structurally deformed layers in a model.

One example of a complex structure involving lateral slip on a fault is the extensional structure coupled with salt movement known as "raft tectonics" (Burollet, 1975; Jackson and Cramez, 1989; Jackson and Talbot, 1991; Duval et al., 1992; Lundin,1992; Hudec and Jackson, 2011). Raft tectonics can be defined as gravitational gliding of rigid fault-bounded blocks on a low angle detachment of thin salt. Raft tectonics were first documented in the Kwanza Basin of Angola (Burollet, 1975; Duval et al., 1992; Lundin, 1992). In the Gulf of Mexico, raft tectonics are recognized in the northwestern onshore region by Fiduk et al. (2004) and in the northeastern offshore region including the Mississippi Canyon protraction area by Pilcher et al. (2014). Studies of raft tectonics based on structural restoration (Duval et al., 1992; Rouby et al., 2003; Hudec and Jackson, 2004) or physical models in the laboratory (Cobbold and Szatmari, 1991; Vendeville and Jackson, 1992; Fort et al., 2004) suggest that raft tectonics begins with an expulsion rollover and progresses into rafting with increased extension. An expulsion rollover is a structure formed in response to movement on a thin-skinned listric normal fault that soles into a salt decollement. In this paper, we focus on a 2D seismic line crossing an expulsion rollover in the Thunder Horse mini-basin in the Mississippi Canyon area, Gulf of Mexico. Our goal is to model the evolution in structural geometry of the expulsion rollover and then investigate the implications for pressure and thermal history model predictions when constructing layer paleo-thicknesses in BPSM by both porosity-controlled backstripping and paleo-stepping methods.

Methods

In the first part of the study, we applied structural restoration techniques to investigate the structural evolution of the expulsion rollover along the path of the arbitrary 2D seismic line. We performed structural restoration in Move 2D for each horizon, sequentially back in time. For each horizon, the workflow implemented in Move 2D combines: (1) porosity-controlled backstripping, (2) isostatic adjustment, (3) restoration of the horizons geometry for displacement along the fault, and (4) adjustment of the horizons to a regional elevation. Regional elevation is defined as the bathymetric profile and elevation of the bedding surface before deformation (Marshak and Woodward, 1988). Adjustment to a regional elevation in the 2D restoration allows us to account for the changing cross sectional area of salt through time due to three-dimensional flow of salt (Rowan, 1993).

In the next part of the study, we constructed two 2D basin modeling scenarios in PetroMod. The first scenario, Model I, takes an input of salt thickness changes and determines layer paleo-thicknesses by porosity-controlled backstripping. The salt thickness changes in this model are obtained by comparing each horizon to an assumed regional elevation following the approach discussed by Gibson (2012). The second scenario, Model II, is based on paleo-stepping method such that both the paleo-thicknesses of the salt and the geometry of other stratigraphic layers are imposed from the sequential structural restorations. We assumed the same boundary conditions and physical properties for the

layers in both models. After constructing the models, we compared the resulting pore pressure and temperature predictions to highlight any key differences and understand the causes of these differences. In both models, we assumed poro-elastic behavior of the sediments. The models did not address poro-plastic effects. Hantschel et al. (2011) and Nikolinakou et al. (2012) pointed out that poro-plastic effects may have potential significance in prediction of pore pressure in areas such as fold and thrust belts and the vicinity of salt domes.

Results

The resulting 99.0 Ma restoration in Figure 1e suggests pre-existing spatial variations in the depositional thickness of salt. Differential thickness created bathymetric relief that concentrated sediment accumulation in areas of lesser salt thickness. Differential sediment accumulation resulted in salt movement, which inflated the salt thickness in the area between Mensa and Thunder Horse mini-basins (i.e., passive diapirism) as can be seen on the 24.0 Ma restoration in Figure 1d. Diapirism was followed by the burial of the diapir during an episode of high sedimentation rate in middle Miocene time (Figure 1b-c). Burial of the diapir led to salt withdrawal, collapse of the diapir and gravitational gliding of the stratigraphic layers along the listric fault between 12.5 Ma to 9 Ma. This restoration model is similar to the early phase of rafting documented in Kwanza Basin by Duval et al. (1992) and in offshore Congo by Rouby et al. (2003). The layers on the hanging wall of the listric fault translate basinward by about 2.2 km between 12.5 and 9.0 Ma (Figure 1b).

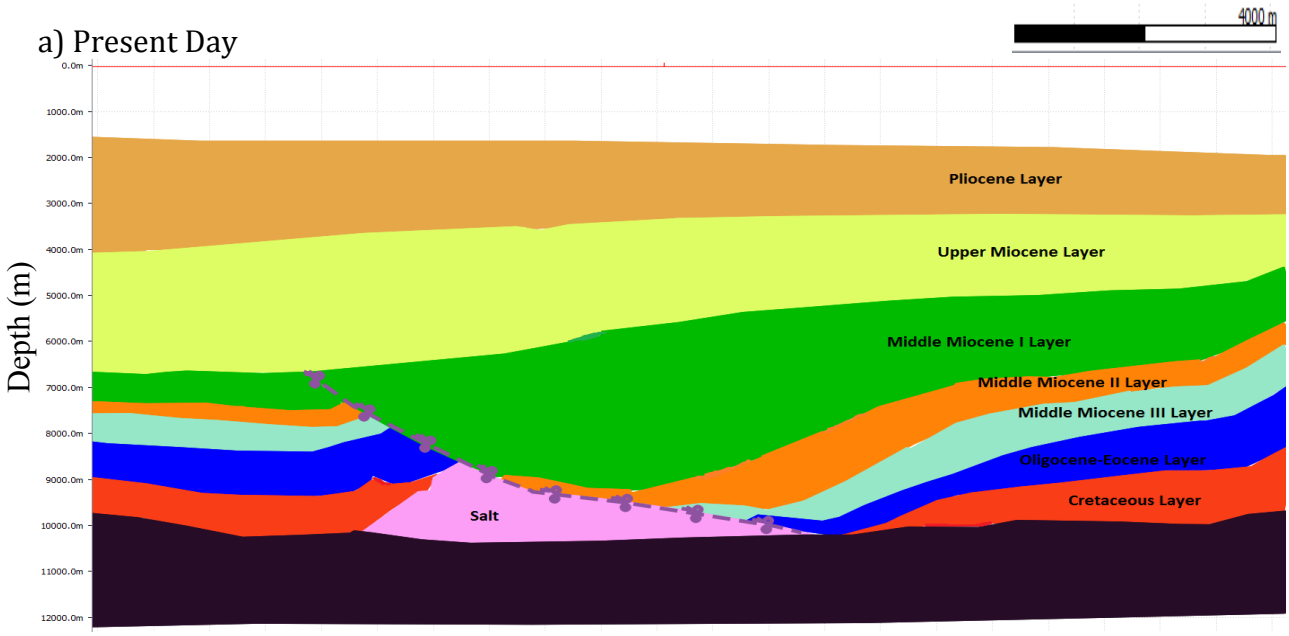

b) 9.0 Ma

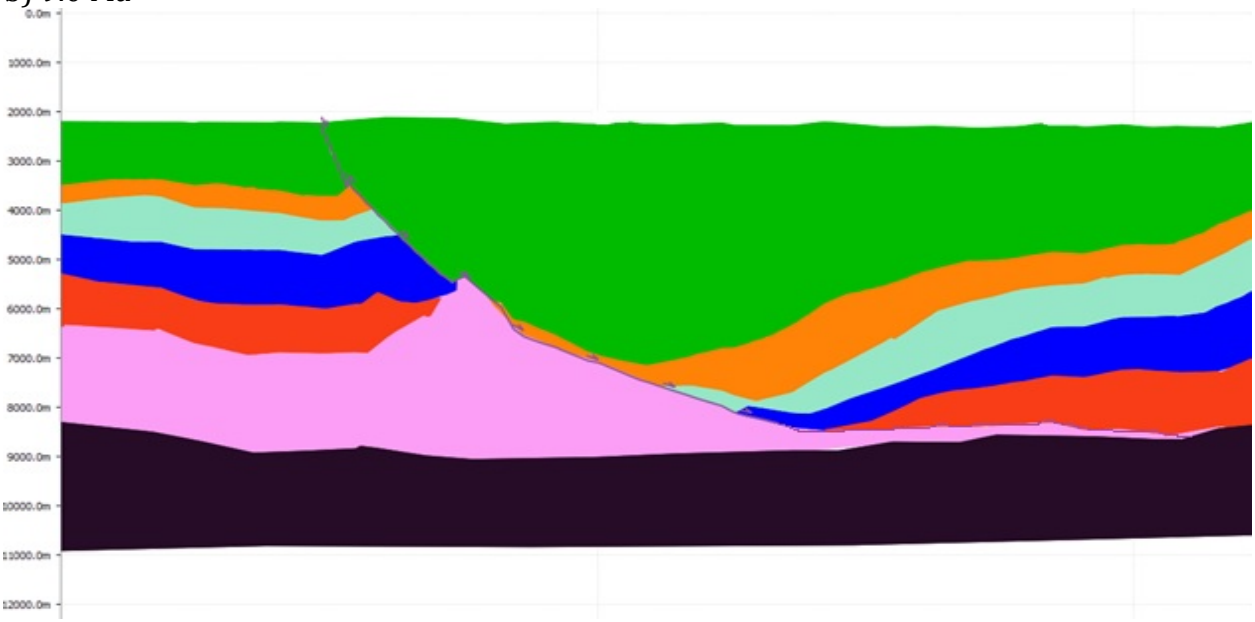

c) 12.5 Ma

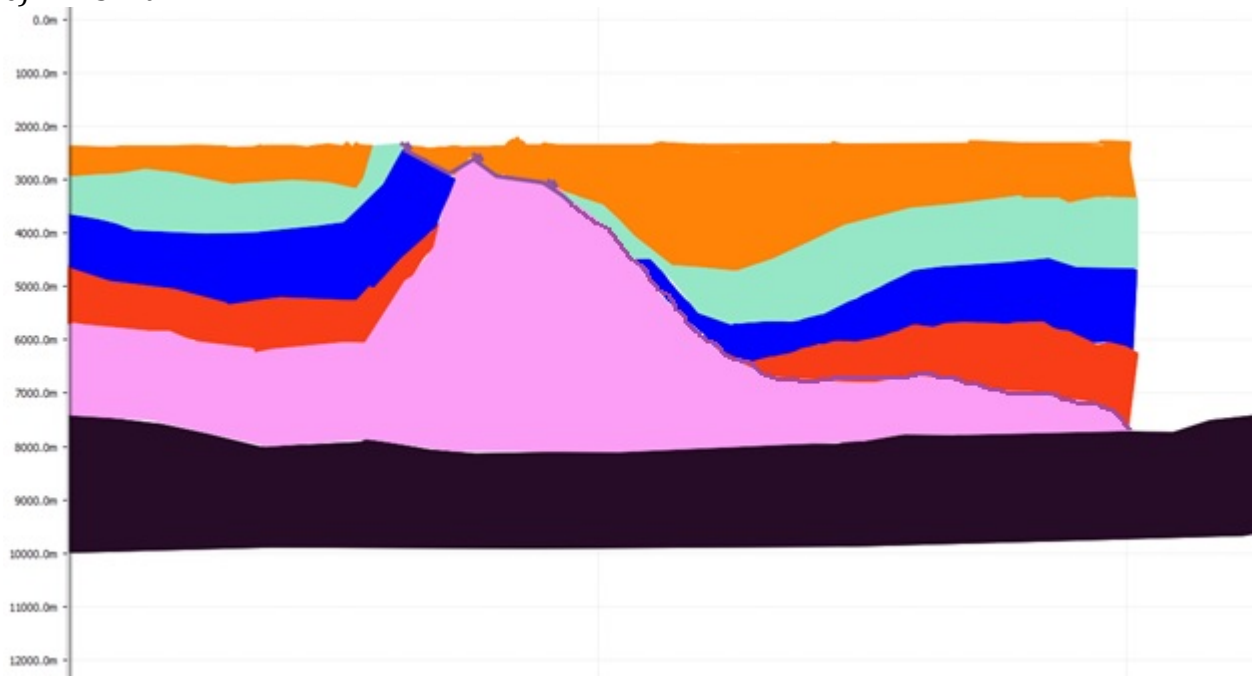

d) 24.0 Ma

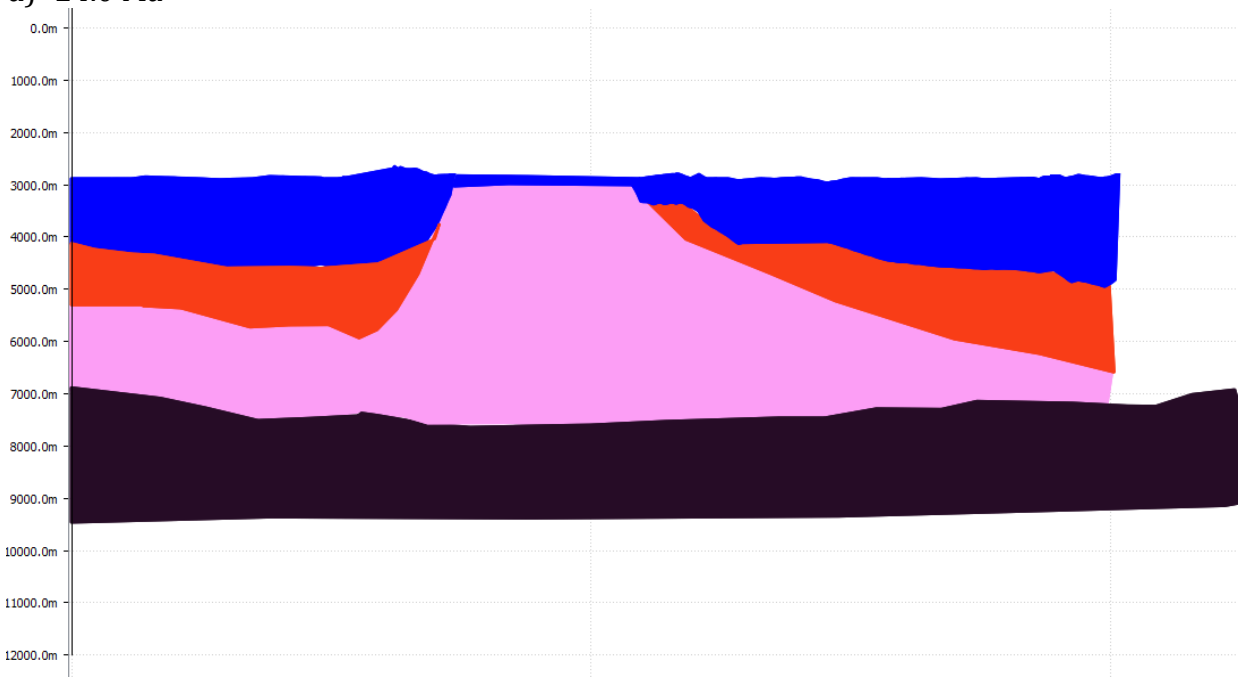

e) 99.0 Ma

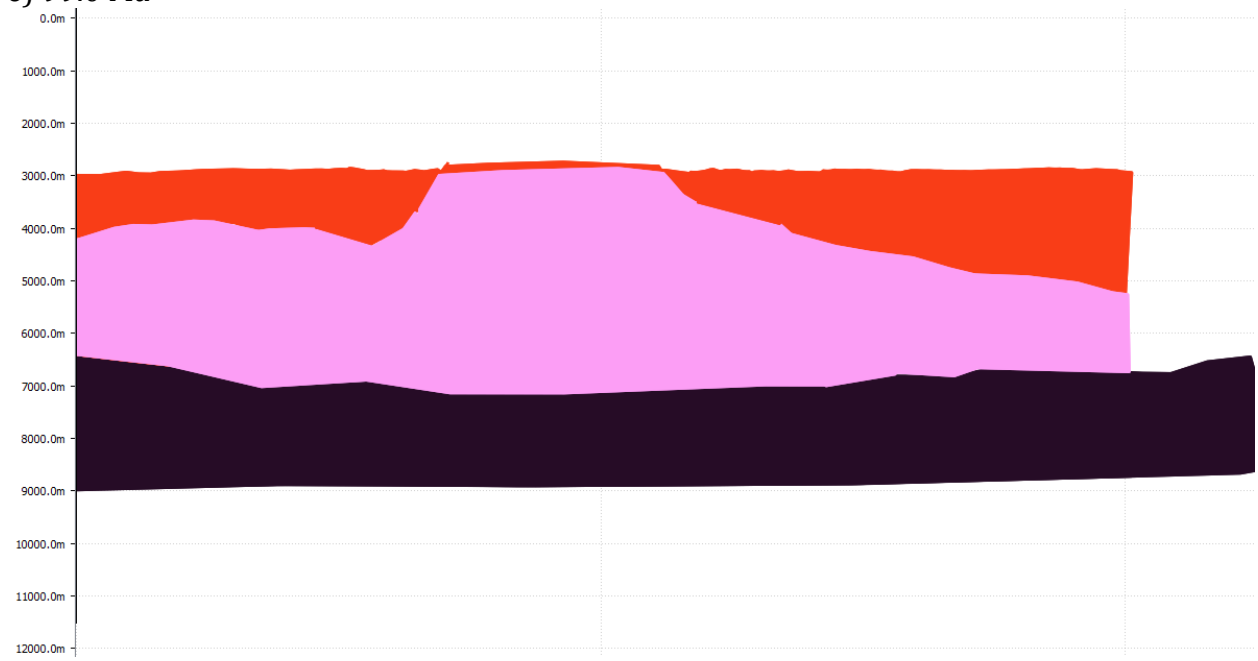

Figure 1. Result of sequential structural restoration illustrating the evolution of the raft system that started as a diapir in (d) and failed due to high Miocene sedimentation (b-c).

For deeper (older) stratigraphic layers in the hanging wall of the rollover, Model II predicts higher pore pressure values than Model I. On the other hand, present day temperature values are nearly identical for both models. To investigate pore pressure and temperature differences due to different layer paleo-thicknesses in the two models, we plotted the pore pressure and temperature outputs at different time steps for the middle Miocene III (24-14 Ma) layer in both models in Figures 2 and 3, respectively. There is higher pore pressure buildup in Model II than Model I at 12.5 Ma (Figure 2), which can be

explained by the higher overburden experienced by the layers and the greater spatial extent of contact with salt. This pressure buildup persists to present day due to rapid burial of the layer.

The temperature plots of the same layer in Figure 3 start with considerable differences in temperature at 12.5 Ma. However, these differences dissipate over time until the two models reach nearly identical temperatures at present day. The development of higher temperature early in Model II is related to the increased extent of contact with salt, which is characterized by high thermal conductivity. As discussed previously, pore pressure builds up early in Model II was and is enhanced by later episodes of relatively high sedimentation. The higher overpressure of the deep layers in Model II results in higher heat capacity than observed in Model I. When we compare the resulting heat capacities in both models, Model II has higher heat capacity values than Model I because pore pressure preserves porosity and increases pore fluid volume. Therefore, the two models reached the same present day temperatures, despite the difference in the heat capacity between them, ultimately equilibrating with time.

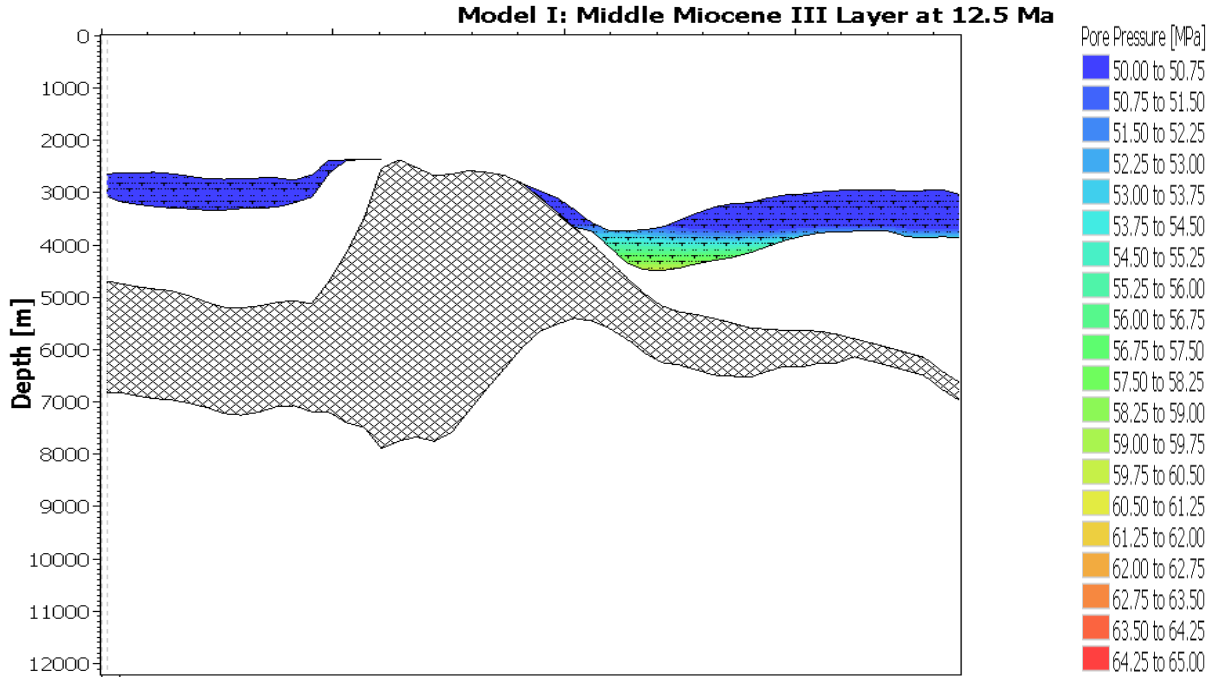

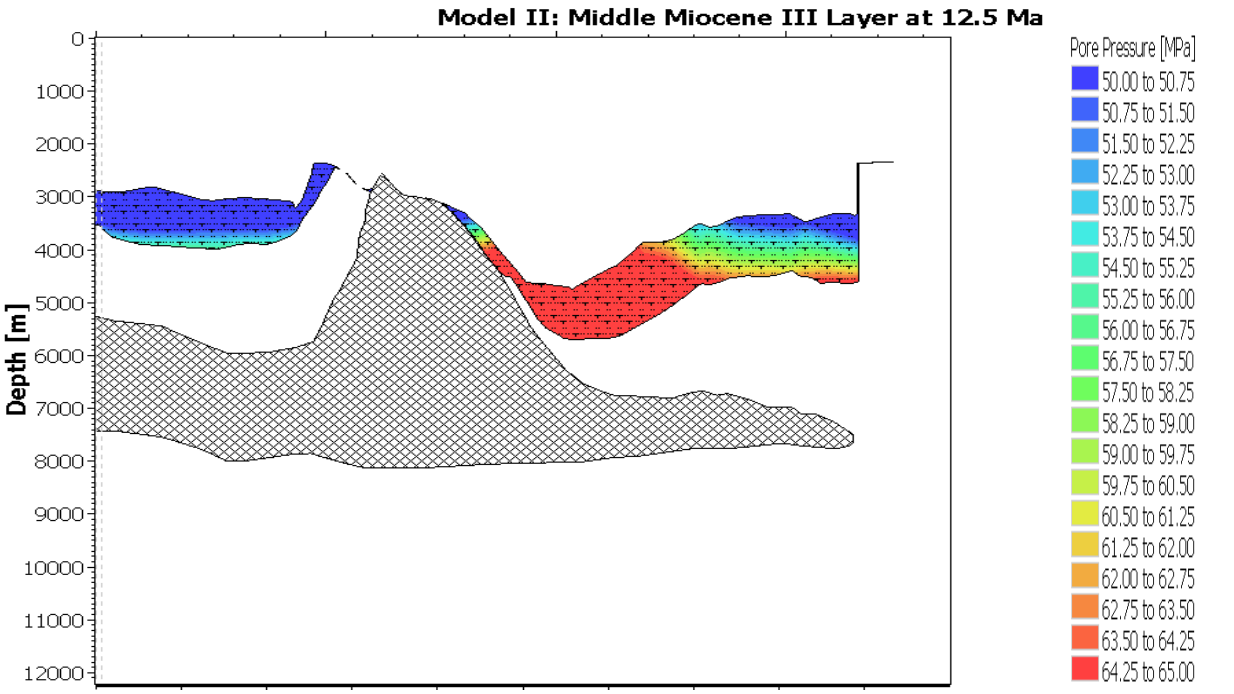
Model II: Middle Miocene III Layer at 12.5 Ma
Depth [m]
0
1000
2000
3000
4000
5000
6000
7000
8000
9000
10000
11000
12000
Pore Pressure [MPa]
50.00 to 50.75
50.75 to 51.50
51.50 to 52.25
52.25 to 53.00
53.00 to 53.75
53.75 to 54.50
54.50 to 55.25
55.25 to 56.00
56.00 to 56.75
56.75 to 57.50
57.50 to 58.25
58.25 to 59.00
59.00 to 59.75
59.75 to 60.50
60.50 to 61.25
61.25 to 62.00
62.00 to 62.75
62.75 to 63.50
63.50 to 64.25
64.25 to 65.00

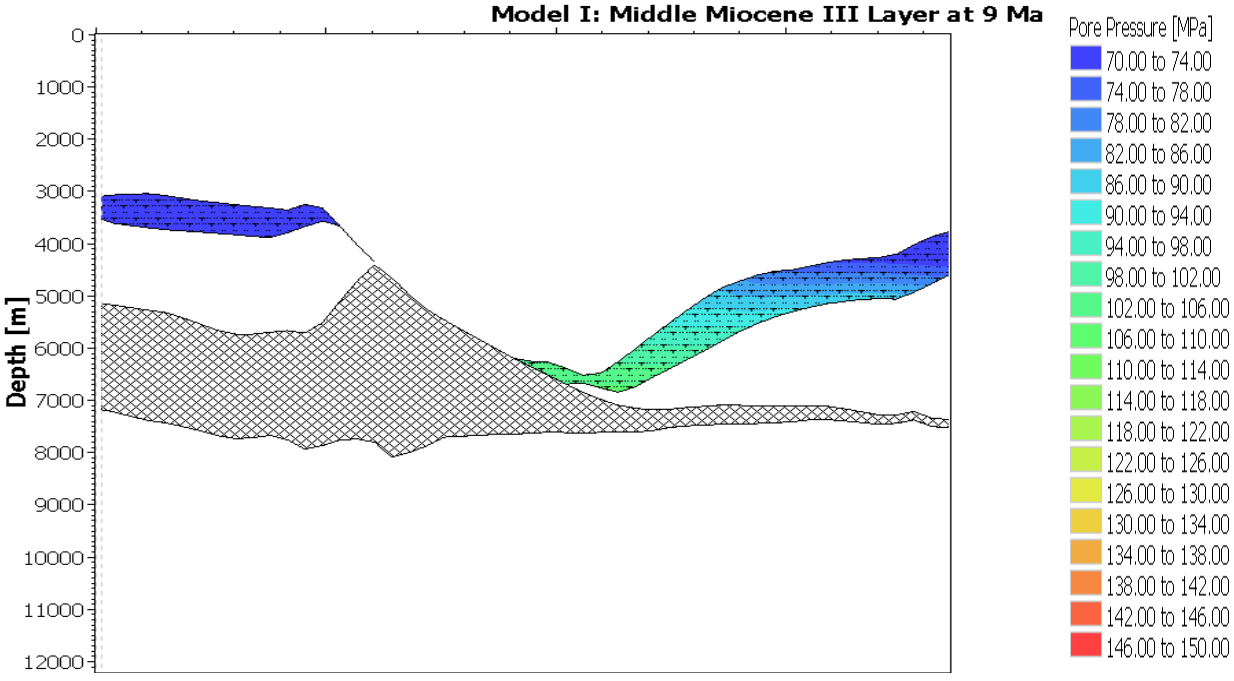
Model I: Middle Miocene III Layer at 9 Ma
Depth [m]
0
1000
2000
3000
4000
5000
6000
7000
8000
9000
10000
11000
12000
Pore Pressure [MPa]
70.00 to 74.00
74.00 to 78.00
78.00 to 82.00
82.00 to 86.00
86.00 to 90.00
90.00 to 94.00
94.00 to 98.00
98.00 to 102.00
102.00 to 106.00
106.00 to 110.00
110.00 to 114.00
114.00 to 118.00
118.00 to 122.00
122.00 to 126.00
126.00 to 130.00
130.00 to 134.00
134.00 to 138.00
138.00 to 142.00
142.00 to 146.00
146.00 to 150.00

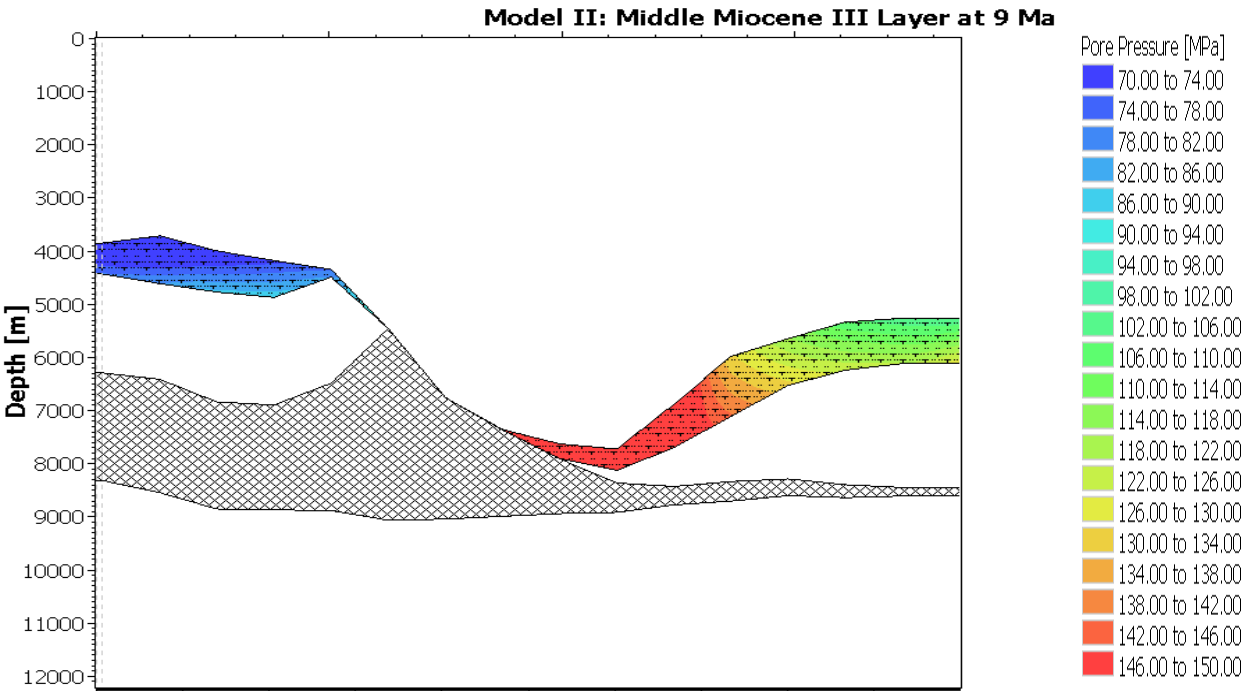
Model II: Middle Miocene III Layer at 9 Ma
Depth [m]
0
1000
2000
3000
4000
5000
6000
7000
8000
9000
10000
11000
12000
Pore Pressure [MPa]
70.00 to 74.00
74.00 to 78.00
78.00 to 82.00
82.00 to 86.00
86.00 to 90.00
90.00 to 94.00
94.00 to 98.00
98.00 to 102.00
102.00 to 106.00
106.00 to 110.00
110.00 to 114.00
114.00 to 118.00
118.00 to 122.00
122.00 to 126.00
126.00 to 130.00
130.00 to 134.00
134.00 to 138.00
138.00 to 142.00
142.00 to 146.00
146.00 to 150.00

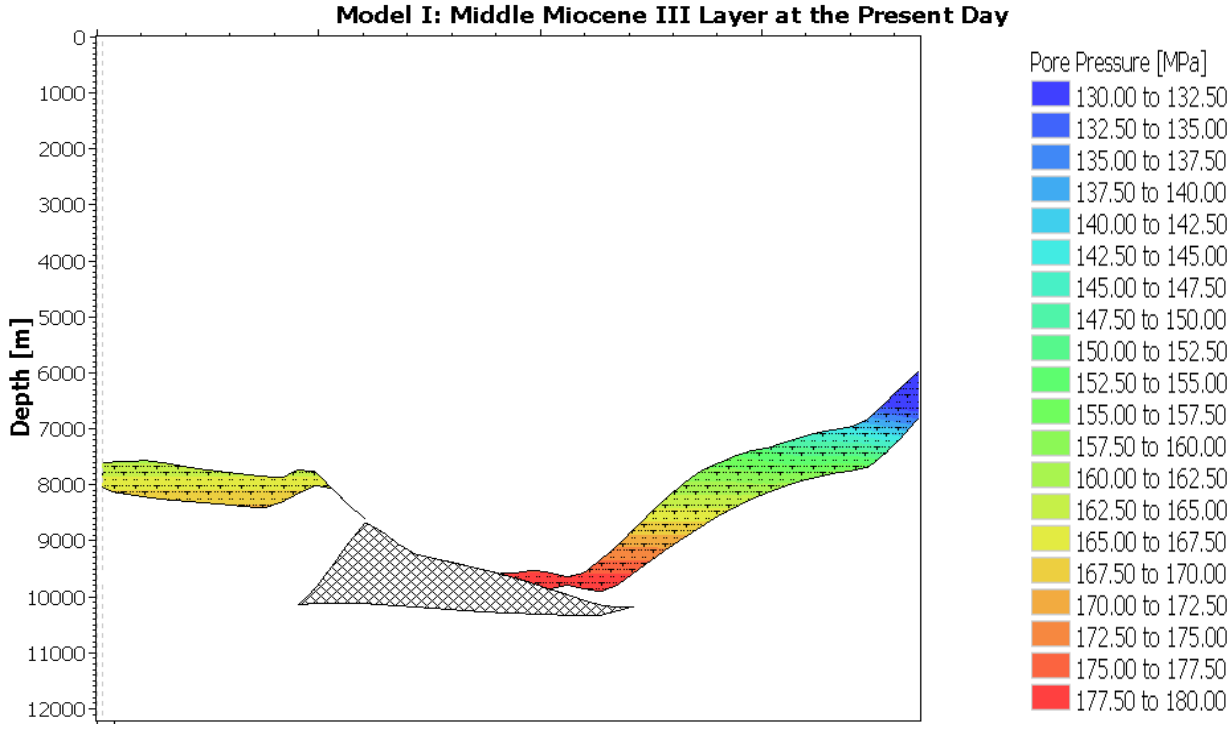
Model I: Middle Miocene III Layer at the Present Day
Depth [m]
0
1000
2000
3000
4000
5000
6000
7000
8000
9000
10000
11000
12000
Pore Pressure [MPa]
130.00 to 132.50
132.50 to 135.00
135.00 to 137.50
137.50 to 140.00
140.00 to 142.50
142.50 to 145.00
145.00 to 147.50
147.50 to 150.00
150.00 to 152.50
152.50 to 155.00
155.00 to 157.50
157.50 to 160.00
160.00 to 162.50
162.50 to 165.00
165.00 to 167.50
167.50 to 170.00
170.00 to 172.50
172.50 to 175.00
175.00 to 177.50
177.50 to 180.00

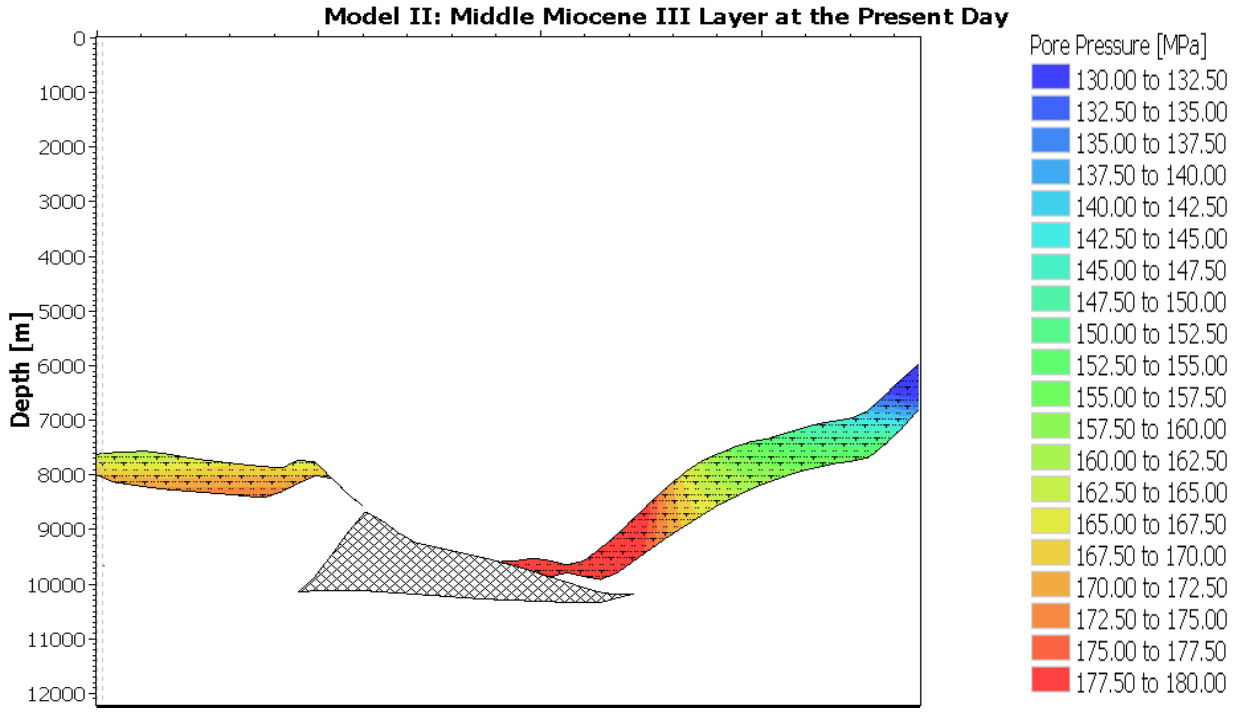

Figure 2. Pore pressure changes at different time steps for Middle Miocene III layer in both models showing a greater degree of pore pressure build up in Model II.

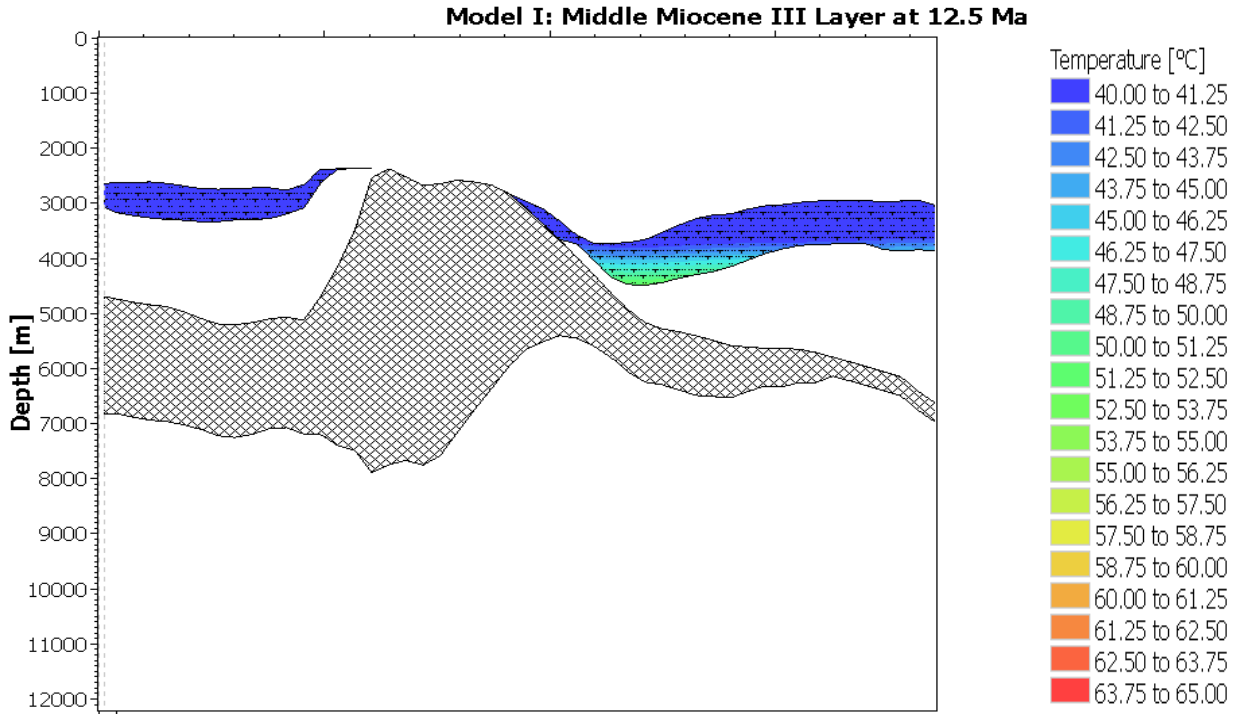

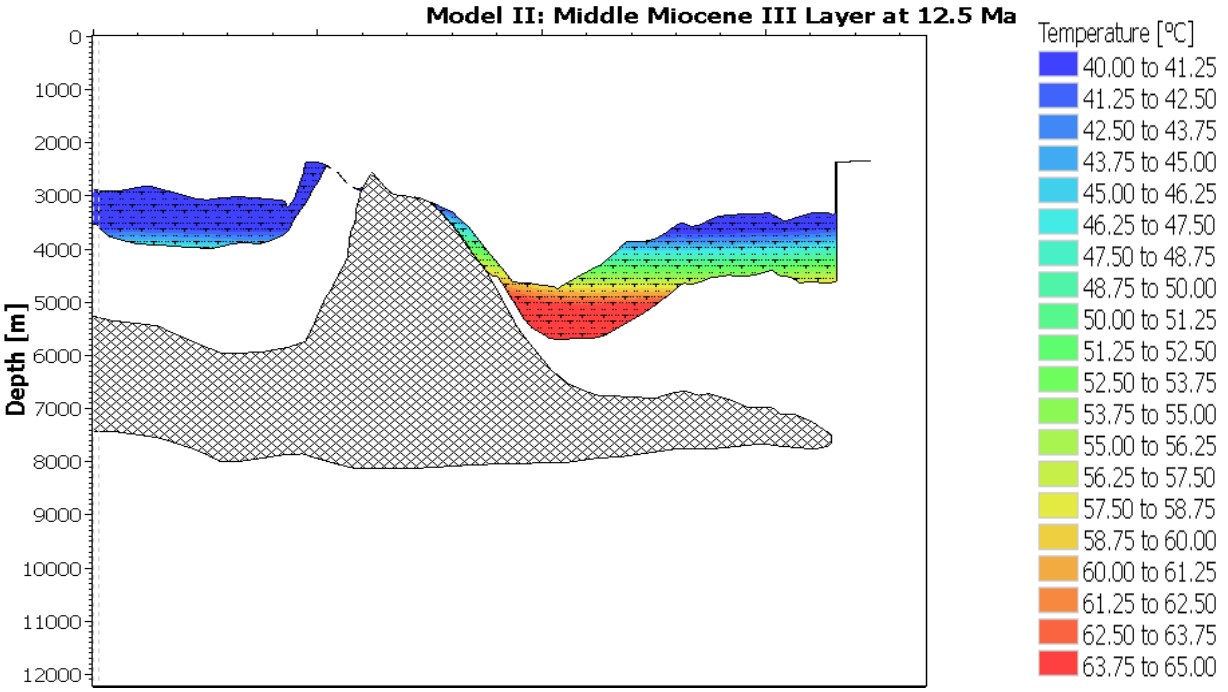
Model II: Middle Miocene III Layer at 12.5 Ma
Depth [m]
0
1000
2000
3000
4000
5000
6000
7000
8000
9000
10000
11000
12000
Temperature [°C]
40.00 to 41.25
41.25 to 42.50
42.50 to 43.75
43.75 to 45.00
45.00 to 46.25
46.25 to 47.50
47.50 to 48.75
48.75 to 50.00
50.00 to 51.25
51.25 to 52.50
52.50 to 53.75
53.75 to 55.00
55.00 to 56.25
56.25 to 57.50
57.50 to 58.75
58.75 to 60.00
60.00 to 61.25
61.25 to 62.50
62.50 to 63.75
63.75 to 65.00

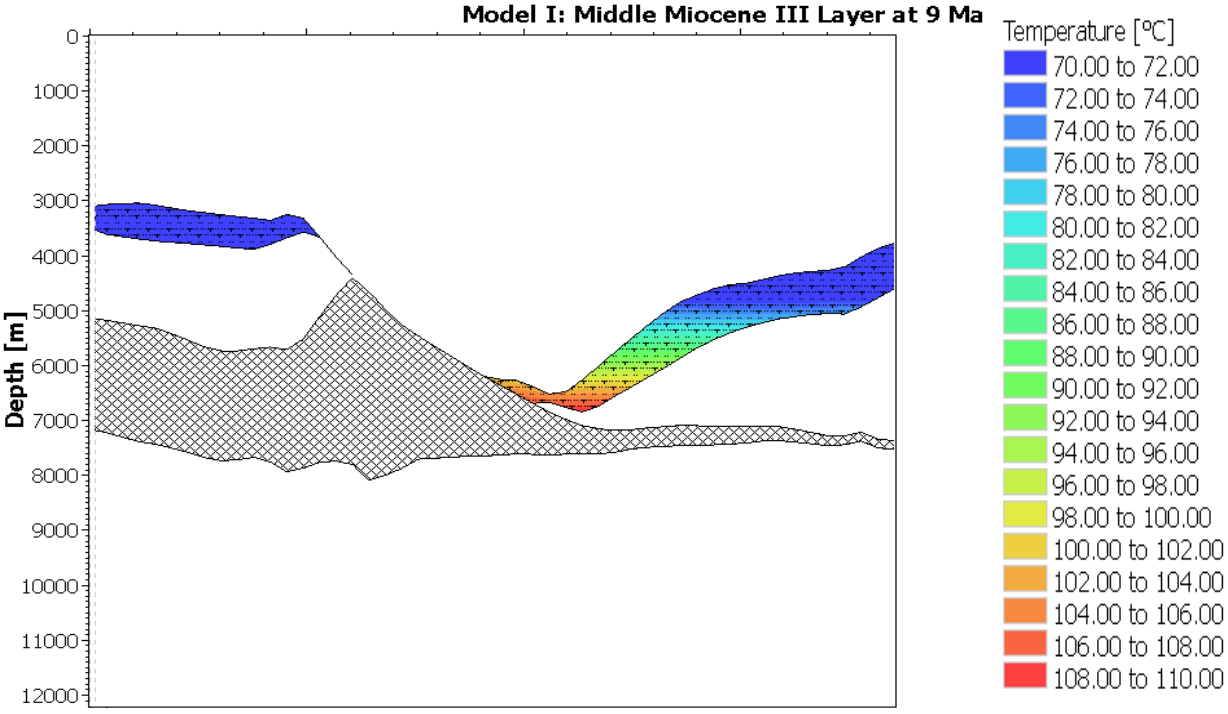
Model I: Middle Miocene III Layer at 9 Ma
Depth [m]
0
1000
2000
3000
4000
5000
6000
7000
8000
9000
10000
11000
12000
Temperature [°C]
70.00 to 72.00
72.00 to 74.00
74.00 to 76.00
76.00 to 78.00
78.00 to 80.00
80.00 to 82.00
82.00 to 84.00
84.00 to 86.00
86.00 to 88.00
88.00 to 90.00
90.00 to 92.00
92.00 to 94.00
94.00 to 96.00
96.00 to 98.00
98.00 to 100.00
100.00 to 102.00
102.00 to 104.00
104.00 to 106.00
106.00 to 108.00
108.00 to 110.00

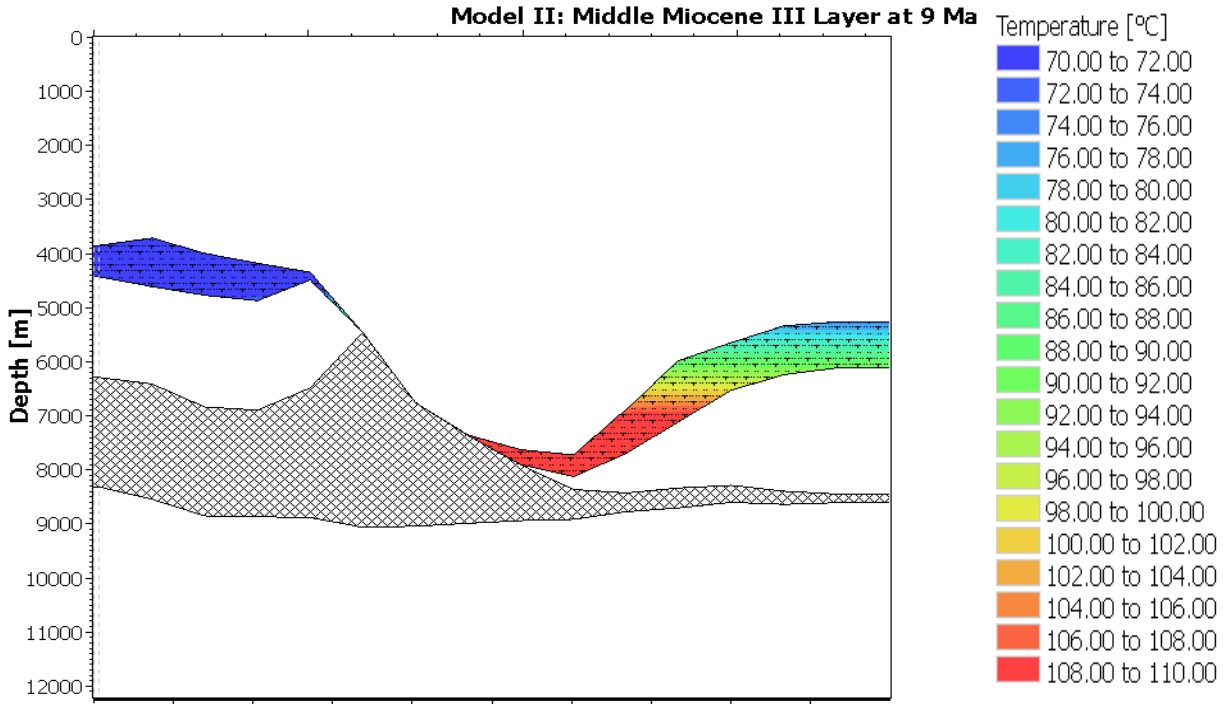
Model II: Middle Miocene III Layer at 9 Ma
Depth [m]
0
1000
2000
3000
4000
5000
6000
7000
8000
9000
10000
11000
12000
Temperature [°C]
70.00 to 72.00
72.00 to 74.00
74.00 to 76.00
76.00 to 78.00
78.00 to 80.00
80.00 to 82.00
82.00 to 84.00
84.00 to 86.00
86.00 to 88.00
88.00 to 90.00
90.00 to 92.00
92.00 to 94.00
94.00 to 96.00
96.00 to 98.00
98.00 to 100.00
100.00 to 102.00
102.00 to 104.00
104.00 to 106.00
106.00 to 108.00
108.00 to 110.00

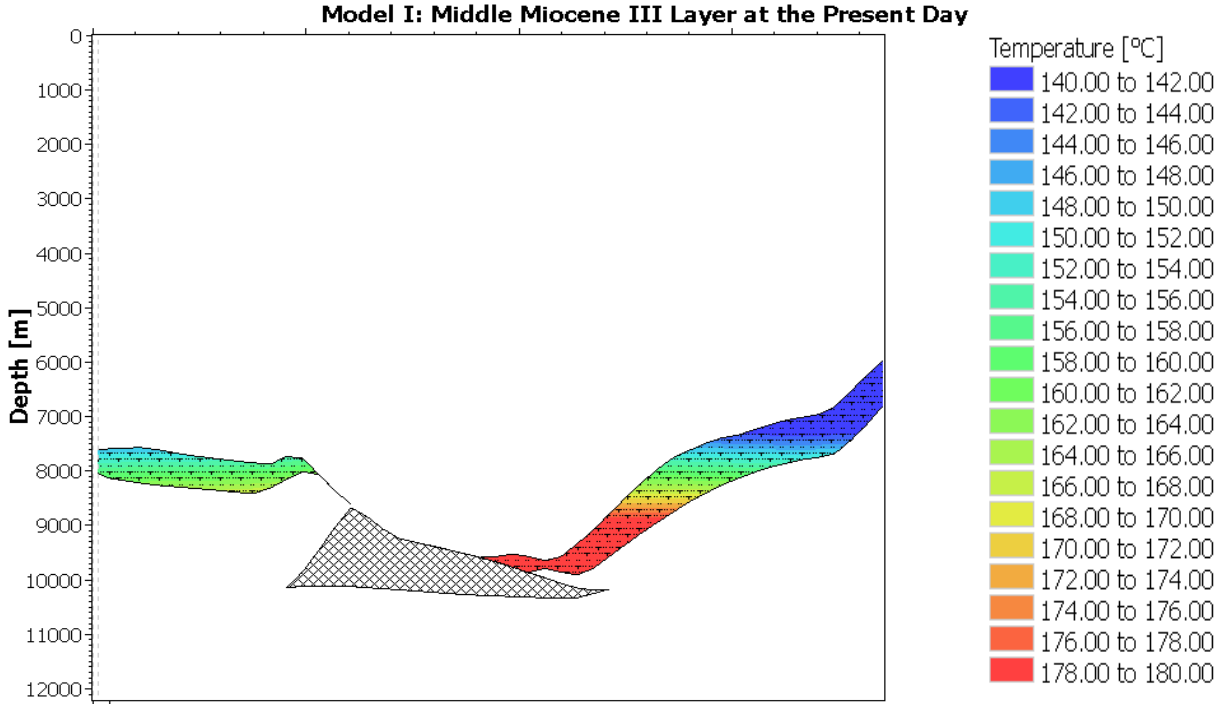
Model I: Middle Miocene III Layer at the Present Day
Depth [m]
0
1000
2000
3000
4000
5000
6000
7000
8000
9000
10000
11000
12000
Temperature [°C]
140.00 to 142.00
142.00 to 144.00
144.00 to 146.00
146.00 to 148.00
148.00 to 150.00
150.00 to 152.00
152.00 to 154.00
154.00 to 156.00
156.00 to 158.00
158.00 to 160.00
160.00 to 162.00
162.00 to 164.00
164.00 to 166.00
166.00 to 168.00
168.00 to 170.00
170.00 to 172.00
172.00 to 174.00
174.00 to 176.00
176.00 to 178.00
178.00 to 180.00

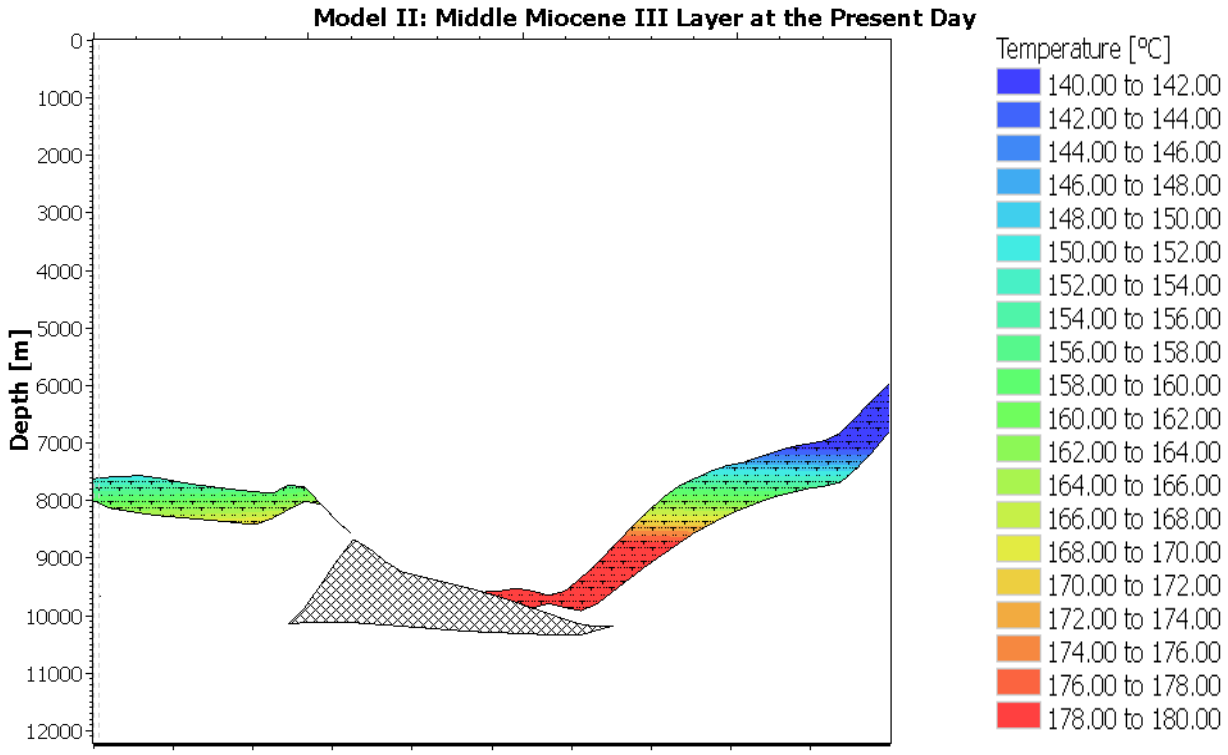

Figure 3. Temperature changes at different time steps for Middle Miocene III layer in both models indicating a higher temperature of the layer in Model II around 12.5 Ma and equilibration of the temperatures in Model II such that the two models have the same present day temperatures.

Conclusions

The results of the two modeling scenarios suggest significant differences in the simulated pore pressure history resulting from porosity-controlled backstripping and paleo stepping methods. These differences are due to variations in overburden pressure and stratigraphic contacts through time between these two models. The magnitude of the differences at present day depends on the behavior of fluid flow dictated by the permeability of the rocks, as well as the time available for fluid flow to equilibrate pore pressure buildups. Similarly, the thermal history predicted by the two techniques can differ depending on the heat generation in the basin, the stratigraphic contacts through time, and the differences in the pore pressure history. Therefore, the importance of applying paleo-stepping methods over porosity-controlled backstripping methods depends on the scope of the problem being addressed by the model, the type of structure and its effects on stratigraphic contacts, the physical properties of the layers, and the heat generation in the basin.

Acknowledgments

The authors thank BP and ExxonMobil for providing the data set used in this study. Funding and participation in this research is made possible through the support of the Stanford Basin and Petroleum System Modeling, Stanford Center for Reservoir Forecasting, and Stanford Rock Physics industrial affiliate programs and through Saudi Aramco Scholarship. Special thanks to Stew Levin (Stanford Exploration Project) for support in setting up the project. Schlumberger graciously provided PetroMod® software. CGG Geosoftware provided the license for Hampson Russell®. Halliburton provided the license to Decision Space Desktop®. We thank the reviewers for useful comments.

References

Al-Hajeri, M. M., M. Al Saeed, J. Derks, T. Fuchs, T. Hantschel, A. Kauerauf, and D. Welte, 2009, Basin and petroleum system modeling: Oilfield Review, v. 21, no. 2, p. 14-29.

Bally, A. W., Gordy, P. L., and Stewart, G. A., 1966, Structure, seismic data, and orogenic evolution of southern Canadian Rocky Mountains: Bulletin of Canadian Petroleum Geology: 14(3), p. 337-381.

Baur, F., Di Benedetto, M., Fuchs, T., Lampe, C., & Sciamanna, S., 2009, Integrating structural geology and petroleum systems modeling–A pilot project from Bolivia's fold and thrust belt. Marine and Petroleum Geology, 26(4), p. 573-579.

Burollet, P. F., 1975, Tectonique en radeaux en Angola: Bulletin de la Société Géologique de France, 17, p. 503–504.

Cobbold, P. R., and P. Szatmari, 1991, Radial gravitational gliding on passive margins: Tectonophysics, 188, p. 249–289.

Dahlstrom, C. D. A., 1969, Balanced cross sections: Canadian Journal of Earth Sciences, 6(4), 743-757.

Duval, B., C. Cramez, and M. P. A. Jackson, 1992, Raft tectonics in the Kwanza Basin: Marine and Petroleum Geology, 9, p. 389–404.

Fort, X., J. P. Brun, and F. Chauvel, 2004, Salt tectonics on the Angolan margin, synsedimentary deformation processes: AAPG Bulletin, 88, p. 1523–1544.

Hantschel, T., A. Kauerauf, 2009, Fundamentals of basin modeling: Berlin, Springer-Verlag, 425 p.

Hantschel, T., Wygrala, B., Fuecker, M. & Neber, A., 2011, Modeling Basin-Scale Geomechanics through Geological Time: International Petroleum Technology Conference, 15-17 November 2011, International Petroleum Technology Conference. Bangkok, Thailand, IPTC 15286.

Hudec, M. R., and M. P. A. Jackson, 2011, The salt mine: A digital atlas of salt tectonics: University of Texas at Austin, Bureau of Economic Geology, Udden Book Series 5 and AAPG Memoir 99.

Jackson, M. P. A., and C. Cramez, 1989, Seismic recognition of salt welds in salt tectonics regimes: SEPM Gulf Coast Section Tenth Annual Research Conference Program and Abstracts, p. 66–71.

Jackson, M. P. A., and C. J. Talbot, 1991, A glossary of salt tectonics: University of Texas at Austin, Bureau of Economic Geology Geologic Circular, 91-4, p. 44.

Lampe, C., K. J. Bird, T. E. Moore, R. A. Ratliff, and B. Freeman, 2012, Modeling^3: Integrating structural modeling, fault property analysis, and petroleum systems modeling—An example from the Brooks Range foothills of the Alaska North Slope, in K. E. Peters, D. J. Curry, and M. Kacewicz, eds., Basin and petroleum system modeling—2009 Napa

Hedberg Conference, v. Hedberg Series No. 4: Tulsa, Okla., American Association of Petroleum Geologists Hedberg Series No. 4, p. 119-136.

Lapinski, T., R. Bouroullec, and P. Weimer, 2004, Structural evolution of the Thunder Horse mini-basin, Mississippi Canyon, northern deep Gulf of Mexico: Gulf Coast Association of Geological Societies Transactions, v. 54, p. 313-326.

Lapinski, T., P. Weimer, and R. Bouroullec, 2004, Sequence stratigraphic evolution of Thunder Horse mini-basin, Mississippi Canyon, northern deep Gulf of Mexico: Gulf Coast Association of Geological Societies Transactions, v. 54, p. 327-341.

Lundin, E. R., 1992, Thin-skinned extensional tectonics on a salt detachment, northern Kwanza Basin, Angola: Marine and Petroleum Geology, 9, p. 405–411,

Marshak, S. and N.B. Woodward, 1988, Introduction to cross-section balancing, *in* S. Marshak, and G. Mitra, eds., Basic methods of structural geology: Englewood Cliffs, Prentice Hall, p. 303-332.

Nikolinakou, M., Luo, G., Hudec, M.R., Flemings, P.B., 2012. Geomechanical modeling of stresses adjacent to salt bodies: Part 2-Poroelasticity and coupled overpressures: AAPG Bulletin, 96(1), p. 65-85.

Pilcher, R. S., Murphy, R. T., & McDonough Ciosek, J., 2014, Jurassic raft tectonics in the northeastern Gulf of Mexico. Interpretation, 2(4), SM39-SM55.

Rowan, M. G., 1993, A systematic technique for the sequential restoration of salt structures; Tectonophysics, 228(3-4), p. 331-348.

Rouby, D., Guillocheau, F., Robin, C., Bouroullec, R., Raillard, S., Castelltort, S., and Nalpas, T., 2003, Rates of deformation of an extensional growth fault/raft system (offshore Congo, West African margin) from combined accommodation measurements and 3-D restoration. Basin Research, 15(2), p. 183-200.

Vendeville, B. C., and M. P. A. Jackson, 1992, The fall of diapirs during thin-skinned extension: Marine and Petroleum Geology, 9, p. 354–371.

INCORPORATING THE FRICTIONAL STRESS LIMIT INTO BASIN AND PETROLEUM SYSTEM MODELS IMPROVES STRESS AND PORE PRESSURE PREDICTIONS OF CRITICALLY STRESSED SEDIMENTARY BASINS

Laainam (Best) Chaipornkaew[1,*], Tapan Mukerji[2], Allegra Hosford Scheirer[1], and Noelle Schoellkopf[3]

[1]*Department of Geological Sciences, Stanford University, Stanford, CA*
[2]*Department of Energy Resources Engineering, Stanford University, Stanford, CA*
[3]*Software Integrated Solutions (SIS), Schlumberger, Danville, CA*
[*]bestc@stanford.edu

Abstract

Calculated stresses and strains depend on basin-scale geomechanical framework through geologic time. Basin and petroleum system modeling (BPSM) can describe the evolution of physical properties in sedimentary basins in a robust manner by simulating a dynamic mechanical earth model in geologic time (Meng et al., 2006; Al-Hajeri et al., 2009; Hantschel and Kauerauf, 2009). Despite this great potential, several published studies using BPSM for pore pressure predictions in structurally complex regions show inaccurate results due to a lack of advanced rock failure modeling (Hantschel et al., 2011; Burgreen-Chan et al., 2016).

The poroelastic BPSM of the East Coast Basin (ECB) of New Zealand by Burgreen-Chan et al., (2016) shows reasonable estimations of stress except at present day. Observations of fractures in outcrops (Field et al., 2004) indicate that fracturing likely began during the onset of subduction at the transpressional plate boundary. By not considering the frictional stress limit at which failure occurs, the predictions of Burgreen-Chan et al. (2015) for pore pressure become erroneous as stresses exceed shear criterion (**Figure 1**).

Because material responds differently to confining pressure, especially in an inelastic regime, under lower confining pressure materials can fail macroscopically on pre-existing weak planes as stress goes beyond the frictional limit. Like most crustal rocks that are in failure equilibrium, reactivation of fault slippage in the ECB could dissipate accumulated pressure with only a small perturbation. Additionally, the effective frictional strength of the crust also depends on the pore pressure at depth (Zoback and Townend, 2001). Given the interplay between critically-stressed faulted rock and elevated pore pressure, this research utilizes geomechanical analysis of the frictional stress limit to improve stress prediction in BPSM.

The relationship among principle stresses (S_1 and S_3), fluid pore pressure (P_f), and the frictional coefficient (μ) can be related by rearranging the Coulomb frictional faulting theory (eq. 1). For the differential stress as a function of depth in frictional equilibrium, maximum differential stress at failure (for a given mean stress) decreases with pore pressure (Zoback and Townend, 2001; Zoback, 2010).

$$\frac{S_1 - P_f}{S_3 - P_f} = (\sqrt{\mu^2 + 1} + \mu)^2 \qquad \text{(eq. 1)}$$

The horizontal stress, vertical stress, and pore fluid pressure are extracted from Lachlan Basin, Inboard, and Outboard Regions of the ECB (**Figure 2**). The ratios $(S_1 - P_f)/(S_3 - P_f)$

from these locations at multiple timesteps are within an expected range with some outliers. Ultimately, these ratios can provide crucial conditions for the upper limit of stress predictions with the assumption that critically-stressed faults and fractures are hydraulically conductive such that they dissipate pressure buildups (Byerlee, 1968; Zoback and Townend, 2001; **Figure 3**).

There are two proposed source rocks in the ECB: the Whangai Formation and the Waipawa Black Shale. The siliceous (more brittle) Whangai Formation has been experiencing rock failure since the beginning of the Neogene (Darby and Funnell, 2001; Field et al., 2004). In contrast, plastic deformation may be important to consider for the (more ductile) Waipawa Black Shale due to its clay-rich lithology. This research also applies a poroplastic material law in the Waipawa Black Shale to determine the effect of plasticity in predicting stress and overpressure history in the basin. User-defined plastic material facilitates significant compaction due to non-recoverable porosity loss, and allows for a more realistic prediction within the Coulomb failure zone (Hantschel et al., 2011; Nikolinakou, 2011).

This study showcases the impact of inelastic deformation in the ECB, emphasizing the importance of incorporating rock failure analyses into BPSM where tectonic settings are prone to inelastic deformation. Applying geomechanical tools to capture full-spectrum effects between the brittle and ductile behaviors highlights the substantial differences in BPSM predictions of stress and pore pressure from the base case that assumes pure elasticity. Lastly, this study may even imply if the brittle-ductile transition (**Figure 4**) is achievable based on the confining pressure conditions associated with burial and uplift history of the ECB (Wei and Anand, 2008).

Figures

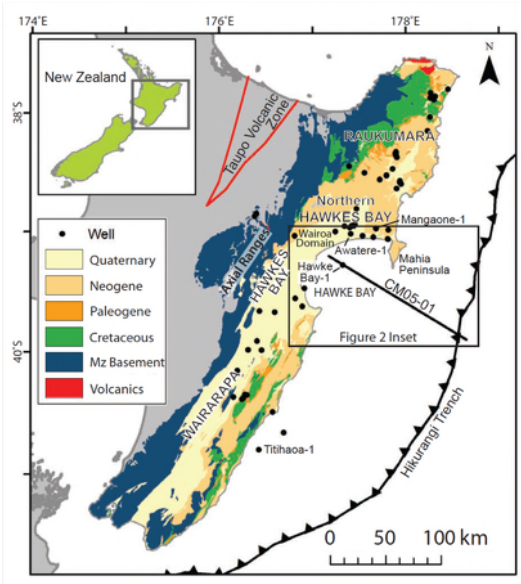

Figure 1. Development of overpressure in the East Coast Basin (ECB), New Zealand for four of the eight structurally restored time steps. The Wanstead Formation, a regional seal rock, is highlighted in white. Overpressure prediction becomes unrealistic near present-day, clearly shown at 4Ma (Burgreen-Chan et al., 2016). V.E. ~1.8.

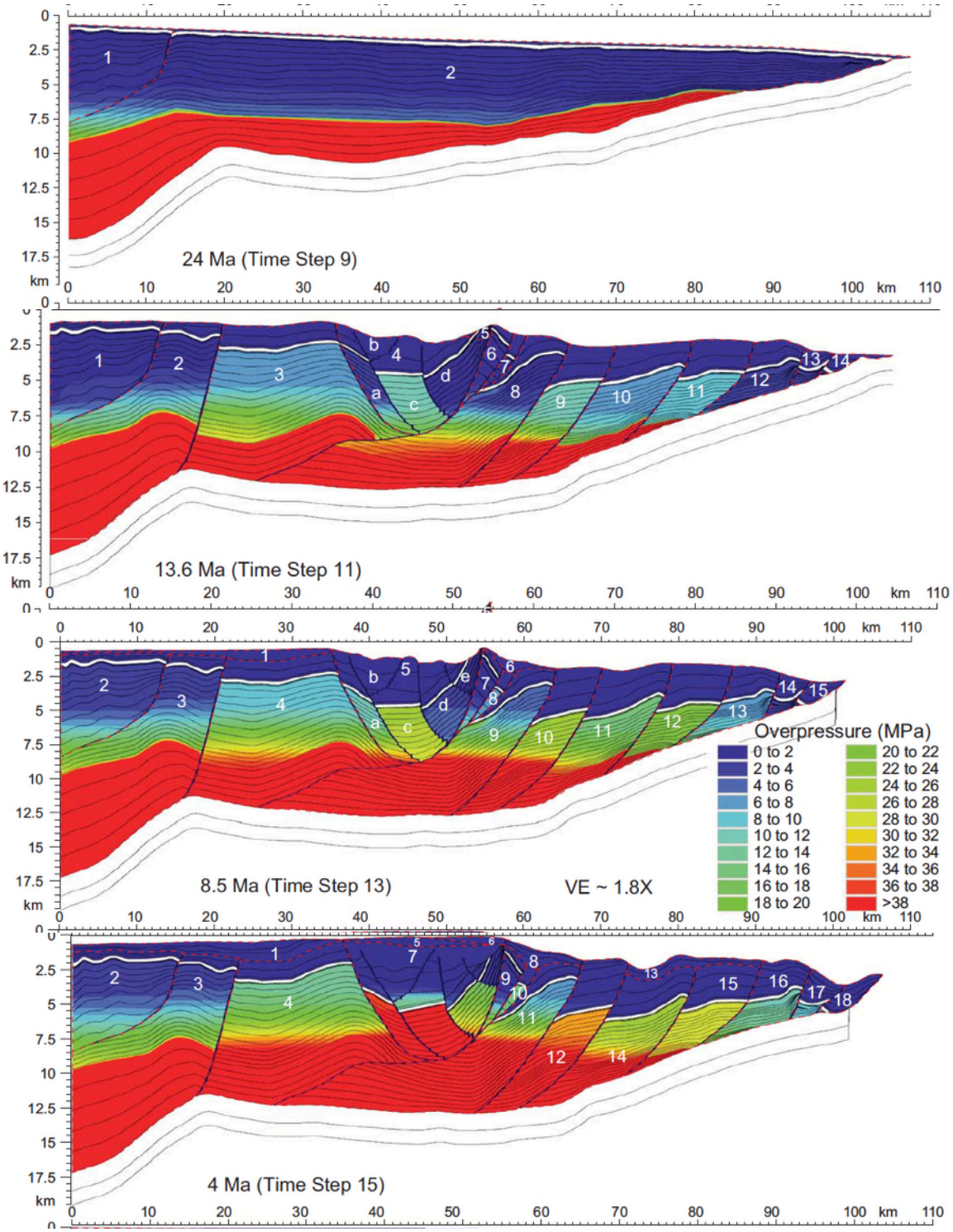
24 Ma (Time Step 9)
13.6 Ma (Time Step 11)
8.5 Ma (Time Step 13)
VE ~ 1.8X
4 Ma (Time Step 15)
Overpressure (MPa)
0 to 2
2 to 4
4 to 6
6 to 8
8 to 10
10 to 12
12 to 14
14 to 16
16 to 18
18 to 20
20 to 22
22 to 24
24 to 26
26 to 28
28 to 30
30 to 32
32 to 34
34 to 36
36 to 38
>38
km

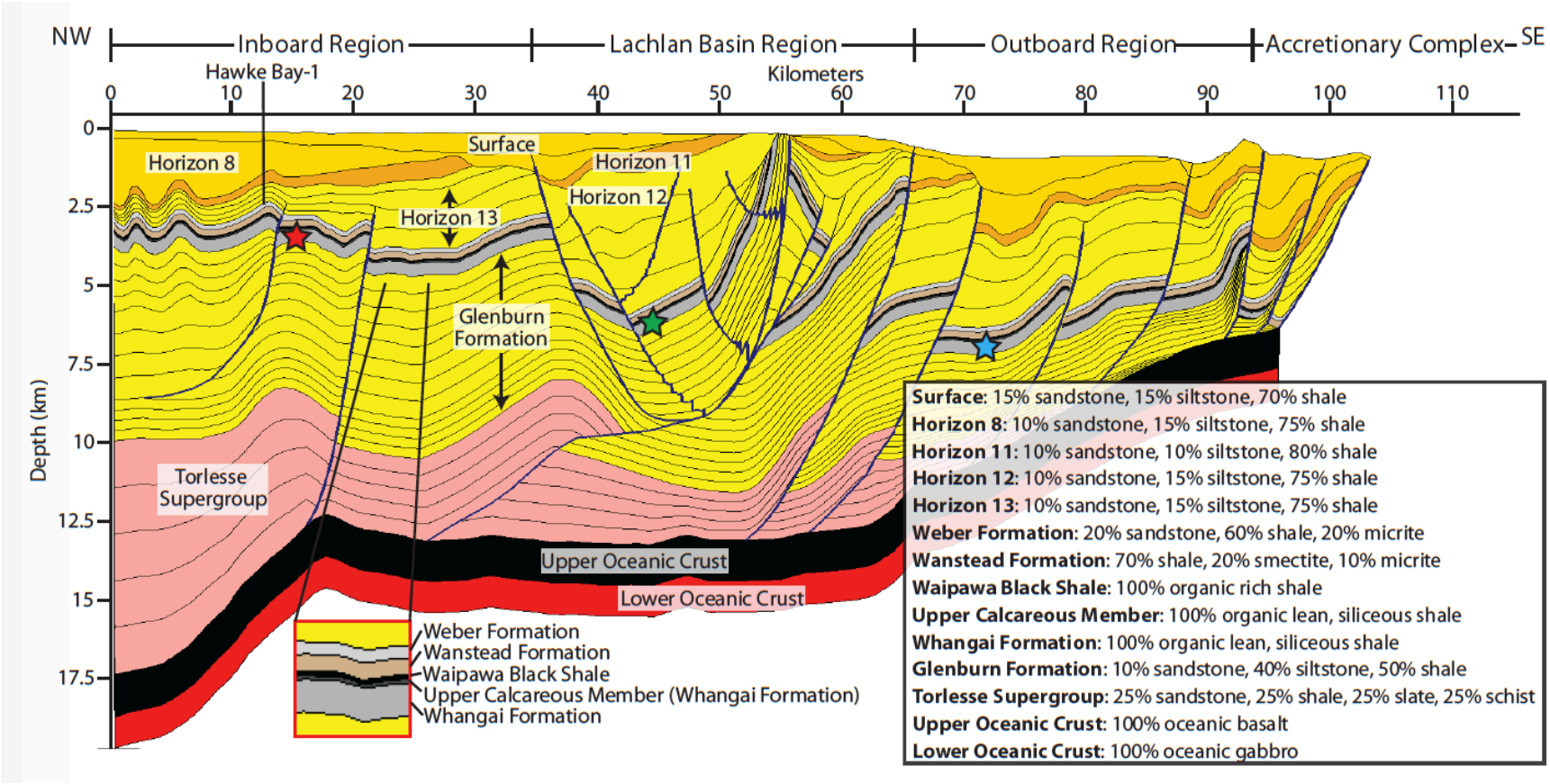

Figure 2. Present-day lithostratigraphy of the ECB across line CM05-01. Lithologic composition is assumed constant through time. Red, green, and blue stars represent the Inboard region, the Lachlan Basin region, and the Outboard region respectively. These locations are used to extract stress and pore pressure data for analysis of the faulting regime using Coulomb frictional faulting theory (Burgreen-Chan et al., 2016).

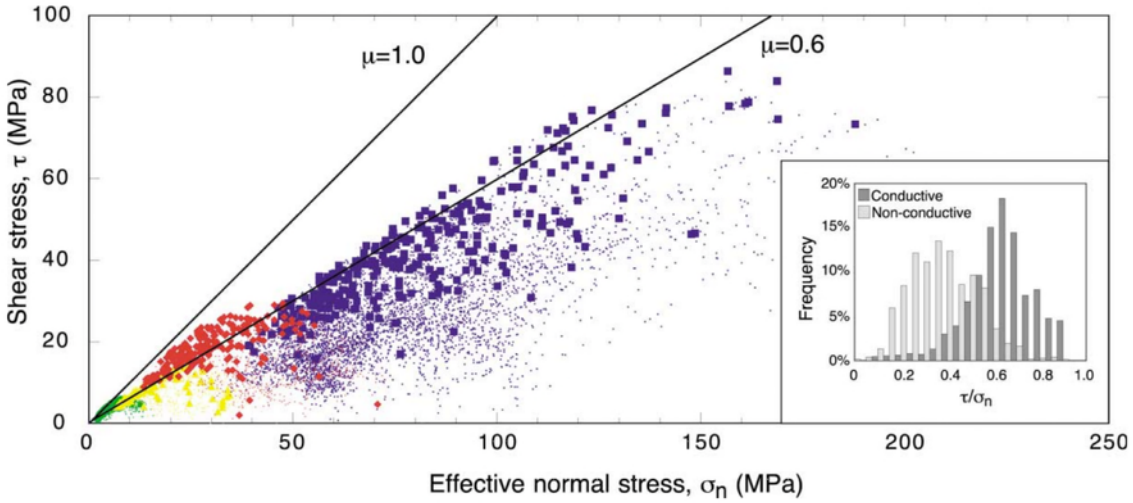

Figure 3. Shear and effective normal stresses on fractures in the Cajon Pass. The filled symbols represent hydraulically conductive fractures and faults, and the dots represent non-conductive fractures. The two lines represent frictional coefficients, 0.6 is conventionally used to represent fracture and fault in failure equilibrium (Zoback and Townend, 2001).

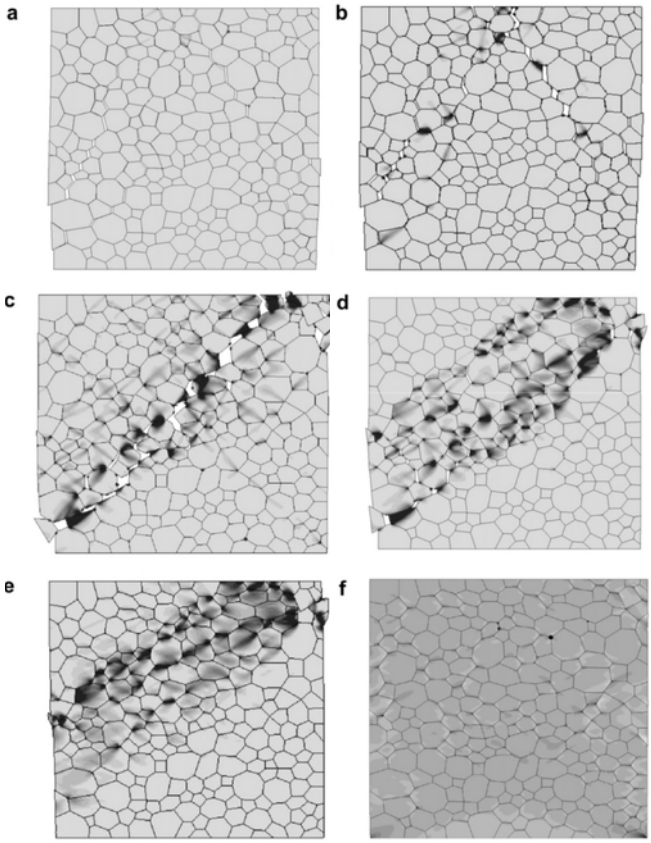

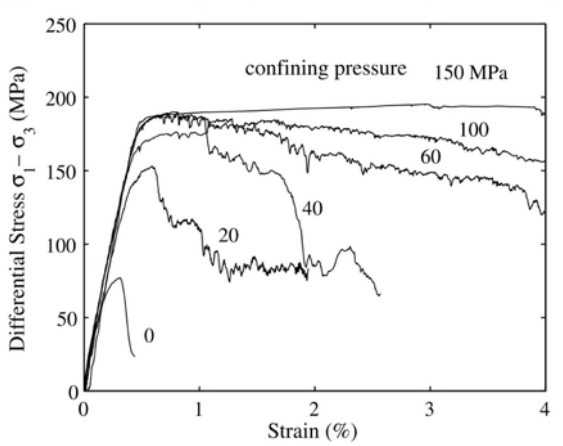

Figure 4. Simulation of plastic strain contours in grain-interiors in specimens compressed at different confining pressure. The deformation microstructures shown in panels a to f correspond to increasing confining pressure (0 to 150MPa). At lower confining pressure, the model is dominated by grain-boundary slip. At higher confining pressure, grain-interior plasticity dominates (Wei and Anand, 2008).

References

Al-Hajeri, M. M., M. Al Saeed, J. Derks, T. Fuchs, T. Hantschel, A. Kauerauf, M. Neumaier, O. Schenk, O. Swientek, and N. Tessen, 2009, Basin and petroleum system modeling: Oilfield Review, v. 21, no. 2, p. 14–29.

Burgreen-Chan, B., K. E. Meisling, and S. Graham, 2016, Basin and petroleum system modelling of the East Coast Basin, New Zealand: A test of overpressure scenarios in a convergent margin: Basin Research, v. 28, no. 4, p. 536–567, doi:10.1111/bre.12121.

Byerlee, J. D., 1968, Brittle-ductile transition in rocks: Journal of Geophysical Research, v. 73, no. 14, p. 4741–4750.

Darby, D., and R. H. Funnell, 2001, Overpressure associated with a convergent plate margin: East Coast Basin, New Zealand: Petroleum Geoscience, v. 7, no. 3, p. 291 LP-299.

Field, B. D., K. E. Higgs, F. Chanier, A. Nicol, and D. Darby, 2004, Play concepts for a complex margin: East Coast North Island, New Zealand, *in* 2004 New Zealand Petroleum Conference Proceedings, Ministry of Economic Development, Wellington, New Zealand.

Hantschel, T., and A. I. Kauerauf, 2009, Fundamentals of basin and petroleum systems modeling: 476 p., doi:10.1007/978-3-540-72318-9.

Hantschel, T., B. Wygrala, M. Fuecker, and A. Neber, 2011, Modeling basin-scale geomechanics through geological time: International Petroleum Technology Conference, no. i, p. 6, doi:10.2523/15286-MS.

Meng, Z., J. Zhang, and S. Peng, 2006, Influence of sedimentary environments on mechanical properties of clastic rocks: Environmental Geology, v. 51, no. 1, p. 113–120, doi:10.1007/s00254-006-0309-y.

Nikolinakou, M. a, 2011, Geomechanical modeling of stresses adjacent to salt bodies : 2 . poro-elasto-plasticity and coupled overpressures: AAPG Bulletin, v. 1, no. 1, p. 65–85, doi:10.1306/04111110143.

Wei, Y., and L. Anand, 2008, On micro-cracking, inelastic dilatancy, and the brittle-ductile transition in compact rocks: A micro-mechanical study: International Journal of Solids and Structures, v. 45, no. 10, p. 2785–2798, doi:10.1016/j.ijsolstr.2007.11.028.

Zoback, M. D., 2010, Reservoir geomechanics: Cambridge University Press, 449 p.

Zoback, M. D., and J. Townend, 2001, Implications of hydrostatic pore pressures and high crustal strength for the deformation of intraplate lithosphere: Tectonophysics, v. 336, no. 1–4, p. 19–30, doi:10.1016/S0040-1951(01)00091-9.

THE EFFECT OF THERMAL MATURITY ON THE ELASTIC PROPERTIES OF ORGANIC-RICH MUDROCKS–A CASE STUDY OF THE SHUBLIK FORMATION, ALASKA

Mustafa Al Ibrahim[1,*], Tapan Mukerji[1], Allegra Hosford Scheirer[2], Inessa Yurchenko[2]
[1]*Department of Energy Resources Engineering, Stanford University, Stanford, CA*
[2]*Department of Geological Sciences, Stanford University, Stanford, CA*
[*]malibrah@stanford.edu

Abstract
Predicting the properties of organic-rich mudrocks is essential for the efficient exploitation of these unconventional resources. In emerging areas, well data is sparse and, as a consequence, purely data-driven geostatistical methods are not sufficient for the characterization of heterogeneous mudrocks. Seismic data can be used to estimate different properties if an accurate rock model is constructed. In this study, effective medium theory is used to model the elastic properties of organic rich mudrocks as a function of thermal maturation. The model is applied on the Shublik and Fire Creek formations in North Slope, Alaska. Kerogen is modeled as a function of thermal maturation, incorporating the creation of organic pores and densification of solids. The matrix is modeled as a vertical transverse isotropic medium. Pores in both the kerogen and matrix are inserted using differential effective medium theory. Gassmann substitution is used to fill pores with hydrocarbons. Results show a good correlation with compressional and shear sonic logs, with correlation coefficients of 0.89 and 0.84 respectively. Comparison with bulk density log is not ideal; the correlation coefficient is only 0.29. Based on reasonable assumptions, it can be shown from sensitivity studies that elastic properties are not sensitive to thermal maturation if lithology and total organic carbon are unknown.

Introduction
Successful characterization of source rock properties is essential for emerging resource plays. Inverted seismic data can be used to infer some of these properties if an accurate elastic model is constructed. The inversion of seismic data to rock properties in source rock is more complicated than in conventional rocks. That is because the elastic properties of these rocks are controlled by 1) lithological components, 2) amount and shape of pores, and 3) thermal maturation (which controls the kerogen and fluid properties). Thus, an elastic template that incorporates all these factors needs to be constructed prior to inversion.

Several studies have focused on constructing rock physics templates for organic-rich mudrocks in recent years. For example, Zhu et al. (2012) modeled shale gas reservoirs as isotropic media using inclusion models and concluded that with increasing organic content, P-impedance and Vp/Vs ratio decreases. Carcione et al. (2011) modeled source rocks as transversely isotropic medium and compared Backus and Krief/Gassmann models. They were able to fit the Krief/Gassmann model to their data. Altowairqi et al. (2015) measured the elastic properties as a function of total organic carbon on synthetic samples. They confirmed that with increasing total organic carbon: 1) velocity significantly decrease, 2) density decreases, and 3) total porosity increases. Specific studies on kerogen include Zargari et al. (2016) in which they used nanodynamic mechanical analysis to show that the moduli of the kerogen particles generally decrease as a function of thermal maturity. Zhao

et al. (2016) modeled elastic properties of organic shale at different maturity stages. The effective medium theories used at different maturity stages are chosen based on the kerogen interaction with the inorganic matrix. The kerogen is assumed to act as a load-bearing component in immature rocks and as an inclusion-filling component in overmature rocks. They concluded that the elastic response is mostly sensitive to organic matter content and mineralogy.

Rock physics templates have been used in the past to characterize geochemical properties of organic-rich mudrocks on the seismic scale in different ways by: 1) estimation of total organic carbon (TOC) from acoustical impedance (e.g., Løseth et al, 2011; Ogiesoba and Hammes, 2014; Broadhead et al., 2016), and 2) estimation of TOC from acoustical and shear impedances (e.g., Hu et al., 2005). Note that while most studies use acoustical impedance for estimation of TOC, Hu et al. (2005) observed that acoustical impedance by itself is not a good predictor of TOC in the Eagle Ford and therefore used simultaneously-inverted acoustic and shear impedance cubes for prediction. This case study uses the Shublik interval in North Slope, Alaska for constructing an elastic template for organic-rich mudrocks while incorporating thermal maturation. The Shublik is complex because of its varying lithology and TOC in both the vertical and lateral direction (e.g., Yurchenko et al., this abstract volume).

Methodology

Figure 1 shows the general workflow followed. First, the effect of kerogen thermal maturation is studied separately by accounting for the physical changes in kerogen matter as it matures. The resultant effective elastic properties of the kerogen are then combined with a rock matrix based on the spatial distribution and alignment of minerals and kerogen. Inputs for the model can be obtained from different sources. Note that each data source will have its own scale and its associated uncertainties. Mineralogical data can be obtained from inversion of elemental data of well logs such as elemental capture spectroscopy (e.g., Claverie et al., 2006), inversion of conventional well logs (e.g., Steiner et al., 2015), x-ray diffraction from cores or cuttings, or inversion of x-ray fluorescence data from cores or cuttings. Pore fraction of kerogen can be estimated from well logs (e.g., Alfred and Vernik, 2012; Galdford et al., 2013) or by calculation from a model (e.g., Modica and Lapierre, 2012). TOC data is obtained from pyrolysis analysis or estimated from different other sources such as well logs (e.g., Schmoker, 1979; Passey, 1991; Issler et al., 2002). Kerogen thermal maturation can be estimated from pyrolysis or reasonably assumed from the literature (e.g., Jarvie et al., 2007).

Geologic Setting

The Upper Triassic Shublik Formation is considered one of the main source rocks in the North Slope, Alaska (Stadnichenko and White, 1929; Magoon and Bird, 1985; Peters et al., 2006). Parrish et al. (2001) identified four main lithofacies in the Shublik and interpreted the deposits as marine in nature and related to an upwelling zone. The studied interval spanning the Upper Triassic Fire Creek and Shublik formations can be subdivided into different members corresponding to distinct lithofacies. Of importance to this study, thin section analysis generally shows amorphous Type II/III organic matter with average vitrinite reflectance of 1.2 (minimum is ~1 and maximum is ~1.4). This is in agreement with previous studies such as Magoon and Bird (1985).

Matrix Mineralogical Estimation

Proportions of the different minerals comprising the mudrocks are needed for elastic modeling. Linear inversion is used to estimate mineral proportions from elemental data. The implementation used here is similar to the one proposed by De Caritat et al (1994). The algorithm uses linear optimization to solve for the best mineral combination, defined as that which minimizes the total error between the elemental proportion observations and the modeled ones under the constraints given in Figure 2. Slack variables are used to account for unknown minerals in the rock (Figure 2). The inverted results are in mass proportions and are then converted to volumetric proportion assuming known mineral densities. In this case study, the elemental data is obtained using a handheld x-ray fluorescence device (Bruker Tracer) (Yurchenko et al., 2016). Calibration is applied to convert the x-ray fluorescence count to mass percentage using the relationships proposed by Rowe et al (2012). Table 1 shows mineral properties used in this study. Note that pyrite and apatite are included in the inversion because x-ray diffraction and core observations confirmed that they are relatively abundant in some intervals in these rocks. Inversion results are compared to x-ray diffraction and carbonate analysis done on samples throughout the interval (Figure 3). There is a general correlation between the two methods.

Elastic Modeling of Organic Rich Mudrocks

Thermal maturation of kerogen will affect its elastic properties. Thus, the effect of thermal maturity must be studied before its inclusion with other components of the rock. Three effects are studied here as a function of thermal maturation (Figure 4): 1) the formation of nanopores (also known as organic pores), 2) the generation of fluids including oils and gas, and 3) the alteration of the remaining kerogen as the fraction of carbon increases relative to hydrogen.

Immature kerogen is assumed to initially have zero pore fraction. With increasing thermal maturation, nanopores form. Kerogen nanopores are recognized as a major component in kerogens, and can vary as a function of kerogen type and thermal maturation (e.g. Loucks et al., 2009; Curtis et al., 2012). In this study, nanopores are assumed to be spherical, uniform in spatial distribution, and filled with either oil or gas. The assumption of spherical nanopores is made based on observations from scanning electron scanning microscopic studies. For example, Loucks et al. (2009) identified nanopores that have a relatively elliptical cross section of varied sizes ranging from 5 to 750 nanometers. Tube-like pore throats connect these nanopores.

A linear relationship modified from Medica and Lapierre (2012) is used to model the evolution of pores in kerogen as function of the transformation ratio (TR) where k is the ratio of kerogen mass to labile mass, $\phi_{Kerogen}$ is the pore fraction, and Cc is the lability of the organic matter (Equation 1). Lability is the fraction of organic carbon that can be converted to hydrocarbon and is typically less than 0.5 (Medica and Lapierre, 2012). It can be estimated from hydrogen index data since hydrocarbon generation is generally limited by the amount of hydrogen in the organic matter (e.g. Daly and Edman, 1987).

Reasonable estimates of type II source rock for k (1.118) and Cc (.36) are used (Medica and Lapierre, 2012). The kerogen pore fraction and the effective kerogen density are obtained

(Figure 5). Note that kerogen pore fraction reaches its maximum at k×Cc (~40%). To get a sense of this number, the estimated total pore fraction increase would be about 8% given a rock with non-kerogen density of 2400 kg/m^3 and a TOC of 5 weight %. Examining the density plot, it is noted that there is only a slight decrease in the kerogen effective density if the model takes into account the increase in the density of solid kerogen matter as a function of thermal maturation.

To model the elastic properties of kerogen, differential effective medium (DEM) theory (e.g. outlined in Mavko et al., 2009) was used to insert dry spherical inclusions (i.e. pores). Gassmann's (1951) relations are then used to fill the pores with fluids. The elastic moduli of kerogen solids are assumed to be constant with a bulk modulus value of 6.8 GPa and shear modulus of 3.8 GPa (Tran, 2014 after Vernik, 1994). Note that Yan and Han (2013) observed about 1 GPa increase in the bulk modulus proportional to an increase in density of about 500 kg/m3 in natural samples. In their work artificially heated samples did not show a clear trend even though kerogen density did increase.

Kerogen solid matter densification occurs with maturation (Okiongbo et al., 2005). The density of the remaining kerogen ($\rho_{Kerogen}$) is generally modeled as a function of vitrinite reflectance (Ro) as a linear function (e.g., Ward, 2010) or a nearly linear function (e.g. Alfred and Vernik, 2012). Alfred and Vernik's (2012) relationship is used in this study (Equation 2). The relationship between the transformation ratio and vitrinite reflectance is given in Equation 3.

$$\phi_{Kerogen} = k \ \ Cc \ \ TR \tag{1}$$

$$\rho_{Kerogen} = 1.293 \ Ro^{0.2} \tag{2}$$

$$TR = \frac{100\%}{(1+20645.5 \ e^{-12.068 \ Ro})} \tag{3}$$

Results from the previous section are combined with a porous rock matrix to study the effects of lithology, maturation, and total organic content on the estimated elastic properties using an anisotropic model. In this model, the matrix is vertical transversely isotropic (VTI) calculated using the Backus average, and pores are elliptical pores (with an aspect ratio) inserted using the DEM model. Figure 6 shows an example of the effect of thermal maturation on the bedding perpendicular compressional velocity.

Case Study

Practically, matrix pore fraction is calculated from the density log. Kerogen porosity contributes a maximum of about 5.2% to the total porosity in the interval. These estimates are in line with the results of Tran (2014), where the maximum kerogen pore fraction was found to be 6.4% using Alfred and Vernik's (2012) model in the same interval. The effect of thermal maturation on the elastic properties of the rock can be studied. Results show a closer match to observed values when the thermal maturation is set to be equal to the measured Ro value of 1.2. This indicates that the model used is reasonable in physically explaining the thermal maturation process. Figure 7 shows the modeled bedding-

perpendicular velocities and density as compared to measurements from well logs. The estimated compressional and shear velocities have a good correlation with well log values. The matrix pores aspect ratio was used to fine-tune the model. An aspect ratio of 0.2 was found to be optimum.

Conclusions and Final Remarks

We present a workflow to model the elastic properties of organic-rich mudrocks as a function of thermal maturation. Importantly, the workflow can be applied on exclusively well log data (given the right well logs). A number of general conclusions can be made from this case study. First, the effect of thermal maturation cannot be ignored in elastic modeling of organic-rich mudrocks if lithology is known. Second, the inclusion of relatively minor constituents such as pyrite, or other minerals that are uncommon, such as apatite in this case, is sometimes important to obtain a good fit. Finally, model parameters such as pore aspect ratio can be used to fine-tune the model. The ultimate goal of this study is to use the model constructed in probabilistic prediction of rock properties from inverted seismic data. Practically, inversion for thermal maturation and TOC is possible if other parameters are relatively constrained.

Figures and Tables

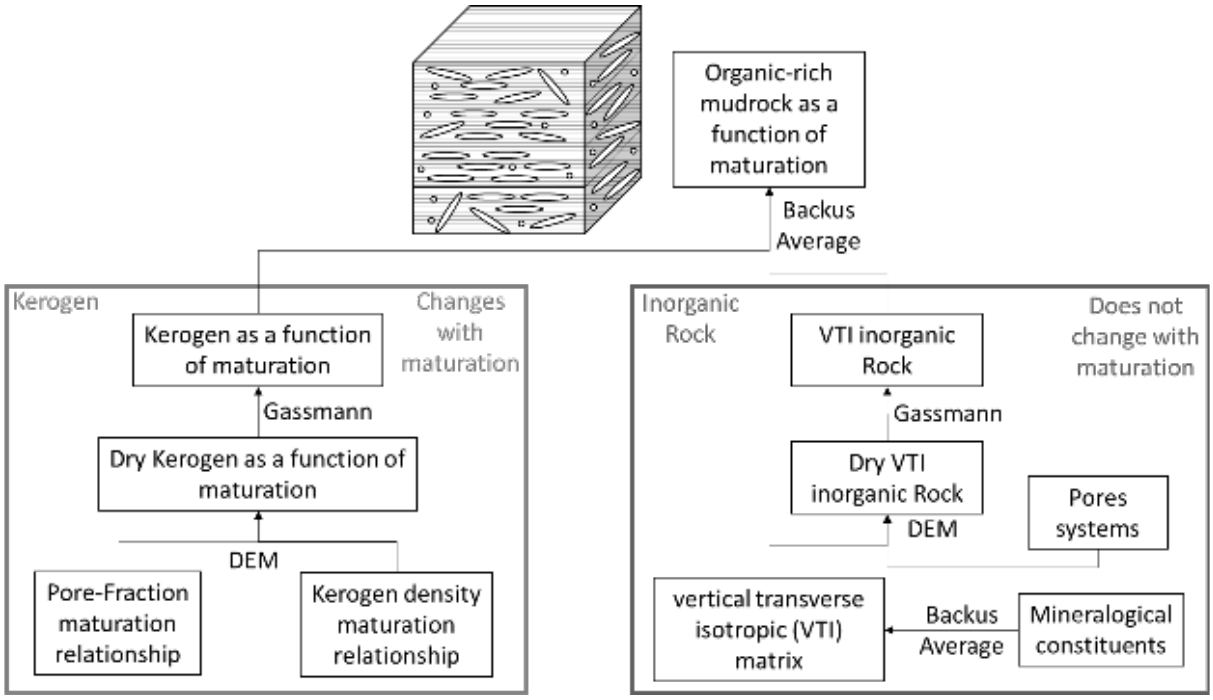

Figure 1. Workflow for modeling the elastic properties of organic-rich mudrocks as a function of thermal maturation.

$$Ax = b$$

$$A_{element\ ,mineral} = \frac{\#Atoms_{element\ \ in\ mineral} * W_{element}}{W_{mineral}}$$

$$b_{element} = x_{element} - s_{element}$$

$$\sum x_{element} = 1$$

$$0 \leq x_{element} \leq 1$$

Figure 2. Linear optimization system solved in the element to mineral inversion.

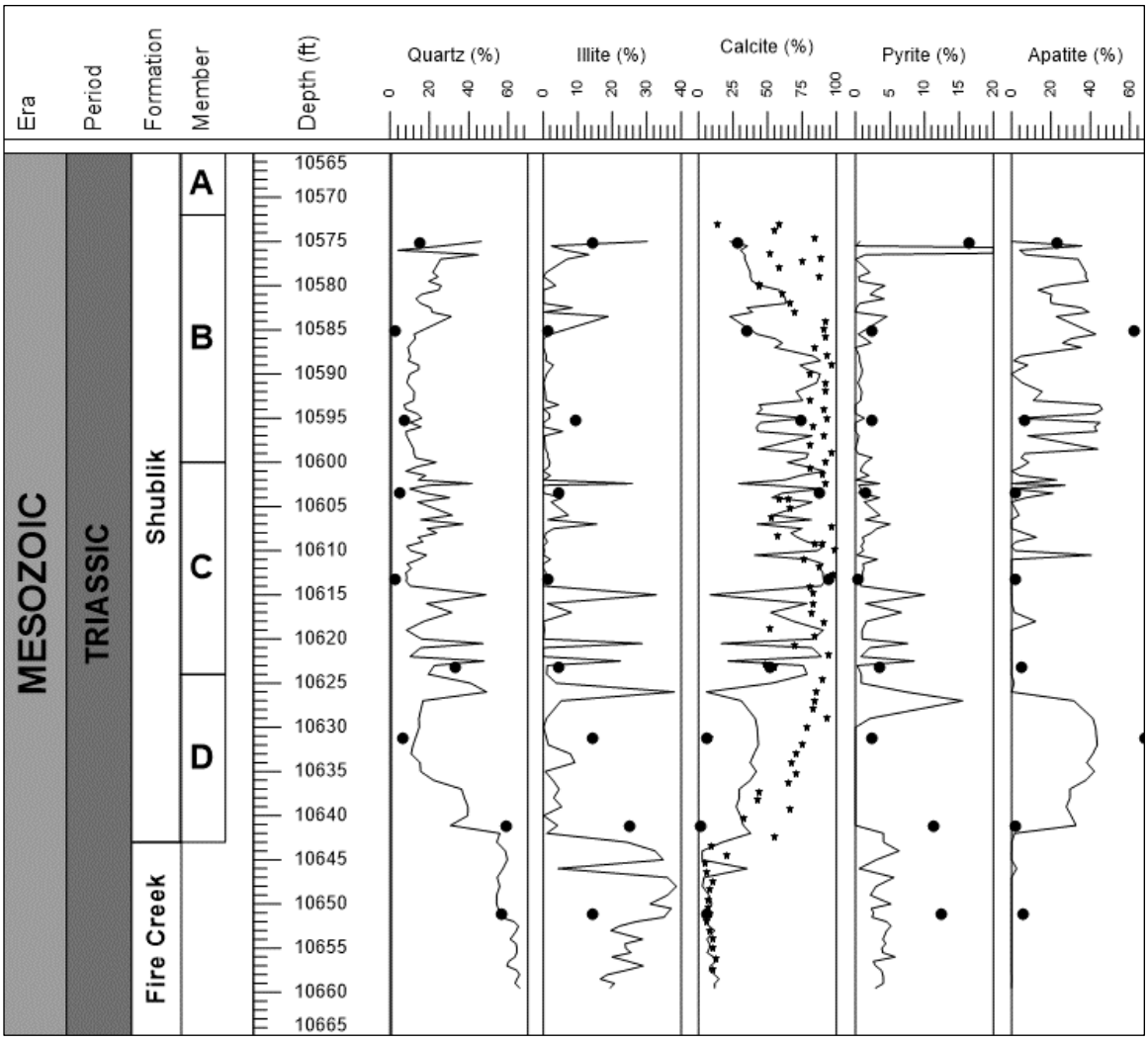

Figure 3. Element to mineral inversion. Circles are data measurements using x-ray diffraction at ~0.3 ft spacing. Stars (calcite log) are bulk carbonate percentage measurements.

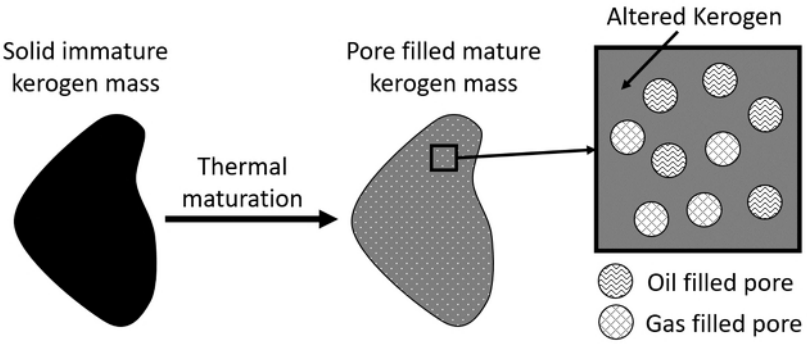

Figure 4. Representation of modeled thermal maturation effects on kerogen.

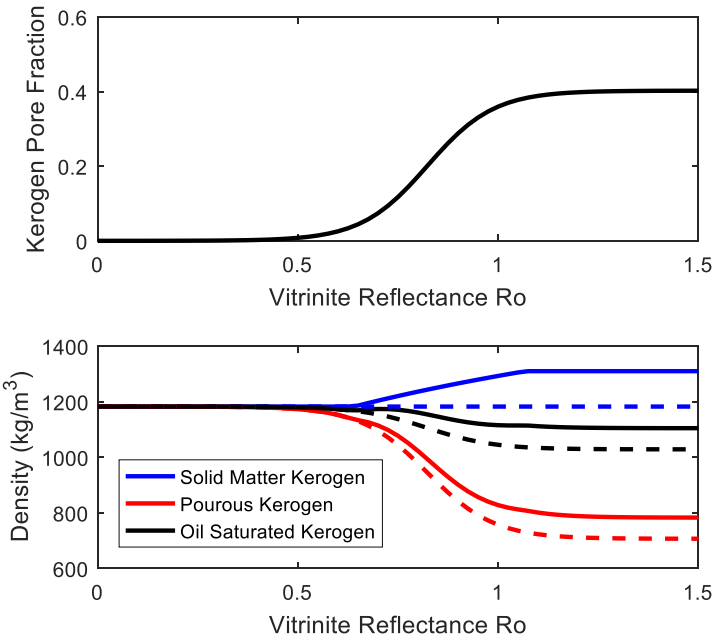

Figure 5. Modeled kerogen pore fraction and density as a function of thermal maturation. In modeling density, two scenarios are considered where density of the remaining kerogen 1) remains constant (dashed lines), and 2) increases as a function of thermal maturation (solid lines).

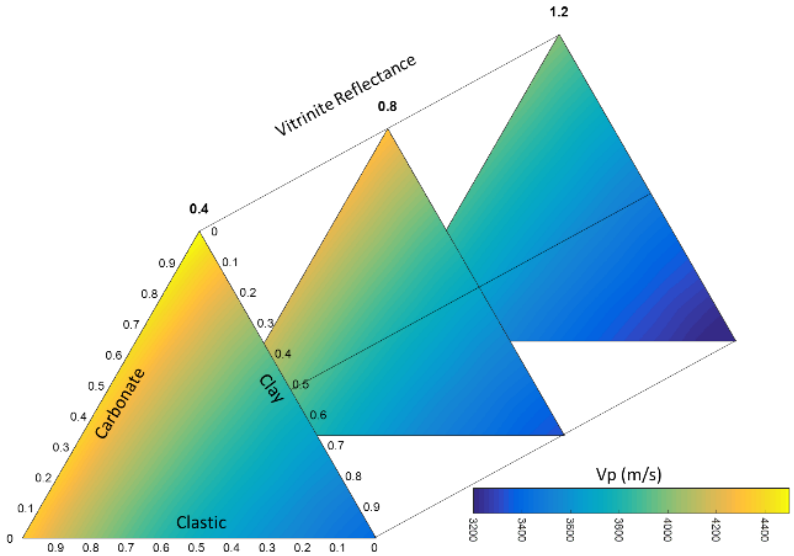

Figure 6. Bedding-perpendicular compressional velocity as a function of thermal maturation for different mineralogical compositions for the VTI rock model. Matrix pore fraction is 0.1 (aspect ratio of 0.2) and kerogen volume fraction is 0.1.

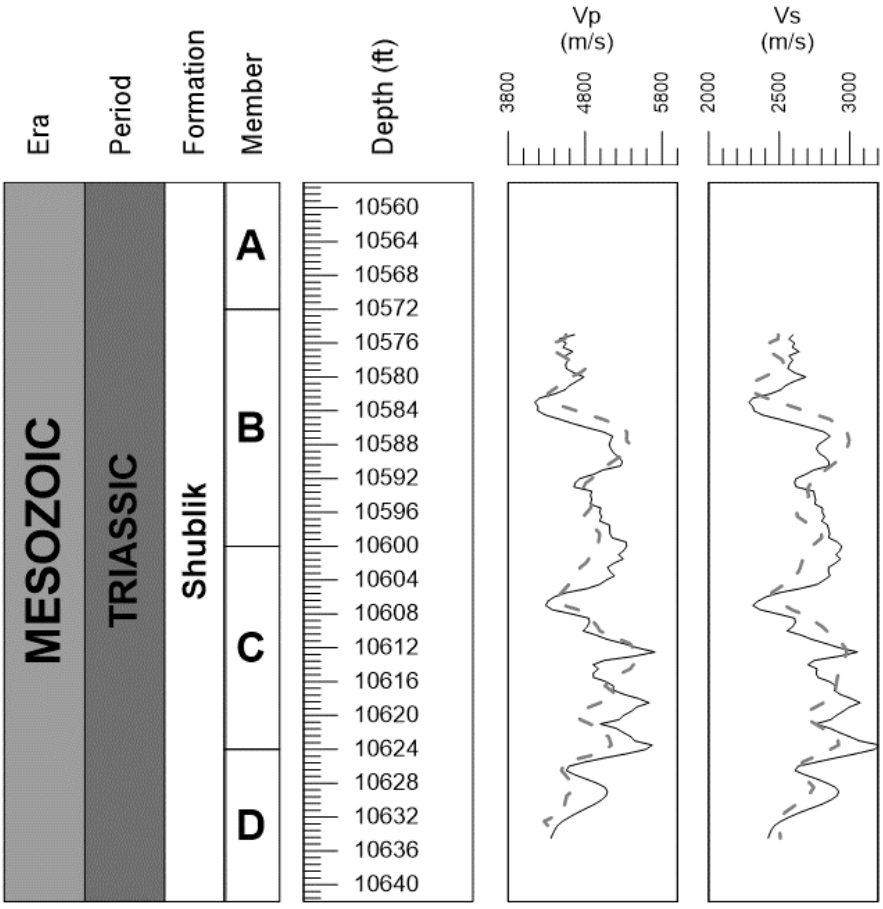

Figure 7. Modeled (solid) versus well log measured (dashed) values for bedding-perpendicular velocities and density in the studied interval.

Mineral	Chemical Composition	Density (kg/m^3)	Bulk Modulus (GPa)	Shear Modulus (GPa)
Quartz	SiO_2	2650	36.6	45
Calcite	$CaCO_3$	2710	76.8	32
Illite	$K_2Al_6Si_6O_{20}(OH)_4$	2750	39.4	11.7
Pyrite	FeS_2	5010	138.9	112.3
Apatite	$Ca_5(PO_4)_3F$	3190	81	44.5

Table 1. Linear optimization system solved in the element to mineral inversion.

References

Alfred, D., and Vernik, L., 2012, A new petrophysical model for organic shales: Presented at the SPWLA 53rd Annual Logging Symposium, Cartagena, Columbia, June 16-20, 15 p.

Avseth, P., Mukerji, T., and Mavko, G., 2005, Quantitative seismic interpretation: Applying rock physics tools to reduce interpretation risk: Cambridge University Press, Cambridge, UK, 408 p.

Broadhead, M. K., Cheshire, S. G., Hayton, S., The effect of TOC on acoustic impedance for Middle Eastern source rock: The Leading Edge, March, p. 258-264.

Claverie, M., Aboel-Abbas, S., Mutiara, C. S., Harfoushian, H., Hansen, S., Leech, R., 2006, Methods for real-time and high-resolution formation evaluation and formation testing of thinly bedded reservoirs in exploration wells: SPE 101126, presented at the SEP Asia Pacific Oil & Gas Conference and Exhibition, Adelaide, Australia, 13 p.

Curtis, M. E., Cardott, B. J., Sondergeld, C. H., and Rai, C. S., 2012, Development of organic porosity in the Woodford Shale with increasing thermal maturity: International Journal of Coal Geology, v. 103. p. 26-31.

Daly, A. R., and Edman, J. D., 1987, Loss or organic carbon from source rocks during thermal maturation: AAPG 91038, presented at the AAPG Annual Convention, Los Angeles, California.

De Caritat, P., Bloch, J., and Hutcheon, I., 1994, LPNORM: A linear programming normative analysis code: Computer & Geosciences, v. 20, no. 3, p. 313-347.

Galdford, J., Quirein, J., Wetacott, D., and Witkoswsky, J., 2013, Quantifying organic porosity from logs: Presented at the SPWLA 54th Annual Logging Symposium, New Orleans, Louisiana, 16 p.

Gassmann, F., 1951. Über die Elastizität poröser Medien. Vier. der Natur. Gesellschaft Zürich, v. 96, p. 1–23.

Hu, R., Vernik, L., Nayvelt, L., and Diceman, A., 2015: Seismic inversion for organic richness and fracture gradient in unconventional reservoirs: Eagle Ford, Texas: The Leading Edge, January, p. 80-84.

Issler, D. R., Hu, K., Bloch, J. D., and Katsube, T. J., 2002, Organic carbon content determined from well logs: Examples from Cretaceous sediments of Western Canada: Geological Survey of Canada Open File 4362, presented at the CSPG 75th Anniversary Convention, Calgary, Canada, 1 p.

Jarvie, Li, C.-X., Duan, Y.-H., and Hu, W.-C., 2015, Electronic structure, elastic anisotropy, thermal conductivity and optical properties of calcium apatite Ca5(PO4)3X (X=F, Cl or Br): Journal of Alloys and Compounds, v. 619, p. 66-77.

Løseth, H., Wensaas, L., Gading, M., Duffaut, K., Springer, M., 2011, Can hydrocarbon source rocks be identified on seismic data?: Geology, v. 39, no. 12, p. 1167-1170.

Loucks, R. G., Reed, R. M., Ruppel, S. C., and Jarvie, D. M., 2009, Morphology, genesis, and distribution of nanometer-scale pores, in siliceous mudstones of the Mississippian Barnett Shale: Journal of Sedimentary Research, v. 79, p. 848-861.

Magoon, L. B., and Bird, K. J., Alaskan North Slope petroleum geochemistry for the Shublik Formation, Kingak Shale, Pebble Shale unit and Torak Formation, in Magoon, L. B., and Claypool, G. E., eds., Alaska North Slope oil/source rock correlation study: Analysis of North Slope Crude: American Association of Petroleum Geologists, Tulsa, Oklahoma, p. 31-48.

Mavko, G., Mukerji, T., and Dvorkin, J., 2010, The rock physics handbook: Tools for seismic analysis of porous media, 2nd Edition: Cambridge University Press, Cambridge, Cambridge, England, 542 p.

Modica, C. J., and Lapierre, S. G., 2012, Estimation of kerogen porosity in source rocks as a function of thermal transformation: Example from the Mowry Shale in the Powder River Basin of Wyoming: AAPG Bulletin, v. 96, no. 1, p. 87-108.

Ogiesoba, O., and Hammes, U., Seismic attribute identification of brittle and TOC-rich zones within the Eagle Ford Shale, Dimmit County, South Texas: Journal of Petroleum Exploration and Production Technology, v. 4, no. 2, p. 133-151.

Okiongbo, K. S., Aplin, A. C., and Larter, S. R., 2005, Changes in type II kerogen density as a function of maturity: evidence from the Kimmeridge Clay Formation: Energy & Fuels, v. 19, p. 2495-2499.

Parrish, J. T., Droser, M. L., and Bottjer, D. J., 2001, A Triassic upwelling zone: The Shublik Formation, Arctic Alaska, USA: Journal of Sedimentary Research, v. 71, no. 2, p. 272-285.

Passey, Q. R., Creaney, S., Kulla, J. B., Moretti, F. J., and Stroud, J. D., 1990, A practical model for organic richness from porosity and resistivity logs: AAPG Bulletin, v. 74, no. 12, p. 1777-1794.

Peters, K. E., Magoon, L. B., Valin, Z. C., and Keller, M. A., 2006, North Slope, Alaska: Source rock distribution, richness, thermal maturity and petroleum charge: AAPG Bulletin, v. 90, no. 2, p. 261-292.

Rowe, H., Hughes, N., and Robinson, K, 2012, The quantification and application of handheld energy-dispersive x-ray fluorescence (ED-XRF) in mudrock chemostratigraphy and geochemistry: Chemical Geology, v. 324-325, p. 122-131.

Schmoker, J. W., 1979, Determination of organic content of Appalachian Devonian shales from formation-density log: AAPG Bulletin, v. 63, no. 9, p. 1504-1537.

Stadnichenko, T., and White, D., 1929, Microthermal studies of some “mother rocks” of petroleum from Alaska: AAPG Bulletin, v. 13, no. 7, p. 823-840.

Steiner, S., Raina, I., Dasgupta, S., Lewis, R., Manson, E. R., Abu-Snaineh, B. A., Alharthi, A., Lis, G. P., and Chertova, A., 2015, Petrophysical challenges in unconventional and tight source rocks, onshore Abu Dhabi: SPE 177614, presented at the Abu Dhabi International Petroleum Exhibition and Conference, Abu Dhabi, United Arab Emirates, 28 p.

Tran, M. T., 1994, Formation evaluation of an unconventional shale reservoir: Application to the North Slope Alaska, MSc thesis, Stanford University, 63 p.

Vernik, L., 1994, Hydrocarbon-generation-induced microcracking of source rocks: Geophysics, v. 59, no. 4, p. 555-563.

Ward, J. A., 2010, Kerogen density in the Marcellus Shale: SPE 131767, presented at the SPE Unconventional Gas Conference, Pittsburgh, Pennsylvania, 4 p.

Whitaker, M. L., Liu, W., Wang, L., and Li, B., 2010, Acoustic velocities and elastic properties of pyrite (FeS2) to 9.6 GPa: Journal of Earth Science, v. 21, no. 5, p. 792-800.

Yurchenko, I., Graham, S. A., Hosford Scheirer, A., and Al Ibrahim, M. A., 2016: Understanding depositional environments of the Shublik Formation of Arctic Alaska using XRF chemostratigraphy: URTeC 2448374, presented at the Unconventional Resources Technology Conference, San Antonio, Texas, p. 1132-1138.

2017 Meeting Poster Abstracts Follow

MULTISCALE CHARACTERIZATION OF PETROLEUM SOURCE ROCKS

Yashar Mehmani[1], Alan K. Burnham[1,*], Michael D. VandenBerg[2], Hamdi Tchelepi[1]
[1]Department of Energy Resources Engineering, Stanford University, Stanford, CA
[2]Utah Geological Survey, Salt Lake City, UT
*aburnham@stanford.edu

Abstract
Simulation of natural petroleum generation and expulsion and in-situ oil shale retorting require characterization of the organic content of the source rock and corresponding values of mechanical properties, thermal conductivity, and permeability as a function of organic content and maturity. We have developed methods using standard optical core photographs (Mehmani et al., 2016a) and near-infrared reflectance core scans (Mehmani et al., 2017). To map the spatial distribution of organic content at the core scale with $O(100\mu m)$ resolution. The latter method is more accurate and generally applicable due to less interference in some formations with high concentrations of dark-colored minerals such as iron-bearing clays and oxides. We apply the method to an immature oil shale core from the Green River Formation, USA, and show its capability in capturing millimeter and meter scale heterogeneity. We demonstrate the fractal-like variability of the organic matter concentration. We demonstrate the implications of this work for mapping spatial distributions of thermo-hydro-mechanical properties of petroleum source rocks at the core scale using thermal conductivity as an example (Mehmani et al., 2016b). Extensions to permeability and elastic modulus would be straightforward given currently established correlations and averaging methods.

Hyperspectral images of several portions of a core from the Mahogany Zone were acquired in collaboration with TerraCore. The images were processed to identify spectral features that (anti-)correlate with organic matter content. Three types of models were subsequently developed: (a) wavelet models based on decomposing the mixture spectrum into a number of power spectra at various scales, (b) broadband models that are based on taking the ratio of two or more reflectance values on the spectrum, (c) an area model that is based on the normalized area of the kerogen absorption band around $\sim$1700nm. All models performed well when tested against measurements. The wavelet models were the most accurate. Models were also tested for samples from Utah versus Colorado, and it was found that only the area model and one of the wavelet models were universally applicable to both locations. The optical method is the least expensive technique in comparison.

Acknowledgments
We acknowledge Total and the Stanford University Petroleum Research Institute for Reservoir Simulation (SUPRI-B) for funding this work. We also thank Specim and TerraCore for the spectral data.

1. Background and motivation

Geologic properties are:

- Strong functions of grade
- Non-linearly dependent
- Micro-structure dependent

Want:

- Thermal conductivity
- Non-linearly dependent
- Micro-structure dependent

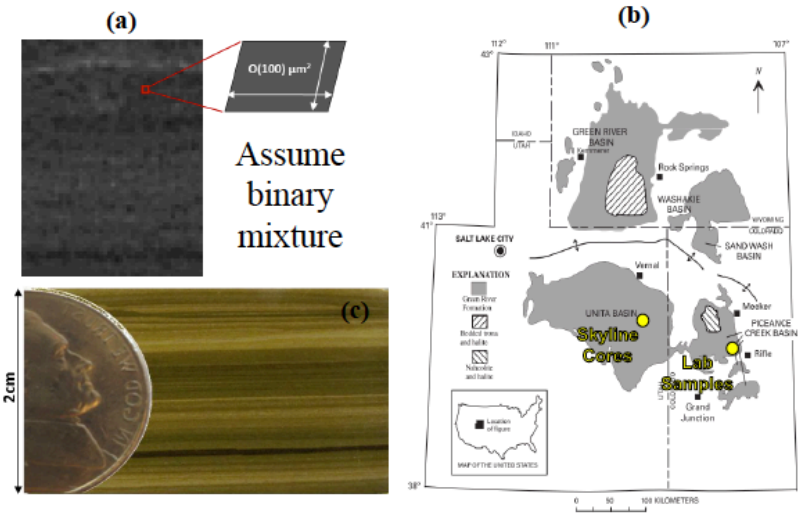

Figure 1: (a) Typical pixel dimensions. (b) Green River Formation sample locations. (c) cm-scale.

2. Heterogeneity on the micron scale

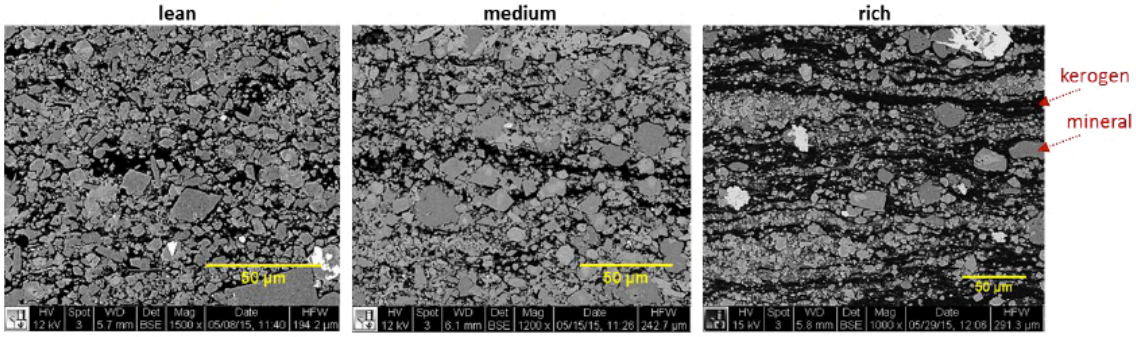

Figure 2: Backscattered scanning electron microscopy images.

3. Heterogeneity on the meter scale

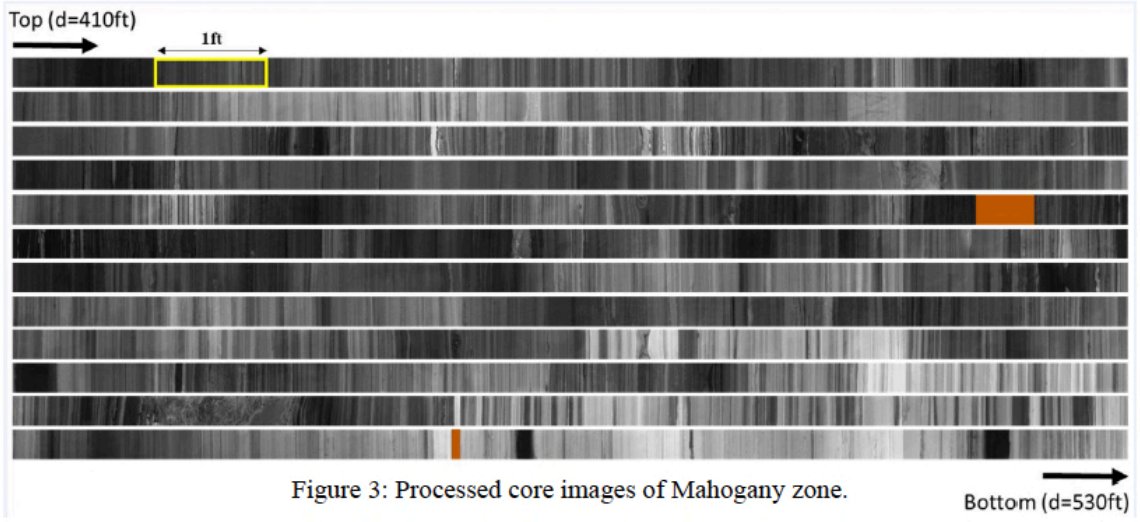

Figure 3: Processed core images of Mahogany zone.

4. Optical method

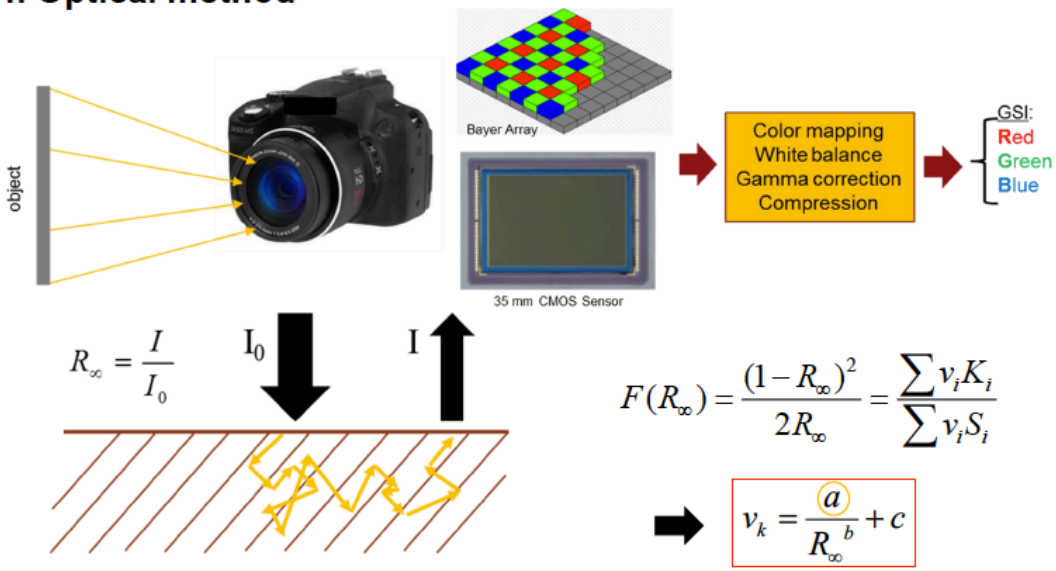

Figure 4: Schematic of the optical method.

5. Near-infrared method

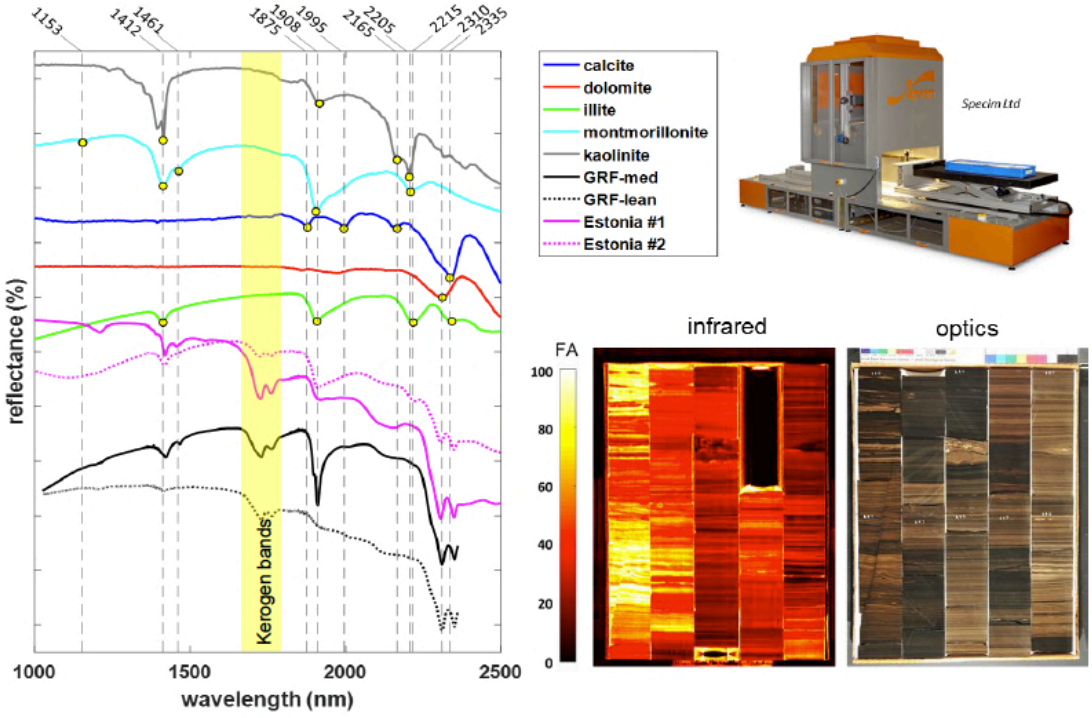

A SIMPLE RELATIVE SORPTIVITY MODEL OF PETROLEUM EXPULSION

Alan K. Burnham
Department of Energy Resources Engineering, Stanford University, Stanford, CA
aburnham@stanford.edu

Abstract
The timing of petroleum expulsion from a source rock is widely accepted to be dominated by the timing of expulsion from kerogen. Expulsion from kerogen is determining by the sorption capacity and relative sorptivity of different chemical types (**Figure 1)**. A two-tank spill model with compositional relative sorptivities is derived and implemented in the kinetic simulator PMod2. Improved compositional models are developed for Green River oil shale and for a generic type II source rock by comparison to a variety of laboratory experiments and geological observations (**Figure 2)**. Combined with estimates of the absorption capacities and relative sorptivities, these models are used to predict the composition of retained and expelled oil as a function of maturity (**Figure 3 and 4**).

Figures

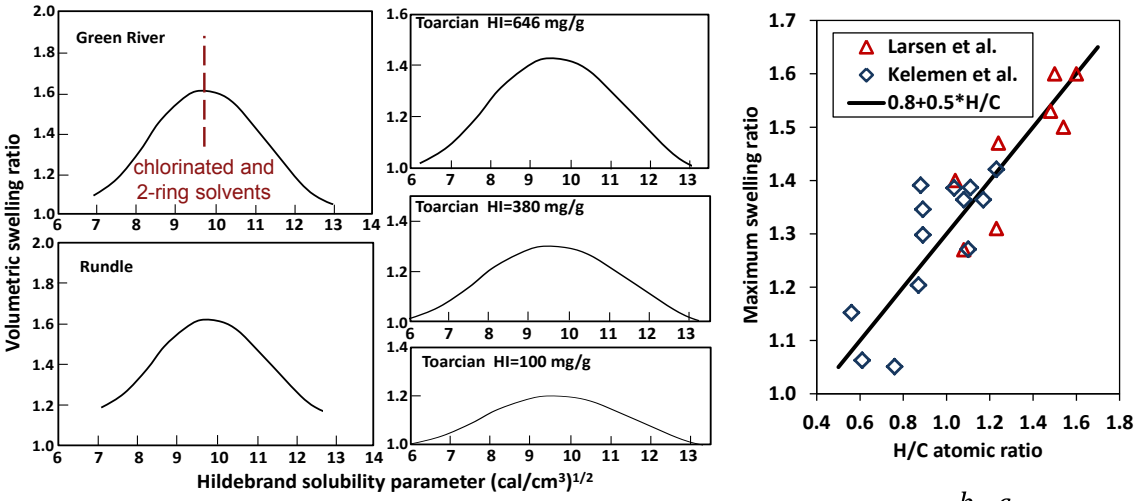

Sorption of liquids and high P limit for gases: $c_{i,ads} = c_{max} \frac{b_i c_i}{\sum_{j=1}^{n} b_j c_j}$

Figure 1. Sorption capacity and selective is well established in the literature.

Rxn	Reactant	Products								
1	KER1	MO3	MO2	MO1	CO2	CH4	COK1	COK2	COK3	
2	KER2	HO3	MO3	COK1	COK2	COK3				
3	KER3	MO3	MO2	MO1	LO1	CHX	CH4	COK1	COK2	COK3
4	HO3	MO3	MO2	MO1	LO1	CHX	CH4	COK1	COK2	COK3
5	MO3	MO1	LO1	LO2	CHX	CH4	COK1	COK2	COK3	
6	MO2	LO1	LO2	CHX	CH4	COK1	COK2	COK3		
7	MO1	LO1	LO2	CHX	CH4	COK1	COK2	COK3		
8	LO1	CHX	CH4	COK1	COK2	COK3				
9	LO2	CH4	COK3				HO3 = nonvolatile polars ≈ DCM-NSOs ≈ asphaltenes			
10	CHX	CH4	COK3				MO3 = volatile polars ≈ nC_5-NSOs ≈ resins			
11	COK1	CH4					MO2 and MO1 = C_{14}-C_{35} aromatics and saturates			
12	COK2	CHX					LO2 and LO1 = C_5-C_{13} aromatics and saturates			
							CHX = C_2-C_4			

Figure 2. Structure of compositional kinetic model having 15 species, 12 reactions, and, depending on kerogen type, 24-36 reaction channels (1-8 per reaction).

Species	Monin et al. (1990)	Behar et al. (2008)	Behar and Jarvie (2013)	Type II model
C_2-C_5	1.96	>1.1	>1.3	2.12
C_6-C_{13}	1.12	>1.1	>1.3	1.36
C_{13+}	0.75	0.80	0.75,0.9	0.79
Aromatics	0.84	0.93	---	0.99
C_6-C_{13}	---	>1.1	---	1.32
C_{14+}	---	0.93	~0.95	0.93
Saturates	1.01	>1.1	---	1.32
C_6-C_{13}	---	>1.1	---	1.41
C_{14+}	---	>1.1	~1.3	1.15
Hydrocarbons	---	≥1.1	>1.3	1.09
Resins	0.68	0.80	0.8	0.81
Asphaltenes	0.68	0.72	0.7	0.71

Figure 3. Maturity at maximum concentrations of various species for a heating rate of 2 °C/h.

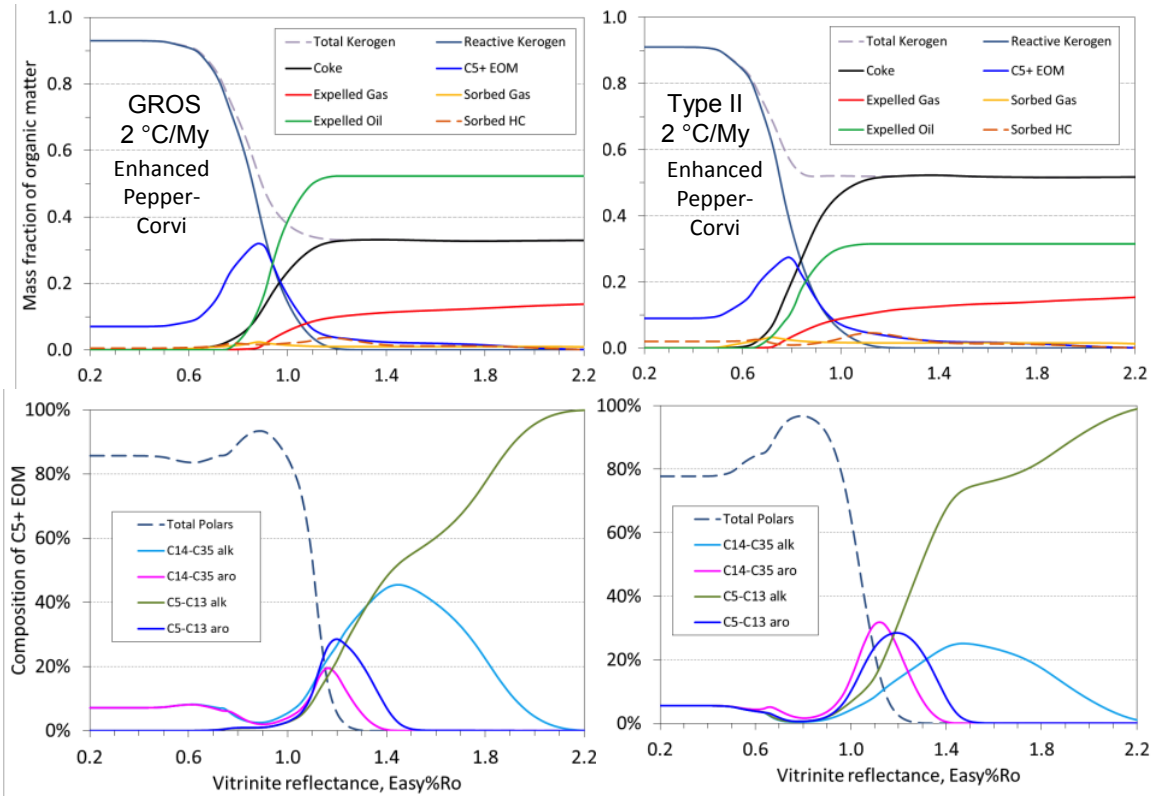

Figure 4. Composition of retained and expelled oil versus maturity at 2 °C/My.

Acknowledgments

This work was supported in part by Total E&P Research and Development, Pau, France.

References

Pepper AS, Corvi PF (1995) Simple kinetic models of petroleum formation. Part III. Modelling an open system. Mar. Petrol. Geol. 12, 417-452.

Burnham AK, Braun RL (2017) Simple relative sorptivity model of petroleum expulsion. Energy Fuels 31, 9308-9318.

CALIBRATION OF AN ADVANCED THREE-PHASE, MULTI-COMPONENT BASIN AND PETROLEUM SYSTEM MODEL FOR THE NORTH SLOPE OF ALASKA

Ken Peters[1,2,*], Oliver Schenk[3], Rolando di Primio[4], Ken Bird[5], Les Magoon[2]
[1]*Schlumberger, Mill Valley, CA*
[2]*Department of Geological Sciences, Stanford University, Stanford, CA*
[3]*Integrated Exploration Systems (IES)-Schlumberger, Aachen 52072, Germany*
[4]*GeoForschungsZentrum Potsdam, Telegrafenberg, 14473 Potsdam, Germany*
[5]*U.S. Geological Survey (emeritus), Menlo Park, CA*
[*]kpeters2@slb.com

The purpose of this study is to evaluate the quality of petroleum phase and fluid property predictions using an advanced basin and petroleum system model for the North Slope of Alaska. The model (832 x 520 km, 1-km grid) includes the coastal plain, Chukchi platform, the foothills of the Brooks Range, and the Beaufort continental shelf. The present-day geometry is based on over 400 wells and extensive seismic data (Figure 1).

Simple black-oil models based on two-component (oil/gas) bulk kinetics, cannot accurately handle the wide range of temperatures, pressures, and component mixture ratios that occur on the North Slope of Alaska. However, three-phase, multi-component models that utilize flash calculations provide useful predictions of petroleum phase and fluid properties, such as API gravity and gas-oil ratio (GOR).

Thermally immature source rock samples from the Shublik Formation, Hue Shale (2), and Kingak Shale were analyzed using the new 'Phase Kinetics' procedure developed and calibrated for PVT-controlled property prediction [1]. Source-rock tracking helped to calibrate the model according to existing mixed accumulations [e.g., 2], thus allowing prediction of the geochemistry of undiscovered accumulations.

The North Slope is characterized by abundant data, which allowed calibration of pressure and temperature. The pressure was calibrated in two steps: one related to rock compressibility, the other to permeability (overpressure calibration). Pressure data for calibration, mainly from drill stem and repeat formation tests, was quality controlled by removing data where measured pore pressures were lower than hydrostatic or higher than lithostatic pressure.

Heat flow was calibrated against vitrinite reflectance and later cross-checked with Horner-corrected bottom-hole temperatures. The vitrinite data required special screening, e.g., to remove reverse depth trends resulting from recycled vitrinite. Calibration focused on the Brookian rather than the deeper Ellesmerian sequence where anomalous vitrinite measurements occur. Due to the size of the model, a filtered subset or reflectance data with a 2-km grid was used for calibration based on 105 selected wells.

Calibrated heat flow maps that were assigned to the model are consistent with published measurements and conclusions [3], e.g., shallow and deep basement correspond to high and low heat flow, respectively, probably due to convective movement of groundwater where heat was transported from the foothills in the south to the coastal plain in the north.

The results indicate that most of the wells in the study area show good calibration against vitrinite reflectance. The assigned heat flow maps, sediment-water interface temperatures, and paleo-water depths are also consistent with regional geology and recent concepts of the thermal regime on the North Slope.

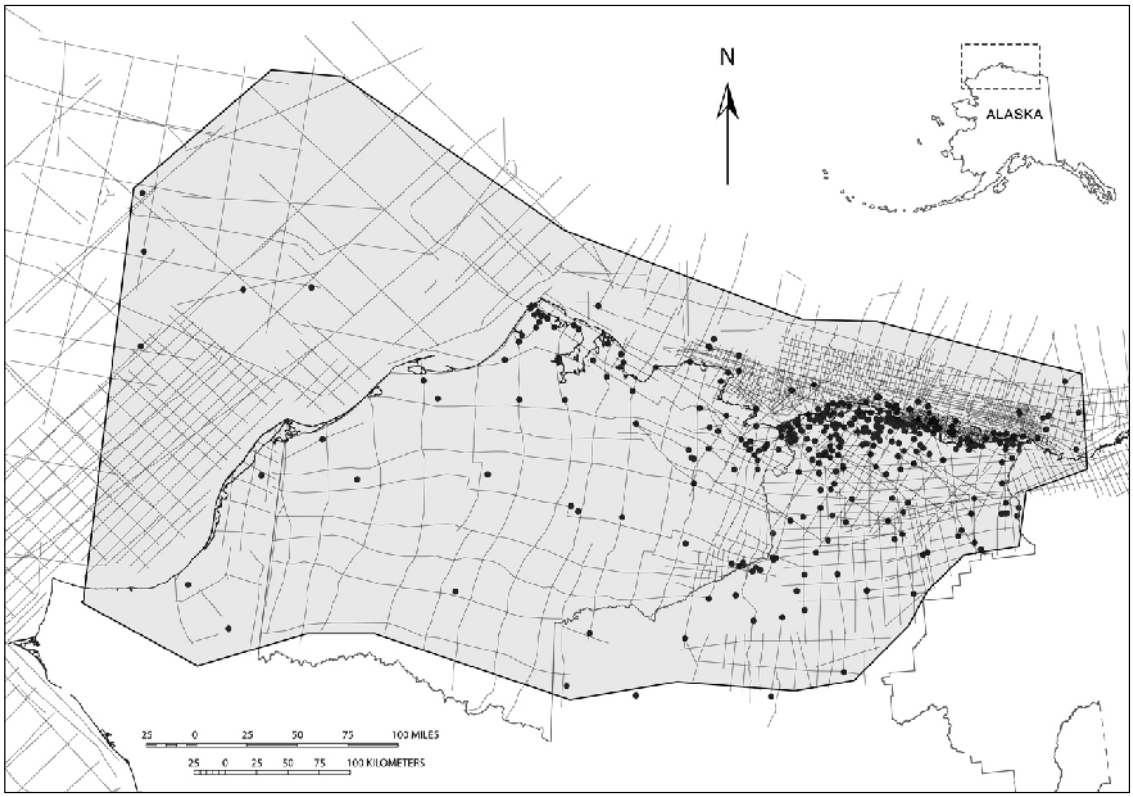

Figure 1. Map of the North Slope of Alaska shows the outline of the model polygon (gray shading). Seismic lines and well locations were used to create structure and isopach maps.

References

[1] di Primio, R., Horsfield, B. (2006) Amer. Assoc. Petrol. Geol. Bull 90, 1031-1058.
[2] Peters, K.E., Ramos, L.S., Zumberge, J.S., Valin, Z.C., Bird, K.J. (2008) Org. Geochem. 39, 623-645.
[3] Deming, D., Sass, J.H., Lachenbruch, A.H., de Rito, R.F., 1992, Amer. Assoc. Petrol. Geol. Bull. 104, 528-542.

IMPROVED OIL-OIL CORRELATION VIA CHEMOMETRICS: EXAMPLE FROM THE ONSHORE AND OFFSHORE SANTA MARIA BASIN, CALIFORNIA

K.E. Peters[1,2], P.G. Lillis[3], T.D. Lorenson[4], and J.E. Zumberge[5]
[1]Schlumberger, Mill Valley, CA kpeters2@slb.com
[2]Department of Geological Sciences, Stanford University, Stanford, CA
[3]U.S. Geological Survey, Denver, CO
[4]U.S. Geological Survey, Santa Cruz, CA
[5]GeoMark Research LLC, Houston, TX
[*]kpeters2@slb.com

Abstract
The purpose of this work is to analyze 48 crude oil samples from the onshore and offshore Santa Maria basins to identify genetic affinities and establish petroleum systems. A key goal is to resolve the controversy as to whether certain geochemical variations (e.g., sulfur content, biomarker and isotope ratios) among the samples result from organofacies variations within the source rock or other factors. Source-related biomarker and stable carbon isotope ratios for each oil sample were assessed to assure that they were unaffected by secondary processes, such as heavy biodegradation or thermal maturation, and were compiled as a training set. The training set allowed creation of a chemometric decision tree (e.g., Peters et al., 2007) that classifies newly collected samples of crude oil or source-rock extracts. Six genetic oil families identified by the chemometrics show map distributions that reflect organofacies variations within the Miocene Monterey Formation source rock (**Figure 1**). Three onshore families originated from two pods of thermally mature source rock. The offshore oil samples consist of one family from the Point Pedernales field and two families from the Point Sal and San Miguel prospects.

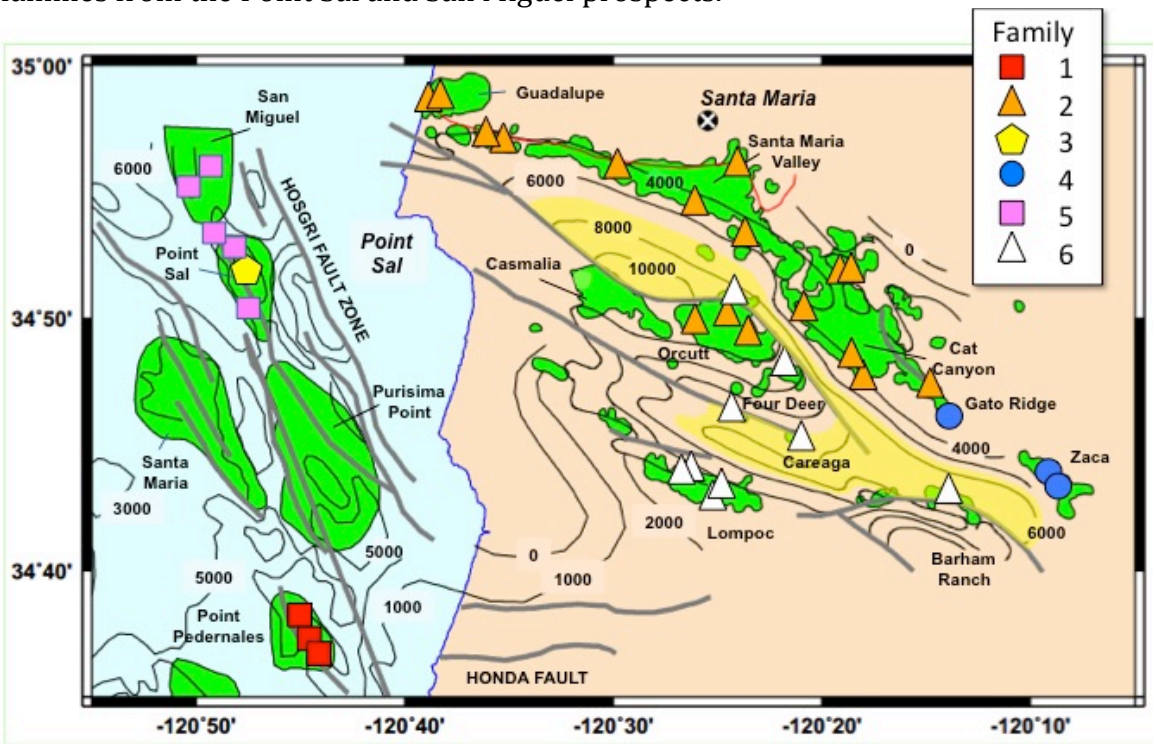

Figure 1. Locations of six oil families in the Onshore and Offshore Santa Maria basins generated from organofacies of the Miocene Monterey Formation based on chemometric analysis of 21 source-related biomarker and carbon isotope ratios for 48 crude oil samples (**Figure 2**). Depth contours (ft) are from Isaacs (1992); yellow overlay highlights deep Monterey source rock (>7,000 ft or 2,134 m depth).

Introduction

Geochemical oil-oil and oil-source rock correlations are required to establish petroleum systems. However, many published correlations rely solely on bivariate or ternary plots of source-related geochemical data. These limited data may be insufficient to reliably infer genetic affinities. This paper shows the value of chemometrics (multivariate statistics) to define oil families and infer source rock organofacies for 48 high-sulfur crude oil samples from the Santa Maria basins (**Figure 1**). Stratigraphic data (Sweetkind et al., 2010) support two converging synclines in the onshore basin where Miocene Monterey Formation source rock reaches the oil window at ~9,000 ft (2,743 m) depth (Tennyson and Isaacs, 2001). However, no publications describe genetic differences for oils from these synclines. Offshore production is expected to differ from the onshore oil because the fields and prospects occur west of the Hosgri fault, although the extent of right-lateral displacement along the fault remains speculative.

Samples and Methods

Analyses were conducted at GeoMark Research LLC. Stable carbon isotope ratios of saturates and aromatics were analyzed using a Finnigan Delta E mass spectrometer (MS). Saturates were analyzed by split injection on a Hewlett-Packard 5890 gas chromatograph (GC) interfaced to a Hewlett-Packard 5971 MS. The GC oven and HP-5 column (50 m, 0.2 mm I.D., 0.11-mm film thickness) were programmed from 150 to 325°C at 2°C/min. The MS operated in selected ion mode, monitoring ion mass-to-charge ratios (m/z) of 177, 191, 205, 217, 218, 221, 231, and 259. Response factors were based on m/z 221 response for a deuterated d4-C_{29} 20R sterane (Chiron Laboratories, Norway) compared with sterane (m/z 217) and terpane (m/z 191) standards. Hierarchical cluster analysis (Pirouette®, Infometrix Inc., Bothell WA, USA; autoscale preprocessing, Euclidean distance, incremental linkage) used 21 source-related biomarker and isotope ratios (Peters et al., 2005, 2007) to identify genetic families among the 48 oil samples (**Figure 2**): C_{19}/C_{23}, C_{22}/C_{21}, C_{24}/C_{23}, C_{26}/C_{25}, Tet/C_{23}, C_{28}/H, C_{29}/H, C_{30}X/H, Ol/H, C_{31}R/H, Ga/H, C_{35}S/C_{34}S, and C_{26}/Ts terpanes, steranes/terpanes, %C_{27}, %C_{28}, %C_{29} steranes, $\delta^{13}C_{saturates}$, $\delta^{13}C_{aromatics}$, $\delta^{13}C_{whole\ oil}$, and the canonical variable (CV).

Results

Twenty-one source-related biomarker and carbon isotope ratios for non- or mildly biodegraded oil samples from the Santa Maria area differentiate six genetic families generated from ^{13}C-rich organofacies of the Miocene Monterey Formation (**Figure 2**). This training set was used to create a chemometric decision tree (e.g., Peters et al., 2007) that classifies new samples of crude oil or source rock extracts and assigns a level of certainty for each correlation.

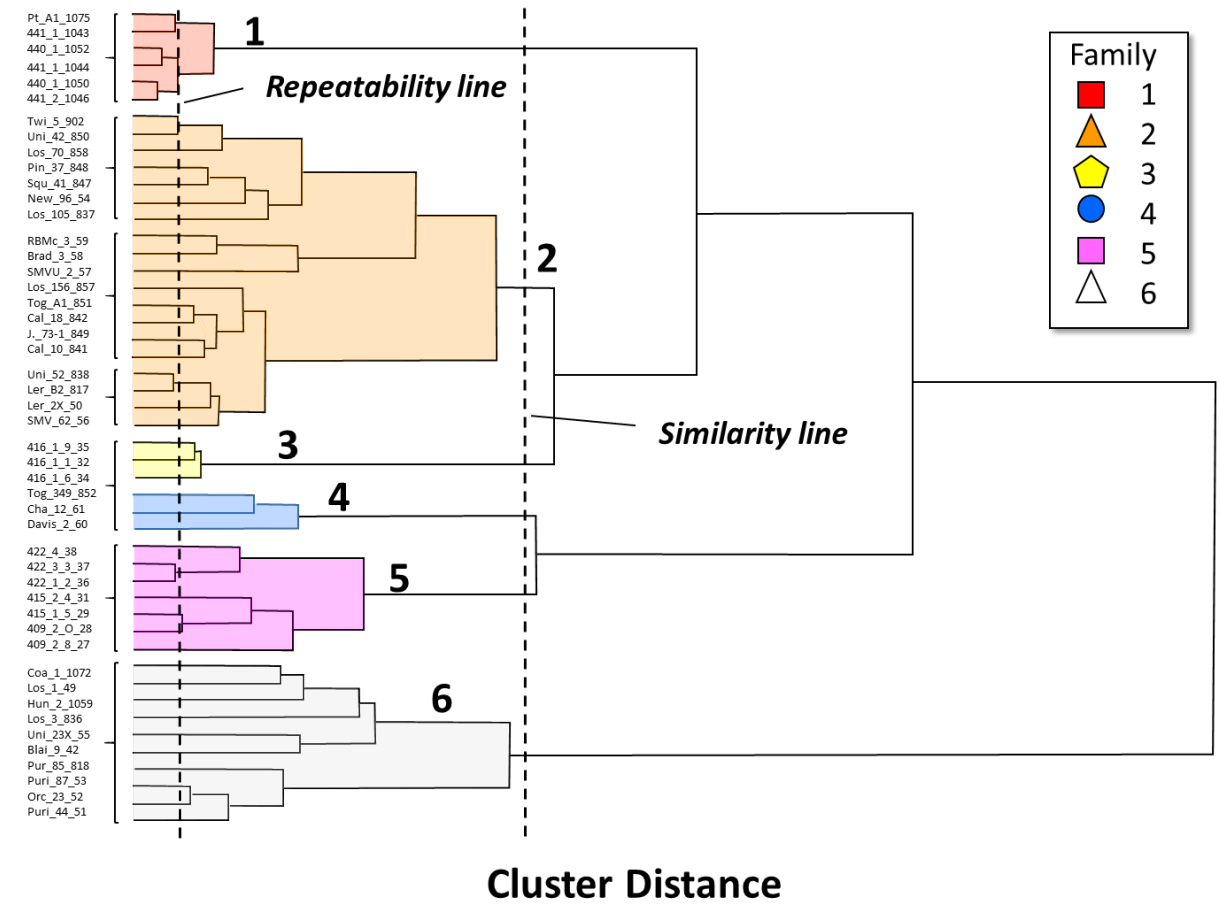

Figure 2. Hierarchical cluster analysis of 21 biomarker and isotope ratios for 48 samples identifies six Santa Maria oil families (similarity line). Repeatability is based on four oil samples (422_1_2_36 and 422_3_3_37 in the same well at similar depths; 409_2_O_28 and 415_1_5_29, nearby wells at overlapping depths).

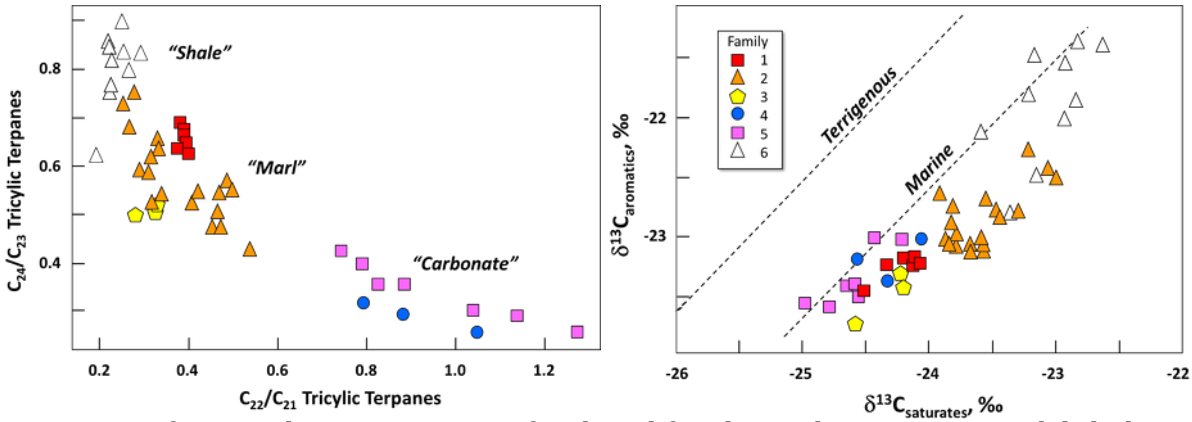

Figure 3. Left: Tricyclic terpane ratios for the oil families indicate source rock lithology ranging from carbonate to marl to shale. Assigned lithology is based on >500 global oil samples (Figure 13.76 in Peters et al., 2005). Right: Carbon isotope ratios of saturates and aromatics show that marine organic matter dominated the source rock for all six oil families. Dashed lines are best fits of data for 339 global oil samples from Sofer (1984). The

^{13}C-rich compositions of all samples are consistent with an origin from the Monterey Formation.

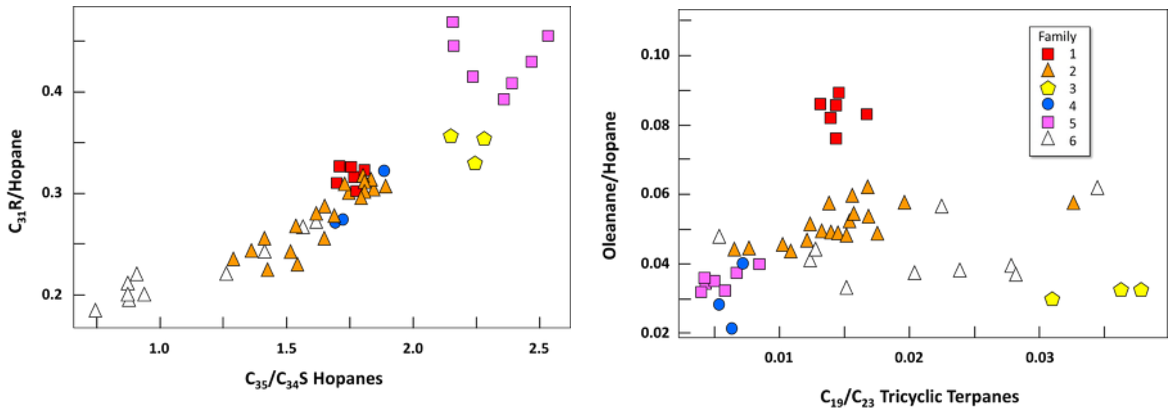

Figure 4. Left: Higher C_{35}/C_{34} hopane and $C_{31}R$/hopane indicate more reducing conditions and more carbonate during source rock deposition, respectively. Right: Higher C_{19}/C_{23} tricyclic terpanes suggest greater higher-plant input, while higher oleanane/hopane is specific for angiosperm (flowering plant) input (Peters et al., 2005).

Locations of onshore oil families 2, 4, and 6 conform to the subsurface distribution of thermally mature Monterey Formation in two synclines (**Figure 1**). Families 2 and 6 dominate the onshore area. Family 2 includes 19 samples from the Guadalupe, Santa Maria Valley, Cat Canyon, and Orcutt fields, which mostly lie on a NW-SE trend updip and NE of the northern syncline. Family 6 includes 10 samples from the Barham Ranch, Four Deer, Lompoc, Orcutt, and Careaga Canyon fields near the southern syncline. The Monterey source in the northern syncline was more carbonate-rich with more marine-influenced organic matter (**Figure 3**) deposited under more reducing conditions with higher-plant input that differed from the more proximal clastic-rich Monterey source in the southern syncline (**Figure 4**). This is consistent with the occurrence of Monterey organofacies for Families 2 and 6 in different NW-trending fault-bounded crustal slivers that formed during Neogene clockwise tectonic rotation of the western Transverse Ranges and N-S extension with little or no rotation within the Onshore Santa Maria basin (Hornafius, 1985). Paleobathymetry likely controlled the distribution of organofacies prior to formation of the synclines. Family 4 is like Family 5 and consists of three samples from the Zaca and Gato Ridge fields in the eastern map area.

The three remaining oil families occur offshore to the west of the Hosgri fault. Family 1 includes six samples from the Point Pedernales field that show weak affinity to Families 2 and 3. Family 3 consists of three samples from the Point Sal prospect. Family 5 consists of seven samples from wells in the San Miguel and Point Sal prospects.

Conclusions

Chemometric analysis of 21 source-related biomarker and stable carbon isotope ratios for 48 oil samples from the Onshore and Offshore Santa Maria basins identifies six genetic oil families. The detail achieved by this multivariate approach is far greater than that allowed by conventional oil-oil correlations based on bivariate or ternary diagrams of source-

related data. The six families show systematic map distributions that reflect organofacies variations within the Miocene Monterey Formation source rock. Three onshore oil families originated from one pod of thermally mature source rock at depths >9,000 ft (2,743 m). The offshore oil families are distinct and consist of one family from Point Pedernales field and two families from the Point Sal and San Miguel prospects. A chemometric decision tree based on the 48-sample training set allows classification of newly collected oil and source rock extracts.

Acknowledgments

We thank John Curtis and Alex Zumberge (GeoMark Research) for data and technical assistance and Scott Ramos and Brian Rohrback (InfoMetrix, Inc.) for helpful discussions. Allegra Hosford Scheirer and Les Magoon (Stanford Basin and Petroleum System Modeling Industrial Affiliates Program; http://bpsm.stanford.edu) and Rick Stanley (USGS) helped with map preparation and useful review comments.

References

Hornafius J.S., 1985. Neogene tectonic rotation of the Santa Ynez Range, Western Transverse Ranges, California, suggested by paleomagnetic investigation of the Monterey Formation: J. Geophysical Research 90, 12503-12522.

Isaacs C.M., 1992. Preliminary petroleum geology background and well data for oil samples in the cooperative Monterey organic geochemistry study, Santa Maria and Santa Barbara-Ventura basins, California: USGS Open-File Report 92-539-F.

Peters K.E., J.M. Moldowan, 1993. The Biomarker Guide. Prentice-Hall, Englewood Cliffs, NJ, 363 p.

Peters K.E., C.C. Walters, J.M. Moldowan, 2005. The Biomarker Guide. Cambridge U. Press, U.K., 1155 p.

Peters K.E. et al., 2007. Circum-Arctic petroleum systems identified using decision-tree chemometrics: AAPG Bulletin 91, 877–913.

Radke M., D. Welte, 1983. The methylphenanthrene index (MPI): A maturity parameter based on aromatic hydrocarbons. *In* M. Bjorøy et al., eds., Adv. in Org. Geochem. 1981, J. Wiley & Sons, 504-512.

Sofer Z., 1984. Stable carbon isotope compositions of crude oils: Application to source depositional environments and petroleum alteration: AAPG Bulletin 68, 31-49.

Sweetkind D.S. et al., 2010. Digital tabulation of stratigraphic data from oil and gas wells in the Santa Maria basin and surrounding areas, Central California Coast: USGS Open-File Report 2010-1129.

Tennyson M., C. Isaacs, 2001. Geologic setting and petroleum geology of Santa Maria and Santa Barbara basins, coastal California. *In* C.M. Isaacs, J. Rullkötter, eds., The Monterey Formation: From Rocks to Molecules. Columbia U. Press, 206–229.

COMPARISON OF KINETIC MODELS FOR VITRINITE MATURATION

Oliver Schenk[1,*], Alan Burnham[2], Ken Bird[3], and Ken Peters[4,5]
[1]*Schlumberger, Aachen, Germany*
[2]*Department of Energy Resources Engineering, Stanford University, Stanford, CA*
[3]*U.S. Geological Survey (emeritus), Menlo Park, CA*
[4]*Department of Geological Sciences, Stanford University, Stanford, CA*
[5]*Schlumberger, Mill Valley, CA, USA*
[*]oschenk@slb.com

Abstract
A modified Easy%R_o is proposed to address concerns about the sharp bend (dogleg) in plots of vitrinite reflectance versus depth commonly observed at depths corresponding to ~0.7 to 1.0% R_o. Characterization of this dogleg is complicated by issues related to identification of true vitrinite, maceral interactions during diagenesis, and reflectance suppression. Comparison to laboratory experiments is complicated by consideration of lithostatic pressure (Burnham, 2017).

Easy%R_oDL (Schenk et al., 2017) modifies Easy%R_o (Sweeney and Burnham, 1990) by increasing the frequency factor (A) to a more typical value of 2×10^{14} s^{-1} and adjusting the activation energies (E_a) to produce a smaller rate of increase with thermal exposure during diagenesis and a faster rate of increase during metagenesis and catagenesis.

We tested and calibrated the different vitrinite reflectance models to assess the impact on timing of maturity and hydrocarbon generation. This poster compares Easy%R_o, its update Easy%R_oDL, and Basin%R_o (Nielsen et al., 2015) using 1D basin and petroleum system modelling for several wells from the Alaska North Slope.

Introduction
Thermal maturation of organic matter mainly depends on temperature and time. This relationship and vitrinite optical properties have been used to formulate kinetic models for the thermal maturation of vitrinite to reconstruct thermal history (e.g., Easy%R_o: Sweeney and Burnham, 1990; Basin%R_o: Nielsen et al., 2015) and to calibrate basin and petroleum system models. First-order Arrhenius-type kinetic models with a distribution of activation energies and a single frequency factor can be used to extrapolate from laboratory to geological conditions. Easy%R_o may be less accurate than Basin%R_o for calibration of basin and petroleum system models as it overestimates maturity in the range of the oil window (Suggate, 1998; Nielsen et al., 2015). Basin%R_o more accurately replicates the dogleg in vitrinite reflectance versus depth that is commonly observed at depths corresponding to ~0.7 to 1.0% R_o, where the hydrogen index decreases due to kerogen transformation after being approximately uniform at lower maturity (Suggate, 1998). However, Basin%R_o does not predict reflectance as well as Easy%R_o for laboratory heating experiments (Nielsen et al., 2015).

Adjusting the frequency factor (A) and activation energy (E_a) distribution

The frequency factor is not well constrained from either laboratory experiments or geologic data. Kerogen transformation ratio (TR) and R_o likely have a similar relationship at both time scales (**Figure 1**).

Easy%R_oDL (Schenk et al., 2017) modifies Easy%R_o by increasing the frequency factor (A) to a more typical value of that of kerogen conversion ($A = 2 \times 10^{14}$ s^{-1}) and adjusting the activation energies (E_a) (**Figure 2**) to produce a lower rate of increase with thermal exposure during diagenesis and a faster rate during metagenesis and catagenesis. It is similar to Basin%R_o at geologic heating rates, but agrees better with R_o from lab experiments.

Figure 3 shows the temperature/vitrinite reflectance relationship of the individual vitrinite reflectance models. The significantly different end value of maturity is not important because it is reached at temperatures above 300° C. More important is the interval between 100 and 200° C with modeled maturities of 0.5 to 1.7% R_o (early oil to wet gas window). Here, Basin%R_o and the updated Easy%R_oDL show lower maturities compared to Easy%R_o but a sharp increase at 150 and 170° C, respectively.

Study area

The geologically complex Northern Alaska petroleum province evolved through the tectonic stages of passive margin, rift, foreland basin, and foreland fold-and-thrust belt. Petroleum was generated from several source rock units, and many reservoirs show evidence of mixing of hydrocarbon source types. Rift-related structures and a regional break-up unconformity are critical trapping and migration components of the largest oil and gas accumulations. In addition, stratigraphic traps that developed during extensional and compressional tectonic regimes show significant resource potential in Jurassic through Cenozoic shelf and turbidite sequences. Thermal maturation is mainly controlled by the Brookian Sequence deposited during Late Cretaceous to Cenozoic time in a prograding foreland basin predominantly from WSW to ENE (Bird, 2001) (**Figure 4**).

Comparison of Vitrinite Reflectance Models for Alaska North Slope Wells

To compare Easy%R_o, Basin%R_o and Easy%R_oDL, we selected several wells from the Alaska North Slope with significant differences in the timing and amount of Brookian burial and erosion. They all show the characteristic dogleg of vitrinite reflectance versus depth (**Figures 5 and 6**). For the Inigok-1 and Bush Federal-1 wells we extracted model input from the regional 3D basin and petroleum system model (Schenk et al., 2012) including, e.g., litho- and organofacies, paleo-basin geometry, and the amount and timing of Tertiary erosion. Only the basal heat flow was adjusted to match the respective vitrinite reflectance models. The Aurora-1 well is located outside the 3D BPSM polygon and we, therefore, constructed the 1D model based on well information from Banet (1993).

Thermal calibration with the individual vitrinite reflectance models required geologically reasonable variations of the basal heat flow starting from the late post-rift phase (**Figures 5 and 6**). Scenarios calibrated with Basin%R_o and Easy%R_oDL show a very close match with the dogleg and temperature. This was not possible with Easy%R_o, which

overestimates vitrinite reflectance in the oil window. For the comparison, we created an Easy%R_o scenario that matches only the shallow steeper R_o segment, which required basal heat flow significantly lower than the Basin%R_o and Easy%R_oDL scenarios.

To evaluate the impact of the calibrated scenarios on the timing of maturity and potential hydrocarbon generation, we focused on penetrated source rock units (Kingak-K1 unit and Shublik Formation). The results show a short period of hydrocarbon generation for the Basin%R_o and Easy%R_oDL scenarios that is mainly controlled by the sudden deep burial by Brookian sediments. Easy%R_o scenarios that match calibration data only in the steep shallow segment predict a slower and later increase of transformation ratio and do not match the observed high thermal maturity of the pre-Brookian sediments.

Conclusions

We tested different vitrinite reflectance models to assess the impact on timing of maturity and hydrocarbon generation. We compared Easy%R_o (Sweeney and Burnham, 1990), its update Easy%R_oDL (Schenk et al., 2017), and Basin%R_o (Nielsen et al., 2015) using 1D basin and petroleum system models of several wells from the Alaska North Slope. In the North Slope study area, Easy%R_o overestimated vitrinite reflectance in the oil window, but Basin%R_o and Easy%R_oDL show significantly improved calibrations against vitrinite reflectance profiles that include the characteristic dogleg structure versus depth.

The individual calibrated models show only slight differences in the timing of petroleum generation because the main control is rapid burial by Brookian sediments. However, variations in the compositions of generated components are likely due to the different boundary conditions needed to calibrate the R_o data for each vitrinite reflectance model.

References

Banet, A.C. [1993] A geochemical profile and burial history of Aurora 890 #1 OCS Y-0943 well offshore of the ANWR 1002 Area, Northeast Alaska. BLM-Alaska Technical Report 16, 56 p.

Behar, F., Vandenbroucke, M., Tang, Y., Marquis, F. and Espitalie, J. [1997] Thermal cracking of kerogen in open and closed systems: determination of kinetic parameters and stoichiometric coefficients for oil and gas generation. Organic Geochemistry 26(5/6) 321-339.

Bird, K. J. [2001] Alaska: A 21st century petroleum province. In: Downey, M.W., Threet, J.C. and Morgan, W.A. (Eds.) Petroleum provinces of the twenty-first century, AAPG Memoir 74, 137-165.

Burnham, A. K. [2017] Global chemical kinetics of fossil fuels – how to model maturation and pyrolysis. Springer, 315 p.

Nielsen, S.B., Clausen, O.R. and McGregor, E. [2015] Basin%Ro: A vitrinite reflectance model derived from basin and laboratory data. Basin Research. doi:10.1111/bre.12160

Schenk, O., Bird, K.J., Magoon, L.B. and Peters, K.E. [2012] Petroleum system modeling of Northern Alaska. In: Peters, K.E., Curry, D. and Kacewicz, M. (Eds.) Basin Modeling: New Horizons in Research and Applications. AAPG Hedberg Series 4, 317-338.

Schenk, O., Peters, K.E. and Burnham, A.K. [2017] Evaluation of alternatives to Easy%Ro for calibration of basin and petroleum system models. Extended abstract, EAGE, Paris, France.

Suggate, R.P. [1998] Relations between depth of burial, vitrinite reflectance and geothermal gradient. Journal of Petroleum Geology 21(1), 5-32.

Sweeney, J.J. and Burnham, A.K. [1990] Evaluation of a simple model of vitrinite reflectance based on chemical kinetics. AAPG Bulletin 74, 1559-1570.

Figures

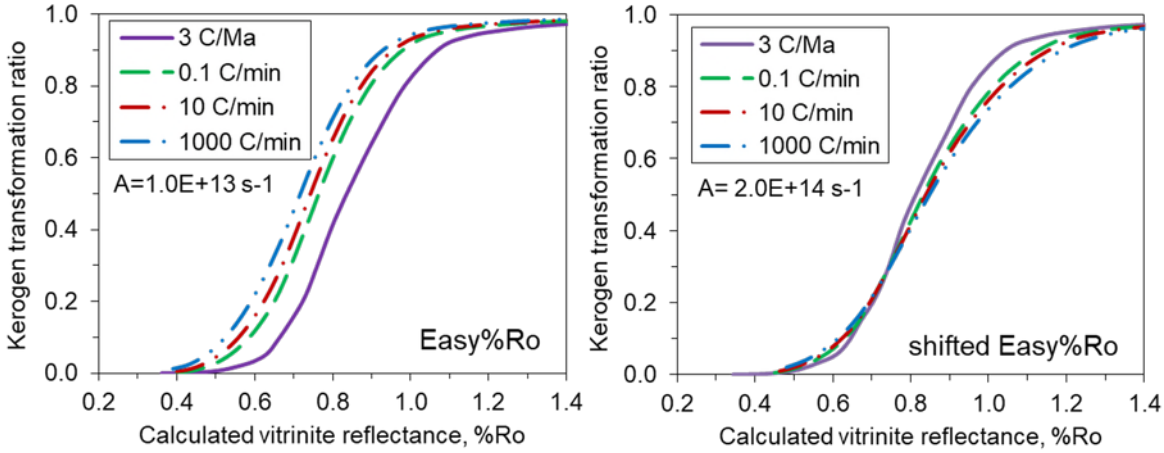

Figure 1. Calculated vitrinite reflectance vs kerogen TR for different heating rates using A from Easy%R_o (left) and a modified Easy%R_o (right) using 2×10^{14} s^{-1} (more typical of kerogen decomposition) and shifting the E_a distribution by 2.7 kcal/mol to match %R_o at 3 °C/Ma. Kerogen-to-oil TR was calculated from Behar et al. (1997) type-II kerogen in which A = 1.6×10^{14} s^{-1}.

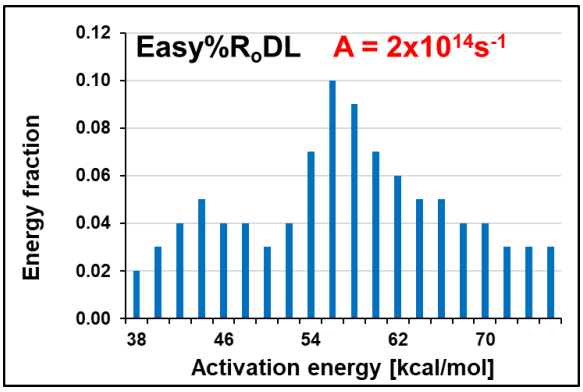

Figure 2. Activation energy distribution used in Easy%R_oDL. The sum of the energy fractions is 0.95, and the conversion to reflectance is given by $\%R_o = \exp(-1.5+3.7F)$, where F is the fraction reacted.

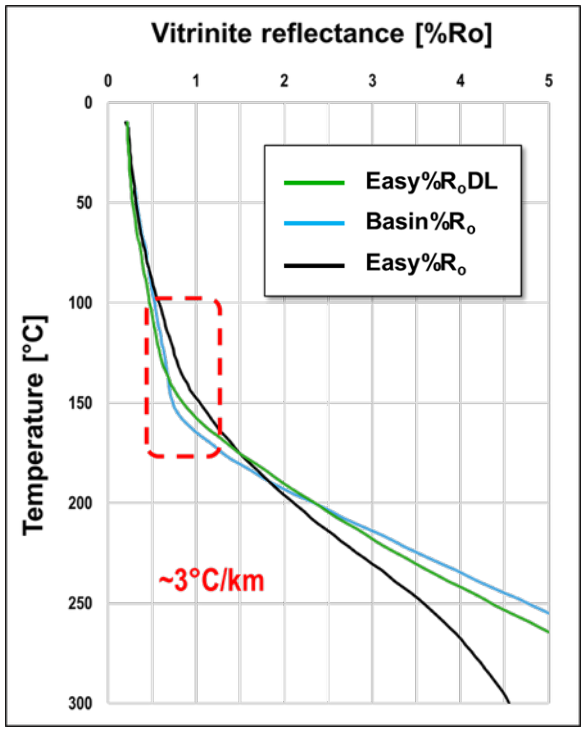

Figure 3. Temperature/vitrinite reflectance relationship of the three analyzed vitrinite reflectance models (Easy%R_o, Basin%R_o and Easy%R_oDL). Dashed red box highlights maturity range that is overestimated by Easy%R_o).

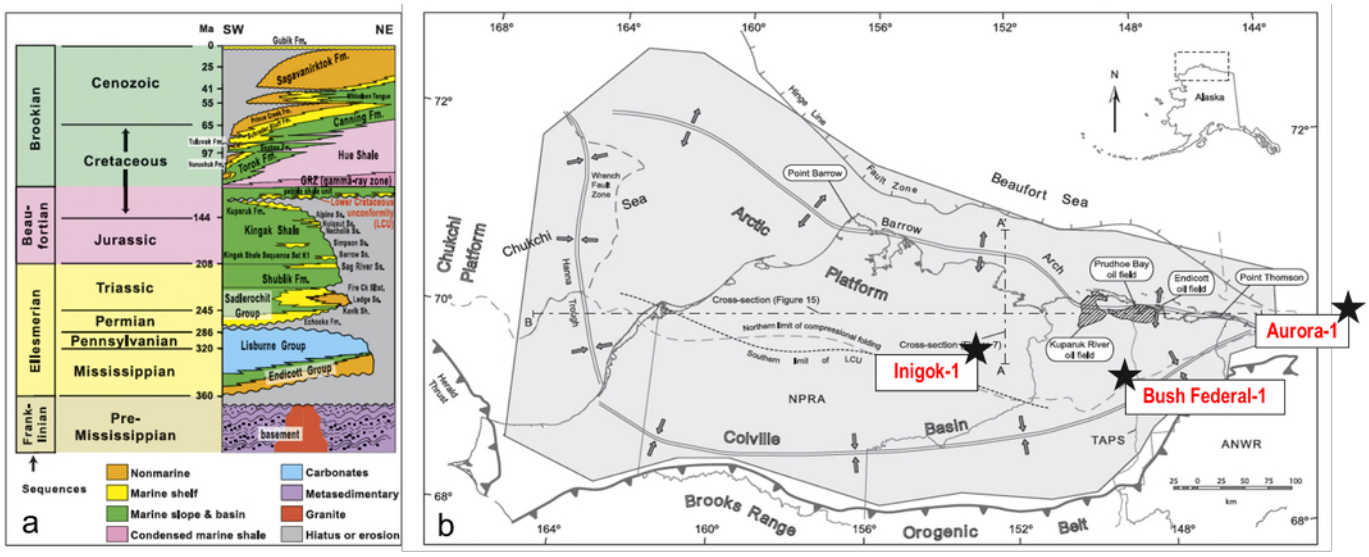

Figure 4. Alaska North Slope stratigraphy (a; after Bird, 2001) and location of wells for selected 1D models (b).

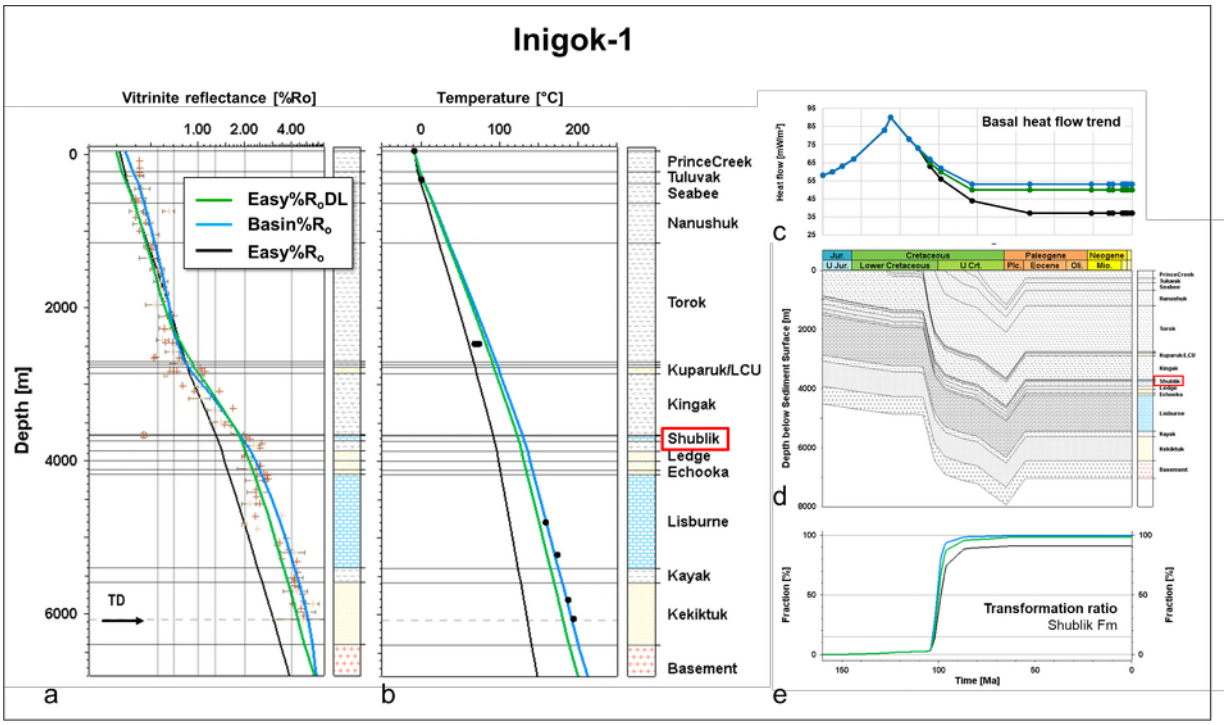

Figure 5. Well plots for Inigok-1 well showing predicted and measured R_o vs depth (a), predicted and measured temperature (b), the required basal heat flow for thermal calibration (c), burial history (d), and TR vs time for Shublik Fm (e).

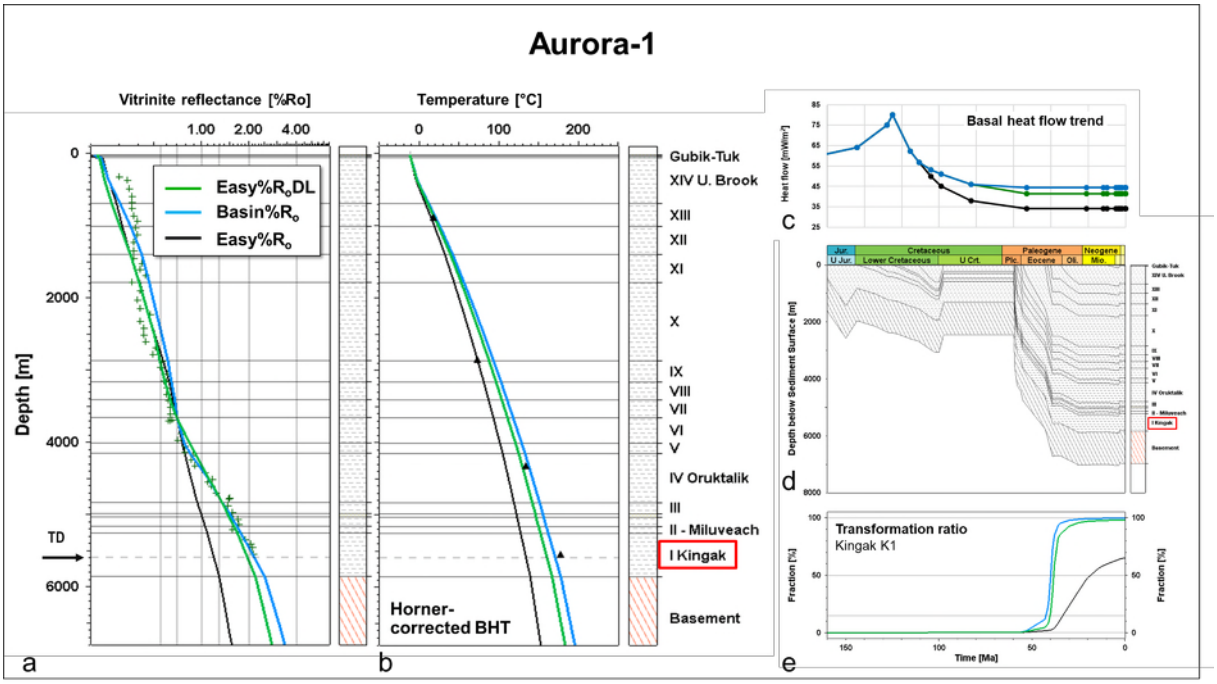

Figure 6. Well plots for Aurora-1 well showing predicted and measured R_o vs depth (a), predicted and measured temperature (b), the required basal heat flow for thermal calibration (c), burial history (d), and TR vs time for Kingak K1-unit (e). Note the later time of peak burial compared to Inigok-1 (**Figure 5**) as result of the E-NE prograding depocenter of the Brookian sequence that mainly controls hydrocarbon generation.